Title
Dissipative Materials Enabled Subwavelength Nanophotonics

Author
Deng, Yang

Publication Date
2019

Peer reviewed|Thesis/dissertation

Dissipative Materials Enabled Subwavelength Nanophotonics

By

Yang Deng

A dissertation submitted in partial satisfaction of the
requirements for the degree of
Doctor of Philosophy
in
Engineering – Materials Science and Engineering
in the
Graduate Division
of the
University of California, Berkeley

Committer in charge:

Professor Jie Yao, Chair
Professor Junqiao Wu
Professor Ming C. Wu

Fall 2019

Dissipative Materials Enabled Subwavelength Nanophotonics

Abstract

Dissipative Materials Enabled Subwavelength Nanophotonics
by

Yang Deng

Doctor of Philosophy in Engineering – Materials Science and Engineering

University of California, Berkeley

Professor Jie Yao, Chair

Properly structuring materials at subwavelength scale allows for strong light-matter interaction, thereby enhancing near-field effects and engineering far-field scattering through intermodal interference. A majority of such effects are associated with plasmonics where electromagnetic waves created in the vicinity of metallic nanostructures is able to give rise to a variety of novel phenomena and fascinating applications. In the recent years, dielectric nanoparticles with high refractive index based on optically induced electric and magnetic Mie resonances attract a plethora of attention. In this rapidly developing field, dissipative loss in optical materials is considered one of the major challenges. Here, in this dissertation, we show that, counter-intuitively, it contributes positively to sub-wavelength scale light enhancement and confinement, and also improves scattering efficiency in the far field.

In the first part of this dissertation, near field enhancement in dissipative dielectric antennas is demonstrated to be orders of magnitude higher than their lossless dielectric counterparts, which is particularly favorable in deep UV applications where metals are plasmonically inactive and transparent dielectrics always have low index. The loss facilitated field enhancement is the result of large material permittivity contrast and electric field discontinuity. These dissipative dielectric nanostructures can be easily achieved with a great variety of dielectrics at their Lorentz oscillation frequencies, thus having the potential to build a completely new material platform boosting light-matter interaction over broader frequency ranges, with advantages such as bio-compatibility, CMOS compatibility and harsh environment endurance.

Additionally, manipulation of ultra-violet light through metasurface in the far field utilizing the silicon loss is then presented. We experimentally demonstrate Si metasurfaces working effectively over a broad band down to 290nm, with efficiencies comparable to plasmonic metasurface performance in the infrared regime. And for the first time, we show photolithography enabled by metasurface-generated ultraviolet

holograms. We attribute such performance enhancement to the large scattering cross-sections of Si antennas in the ultraviolet range, which is adequately modeled via a circuit model. Our new platform will deepen our understanding of the role of material dissipation and introduce even more material options to broadband metaphotonic applications, including those in integrated photonics and holographic lithography technologies.

Dynamically tunable far field with subwavlength nanostructures is always desired for practical applications. In the last section of this dissertation, we introduce a lithography free and field-programmable photonic metacanvas. Previous attempts of realizing such idea used micro-mechanical metamaterials or amorphous-crystalline phase transition materials, which are limited in terms of the functionalities, efficiency, cost, and high working temperature (> 600^{o}C). It is much desired to reconfigure photonic devices in a fast, large-scale, cost-effective, reliable, and free-style way at or near room temperature. Here, we present a completely rewritable meta-canvas on which arbitrary photonic devices can be rapidly written, erased and rewritten. The writing is with a low-power (1 mW) continuous laser and the entire process stays below ~ 90^{o}C. Using these devices we demonstrate dynamical manipulation of optical waves for light propagation, reconstruction and polarization. Such meta-canvas supports physical (re)compilation of photonic operators akin to that of FPGA, opening up possibilities where a single photonic element can be field-programmed to deliver complex, system-level functionalities.

Contents

LIST OF FIGURES

LIST OF TABLES

ACKNOWLEDGEMENTS

First and foremost, I owe a lot of debt of gratitude to my advisor, Prof. Jie Yao. I am sincerely grateful for the support and guidance he granted me to explore new research ideas. I am also glad to have had the opportunity to serve as a graduate student instructor in MSE 123, and I am very grateful to Jie for the breadth of this teaching experience.

I would like to also express my sincere gratitude to all the members of my dissertation committee, Professors Jie Yao, Ming-Chiang Wu and Junqiao Wu for their time and thoughtful advices. Thanks are also given to Professors Liwei Lin and Joel Ager IIII for serving on my qualifying exam committee.

The works presented in this dissertation have been accompanied by plenty of supports from all the people in the Yao lab. Particularly, I am specifically grateful to Dr. Xi Wang. Xi was a great research mentor during my PhD study, who has a comprehensive knowledge of optical/photonic simulations, nano-fabrication, and optical measurements. None of the works in this dissertation would have been possible without him. Kaichen Dong, Zilun Gong, Shuai Lou have both been instrumental in helping me to solve the issues in my device simulations, fabrication and testing. The fruitful discussions we had in our group always gave me new insights in understanding the deep physics and developing new ideas.

I also would like to thank other group members in the Yao lab, Kyle B Tom, Yin Liu, Fuyi Yang, Shuren Lin, Rui Chen, Qingjun Wang and Jinhua Cao. Their research progress always made me inspired and encouraged me to explore further in my research.

Thank you to the staff of the Marvell Nanolab and BNC and your dedication to running such professional academic facilities. The collaboration with Prof. Laura Waller and Nicolas Pégard is very fruitful. Especially, I am grateful to Nicolas Pégard for his very collaborative and motivated attitude, which enabled our collaborative work on the ultraviolet metasurfaces.

I'd like to thank my parents and family in China. Their unquestioning and generous supports have been crucial to the completion of this dissertation. Last but not least, I would like to thank my wife, Shiqian Shao, and my family for their love and encouragement.

Chapter 1

Introduction

1.1 Subwavelength confinement and localization

In nineteenth century, British physicist Lord Rayleigh investigated the predominantly elastic scattering of light by subwavelength particles to explain why the sky is blue. Since then, the nanoparticle-induced scattering has been of importance for optical scientists. Later, German physicist Gustav Mie explained a dependence of colors of gold colloids upon their size distribution, hence opening up the possibility of utilizing resonant nano-scatterers to control an optical response.

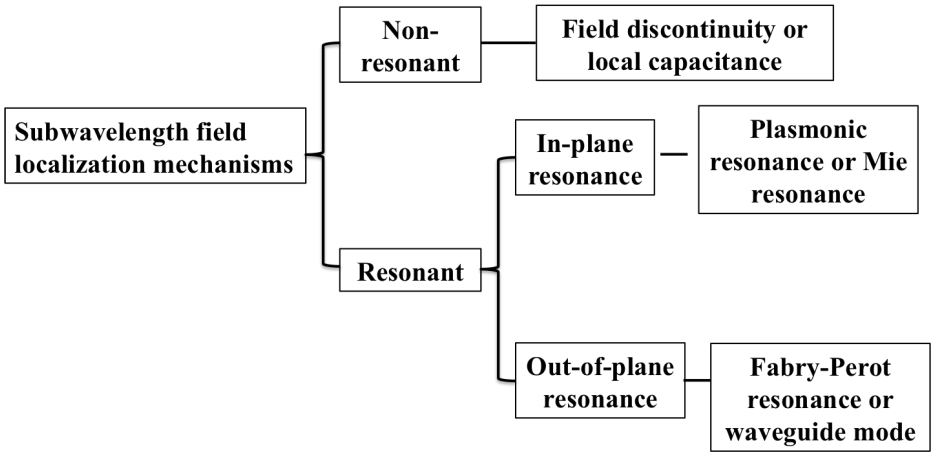

Figure 1. 1 Diagram of categories of subwavelength field localization mechanisms for both metals and dielectrics [1].

Recent decades have witnessed a rapid progress in nanophotonics, especially the study of plasmonic nanoparticles, such as gold (Au), or silver (Ag), in which the electromagnetic surface waves couple to collective plasmons [2]. Proper design of the nanostructures allows resonant optical modes, enabling manipulation of the light effectively at the nanoscale. This notion opens up a broad range of new opportunities in sciences and technologies, including optical data storage [3], bio sensing [4], lithography [5], imaging [6], etc.

The physical origins of light enhancement at nanoscale can be categorized into non-resonant and resonant phenomena, as shown in Figure 1.1 [1]. The mechanism of non-

resonant light confinement originates from the field discontinuity or local capacitance effect at the interface of two media, such as metal-dielectric and dielectric-dielectric interfaces (shown in Figure 1.2) [7-12]. When a light impinges onto or reflected from a metal-dielectric interface, the accumulated charge near the sharp edges of the metal creates surface currents, which is the so-called edge effect [13]. If two subwavelength metallic sharp pieces point to each other, forming a metallic slit (a nano-gap), the oscillation of the incident electric field near the slit induces the co-directional surface current density at a specific time (Figure 1.2(b)) [8, 13]. Thereby, the charges accumulated at opposite edges of the slit have opposite signs, generating electric dipoles to enhance the electric field in the nano-gap.

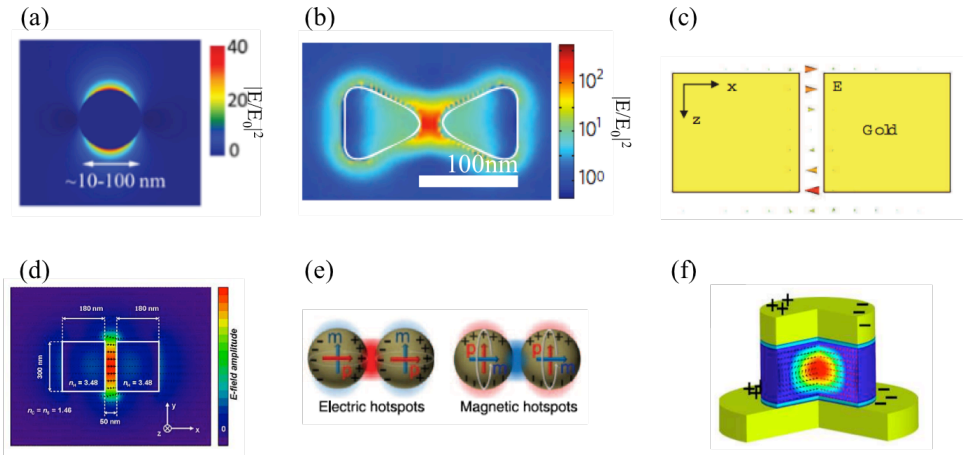

Figure 1. 2 Light localization and confinement in metallic, dielectric and hybrid nanostructures. (a) The near field distribution of electric field around a metallic nanoparticle [7]. (b) A gold bowtie structure with resonant electric field distribution [8]. (c) Electric maximum peak field distribution of FP resonance in a gold nanostructure [9]. The size and the direction of the arrows indicate the strength and direction of the electric field respectively. (d) Cross-section profile of the electric field in a dielectric waveguide [10]. (e) Magnetic and electric enhancement in the nanogap between two silicon nano-cylinders [11]. p and m denote electric and magnetic dipole moments, respectively . Arrows indicate polarization direction for electric (E) and magnetic (H) fields. Color varies from minimal (blue) to maximal (red) values. (f) Simulated electric mode profile for the fundamental mode (TM_{111}) in a hybrid structure (gold-semiconductor nanopatch). The surface color at the cross-section represents the electrical energy density [12]. Arrows indicate the direction of the electric (red) and magnetic (black) field.

When the geometrical size is properly designed and is close to the wavelength of the incident light, the phase of the incident field is not spatially uniform anymore, leading to the retardation effect [14]. In this retardation effect regime, the mechanism based on resonance can be further utilized to enhance the field confinement. The resonances mentioned here can be classified into two types: in-plane resonance (Figure 1.2(b)) and the vertical resonance (Figure 1.2(c)). The in-plane or out-of-plane resonances are dependent upon the size and permittivity in the corresponding plane or direction of the metallic particle and the ambient medium [9]. In another word, the in-plane resonance involves the perimeter of the metallic particle while the out-of-plane is pertinent to its thickness.

Take an example of a single metallic nanosphere, shown in Figure 1.2(a). When the perimeter of the nanosphere approaches the wavelength in vacuum, the phase of the excited surface currents along the nanosphere is no longer in phase and instead the retarded phase distribution exists, leading to a certain type of resonance condition, such

as dipoles, quadrupole and other high-order modes [7]. Other more complicated designs involves different resonances were discussed and reported systematically [7, 15]. The out-of-plane resonance is associated with Fabry-Pérot (FP) cavity resonance of the metal particle [9]. The FP resonance is hampered as well when the thickness is large enough to exceed the propagation loss. Therefore a thin metal sheet with optimal design is required to readily observe the FP resonance [1].

In addition to noble metals, in the past decades, dielectrics, especially the ones with high refractive index, has also been widely known to be able to manipulate light to be below the free-space diffraction limit [11, 16]. These high-index dielectrics combined with properly designed nanostructures offer negligible optical losses, have the similar mechanisms as metals: non-resonant and resonant behaviors. However the detailed physics behind is different because of the lack of free electrons in dielectrics. Figure 1.2(d) shows a slot waveguide made of dielectrics, in which the light is confined inside the middle layer with low index dielectric material [10]. When the two waveguides with high index are placed closed enough such that the gap size is less than the decay length of the evanescent field outside waveguide, the field in the gap will be enhanced due to the discontinuity of electric field polarized perpendicular to the interface. In this nanostructure, no resonance is required to confine the electromagnetic field and the confined field in the nanogap can propagate along the slot waveguide.

Introduction of resonances in dielectric nanoantennas brings up their extreme ability to concentrate electromagnetic field in the nanoscale as well. These resonances can be analyzed well with Mie scattering theory [17], which works for both metal and dielectrics but they there are some differences in terms of physics behind due to their opposite sign of dielectric permittivity, which is negative for metals and positive for dielectrics. For a metallic nanoparticle with a fixed size parameter, surface plasmon resonances of an electric type (such as dipole, quadruple, etc) are produced while there is almost negligible magnetic response because of very little evanescent field inside the metallic particle (the magnetic response can actually be generated in metallic structures but some specific designs are required, such as split-ring resonators [18]). For dielectric nanoparticle, both electric and magnetic resonances with the similar strength can be observed, as shown in Figure 1.2(e) [11]. Thanks to the negligible material loss, the field can be confined inside the dielectric particle and thereby such enhanced field combined with phase retardation effect enables the resonant magnetic dipole when incident light couples with the circular displacement currents of the electric field.

1.2 Optical Metasurfaces

Near field engineering with nanoparticles also affects the scattering property of light in the far field. Advanced control of light propagation in the far field is crucial for numerous modern technologies, such as high-capacity communications [19], optical sensing [20], and high-resolution imaging applications [21]. However, conventional optical elements are bulky and do not meet the fast-growing requirements of integration in compact systems [22]. Optical metasurfaces consisting of nano-scatterers aforementioned are able to modify the light properties while maintaining substantial

miniaturization of photonic devices [23, 24]. They are composed of an artificial nanostructured planar interface that has subwavelength thickness and that controls light properties by spatially arranged meta-atoms (or so-called optical antennas). Those meta-atoms (plasmonic or dielectric scatterers), interact with the incident EM fields resonantly or non-resonantly, resulting in engineering different characteristics of the scattered light from the incidence such as its amplitude, wavefront, polarization, or spectrum [25-30].

The first optical metasurface was demonstrated utilizing V-shape antennas in the Mid-infrared (Mid-IR) (show in Figure 1.3(a)) and then confirmed in near-infrared (near-IR) spectral regimes respectively [31, 32]. There are two plasmonic eigenmodes existing in such optically anisotropic antennas. With properly designed geometry and orientation of the antennas, the phase of y-axis polarized light in the scattered field has an incremental change of $\pi/4$ between two neighboring V-shape antennas when incidence is x-axis polarized [31]. The thickness of the antenna is only around one tenth of the wavelength in vacuum but the spatially varying phase profile allows for anomalous refraction, orbital angular momentum generation, etc [25-30].

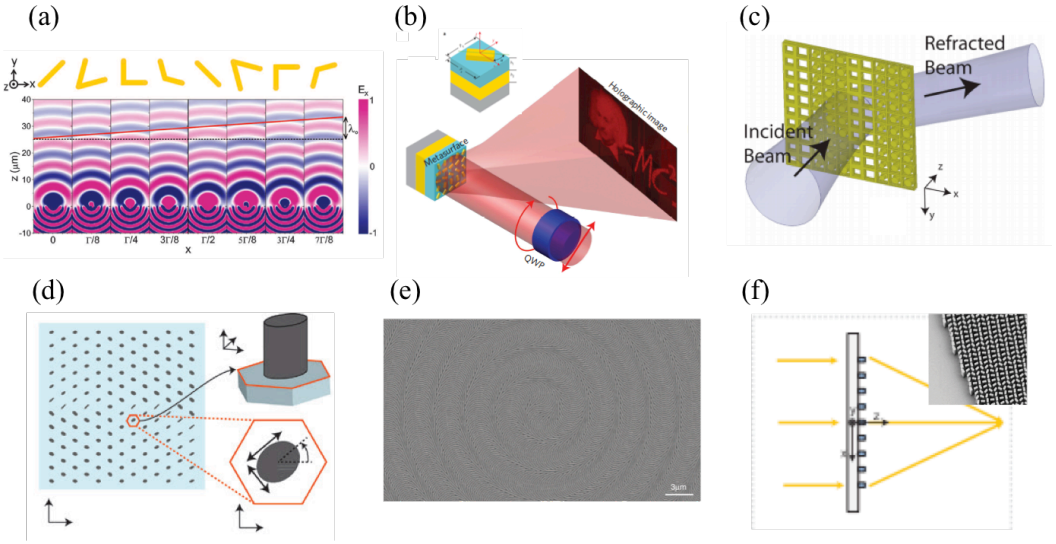

Figure 1. 3 Metallic (a-c) and dielectric (d-f) metasurfaces. (a) Plasmonic V-shape antenna enabled metasuface to bend beam in the mid-IR regime [31]. (b) Reflective metasurfaces for hologram generation in the near-IR and visible range [33]. (c) Schematic of an optically thin, isotropic Huygens' metasurface that efficiently refracts a normally incident beam at telecommunication wavelengths [34]. (d) A spatially varying waveplate with the ability to convert horizontally and vertically polarized input light to radially and azimuthally polarized output light in the telecommunications band [35]. (e) SEM image of the fabricated dielectric metasurface axicon consisting of silicon (Si) nanobeams at near-IR wavelengths [36]. (f) Schematic configuration of a dielectric metalens at visible wavelengths. Inset: SEM picture of the dielectric metalens [37].

The mechanism based on V-shape antenna has to involve two antenna resonances to introduce the phase or amplitude tunability. A completely different approach to bring out phase jump is to utilize so-called Pancharatnam-Berry phase (geometric phase) [38, 39]. An example is shown in Figure 1.3 (b) [33]. The subwavelength scaterers (nanorod) with same geometric size but spatially varying orientation angle allow for different phase delay. With a transparent spacer layer and reflective mirror underneath, the efficiency for hologram demonstration in reflection was reported up to 80% in the near-IR region (shown in Figure 1.3(b)) [33]. The metasurfaces based on geometrical phase

is associated with polarization change as well. In another word, it works for circularly polarized incident light and manipulate the circularly polarized transmission with the opposite handness. The mathematical derivation based on Jones matrix makes it easy to reveal the relation between polarization and phase delay. More details will be discussed in Chapter 5. The recent investigation on geometric phase has been following the early works by Hasman and co-workers [40, 41].

To improve the efficiency of the metasurface in transmission, one has to completely eliminate reflection and avoid any absorption inside the material. The impedance match by controlling the surface electric and magnetic polarizabilities is able to minimize the reflected power and boost the efficiency. This type of metasurface is called Huygens' metasurface [42-48]. This concept was first demonstrated in microwave regime [48], and then one example in the optical range is shown in Figure 1.3(c) [34] . Engineering the effective surface impedance of the metasurface via changing the filling ratios, high transmission efficiency can be achieved [34]. Additionally, subwavelength size particles supporting Fano resonance (interference of a broad electrical dipole and high-order modes) is able to induce asymmetry in the light scattering and thereby enhancing the forward scattering efficiency [49].

Due to high losses of metals at visible frequencies and their incompatibility with complementary metal oxide semiconductor (CMOS) fabrication processes, dielectric metasurfaces stands out in terms of efficiency due to their capability of engineering resonant electric and magnetic optical response combined with negligible losses. The initial idea of utilizing dielectric structures to engineer the far field distribution was studied two decades ago based on blazed gratings [41, 50]. Some other similar ideas based on nano-posts have been reported recently as well to achieve the 2π phase delay [35, 42, 47, 51]. A complete control of phase and polarization in the near-IR range was demonstrated by using amorphous silicon (Si), as shown in Figure 1.3(d) [35]. This approach is not directly based on the resonances of single element and requires relatively tall nanoparticles (close to vacuum wavelength) to achieve multiple resonances such that 2π phase delay is achievable while maintaining high transmission for all of the post sizes. The geometric phase approach aforementioned for plasmonic metasurfaces works for dielectric ones as well. A recent work based on geometric phase principle demonstrated flat Si lenses and axicons at near-IR wavelength range (shown in Figure 1.3(e)) [36] . This approach was further extended to highly efficient operation at visible frequency regime by employing transparent titanium dioxide (TiO_2) nanofin structures [37]. To achieve high efficiency, high aspect ratio (reaching 10:1) is required even if the high index material, Si or TiO_2, is used. Meanwhile the highest efficiencies to date for operation in the transmission mode have been reported, are in the range of 80 to 90%. Low index material, silicon nitride (Si_3N_4) was also demonstrated to have the same efficiency but the height of nanopillar needs to be scaled up proportionally to compensate the index decrease [52]. This is also so called "waveguide mode" or Fabry-Pérot mode.

1.3 Motivation

In the photonic systems for subwavelength light confinement and enhancement and optical metasurfaces, noble metals (Au, Ag, etc.) based on plasmonic effect was used first from the Terahertz to near-IR. However, because of intrinsic Ohmic losses of metals at visible wavelengths and their incompatibility with complementary metal oxide semiconductor (CMOS) fabrication processes, only very few plasmonics applications have been realized in practice [11]. Aluminum (Al) has a potentially better response at shorter wavelengths, but it suffers from oxidation induced performance degradation and fabrication challenges when scaled down [53, 54]. Although there are new materials with improved plasmonic properties being proposed [55], they have limited efficiencies in the ultraviolet (UV) regions, where a variety of ubiquitous applications are of interest (e. g. high-resolution photolithography, imaging and chemical/biological sensing applications) [56]. In all of these materials, dissipative material loss, represented by the imaginary part of permittivity (ε_i), exists ubiquitously and has been widely believed to be detrimental for many applications. Research efforts so far have been focused on minimizing the material loss [57]. For example, lossless dielectric structures have also been utilized to compress light into subwavelength structures aforementioned [10, 16]. However, they are unable to show comparable light enhancement capabilities as plasmonic structures [10, 16].

Regarding the metasurface applications, dielectric materials, including Si, titanium dioxide (TiO_2), Gallium Nitride (GaN) and silicon nitride (Si_3N_4), recently have been employed to manipulate light efficiently based on Mie resonances or so-called waveguide modes at near-IR and visible frequencies [35-37, 51, 52]. Nevertheless, the reported thicknesses of dielectric metasurfaces were close to or even larger than their operation wavelengths, leading to high aspect ratios of 10 ~ 15 [35-37, 51, 52]. Moreover, most UV transparent dielectrics have low refractive indices (e.g., MgF_2, CaF_2, and SiO_2), posing more severe challenges to the metasurface design and fabrication for the UV range. In addition, very low index contrast compared to the substrates also compromises the performance.

In this dissertation, we show that, counter-intuitively, large material permittivity in dielectric nanophotonic structures may contribute to both near-field enhancement and far field manipulation effectively. The small light enhancement factor in existing dielectric systems can be greatly improved with the introduction of large material permittivity, represented by the imaginary part of the permittivity. Furthermore, in the metasurface system, the scattering capability can be augmented as well because of the larger permittivity.

1.4 Thesis plan and overview

The main goal of this dissertation is to demonstrate the potential of large permittivity of materials in the realization of efficient meta-photonic platform for some unique applications and new device concepts. The remainder of the dissertation describes our works utilizing the material large permittivity and tunable metaplatforms. In Chapter 2,

we show subwavelength field enhancement in the dissipative dielectric nano-antennas. In Chapter 3, we show a non-resonant dielectric nanogap structure to achieve field confinement enabled by the large permittivity of materials. In Chapter 4, we propose a circuit model for dissipative dielectric antennas to demonstrate the ability of high scattering efficiency in the far field. In Chapter 5, the design of all Si UV metasurfaces based on the large permittivity of Si is discussed. In Chapter 6, fabrication and characterization of the all Si ultraviolet metasurfaces are discussed in details. We experimentally demonstrated the metasurface for beam steering and UV hologram enabled high-resolution lithography. In Chapter 7, we show a rewritable photonic metacanvas platform based on the phase transition of vanadium dioxide (VO_2).

Chapter 2

Field confinement and fluorescence enhancement enabled by dispersive antennas

2.1 Review of Drude - Lorentz dispersion model

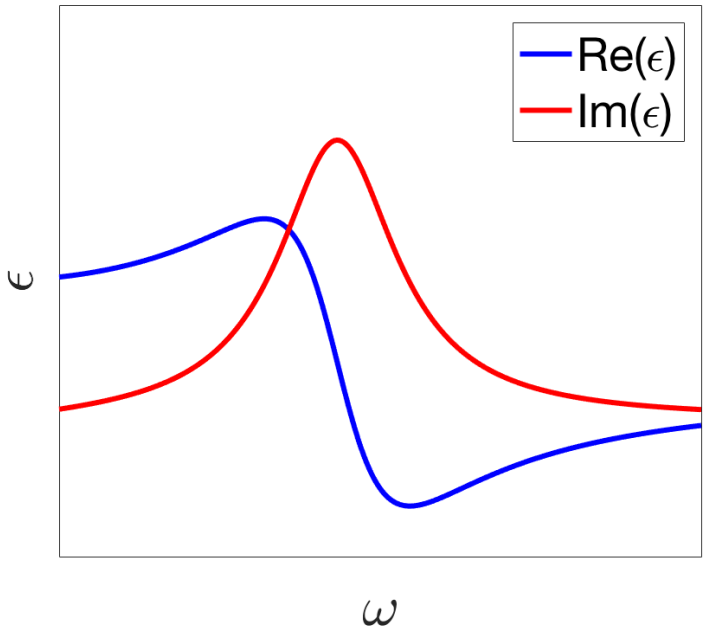

Figure 2. 1 Schematic illustration of typical permittivity spectrum showing the relation of real and imaginary parts of permittivity.

Light matter interaction may be quantified by the near field enhancement and the maximum achievable scattering efficiency in the far field from a subwavelength nanoparticle, both of which are strongly dependent on the material parameters, namely dielectric constant, or permittivity. The permittivity is a physical measure of the electric polarizability of a material, which can be modeled as a harmonic mass-spring system. Its quantum-formula is given through this relation (called Drude - Lorentz dispersion model) [58-61],

$$\varepsilon(\omega) = \varepsilon_\infty + \frac{\omega_p^2}{\omega_t^2 - \omega^2 + i\Gamma_0\omega} \tag{2.1}$$

where ε_∞ is the high frequency limit of ε; $\omega_p = \sqrt{Ne^2/\varepsilon_0 m}$ (N: electron density; e: electron charge, ε_0: vaccum permittivity; m: electronic mass) is plasma frequency; ω_t is the resonant frequency of the oscillator; ω is the angular frequency of light; Γ_0 is the damping factor. A schematic illustration of the real (Re(ε)) and imaginary (Im(ε)) part of dielectric constant is shown in Figure 2.1 and they follow the Kramers-Kronig relations (KKR) analytically [62, 63]. KKR is often used to calculate the real part of permittivity (ε_r) from imaginary part of permittivity (ε_i) (or vice versa) in stable physical systems, which is implied by the causality induced analyticity condition [64]. When $\omega_t = 0$, this model evolves to Drude model [59, 60], which solely takes into account free electrons in the light matter interaction and thereby is only applicable to metals.

The low (ε_s) and high frequency (ε_∞) limits of the permittivity are given by,

$$\begin{cases} \varepsilon_s = \varepsilon(\omega \to 0) = \varepsilon_\infty + \dfrac{\omega_p^2}{\omega_t^2} \\ \varepsilon_\infty = \varepsilon(\omega \to \infty) \end{cases} \tag{2.2}$$

By substituting equations (2.2) into (2.1), the complex dielectric function then can be expressed in terms of the constants ε_s and ε_∞ as follows,

$$\tilde{\varepsilon}(\omega) = \varepsilon_\infty + \frac{(\varepsilon_s - \varepsilon_\infty)\omega_t^2}{\omega_t^2 - \omega^2 + i\Gamma_0\omega} \tag{2.3}$$

If there is more than one oscillator, the dielectric function is assumed to be equal to the sum of the contributions from each individual oscillator, which fits better for the real materials. A Lorentz model with *N* oscillators is described in the following,

$$\varepsilon(\omega) = \varepsilon_\infty + \frac{\omega_p^2}{\omega_t^2 - \omega^2 + i\Gamma_0\omega} + \sum_1^{N-1} \frac{f_j \bullet \omega_{0j}^2}{\omega_{0j}^2 - \omega^2 + i \bullet \gamma_j \bullet \omega} \tag{2.4}$$

where *N* is the number of the oscillators; f_j, ω_{0j} and γ_j are the oscillator strength, the resonance frequency, and the damping coefficient of the j_{th} oscillator [58]. The first two terms in Equation (2.4) denote the intra-band effect of the free-electron-like nature with the Drude model and last one describes the inter-band effect of bound electrons with the Lorentz model. The high frequency limit constant, ε_∞, is usually equal to 1 but can be greater than 1 if oscillators in higher energies exist and are not taken into account. The difference, $\varepsilon_s - \varepsilon_\infty = \omega_p^2/\omega_t^2$ describes the strength of the single Lorentz oscillator. The resonant frequency, ω_t (or ω_{0j}) corresponds to the absorption peak position of the

corresponding oscillator. Γ_0 and γ_j are the broadening of each oscillator resulting from the absorption process involving transitions between two states. It is equal to the full width at half maximum (FWHM) of the corresponding peak. The oscillator strength f_j represents the relative amplitude of the j_{th} oscillator. A table of the parameter data sets from several experimental literatures can be found in reference [65, 66]. Figure 2.2 shows an example of the refractive index (square root of permittivity) of crystalline Si in the UV range, which is represented by a three-pole oscillator. This model's prediction (solid lines) is in great agreement with the reported experimental data [65, 66].

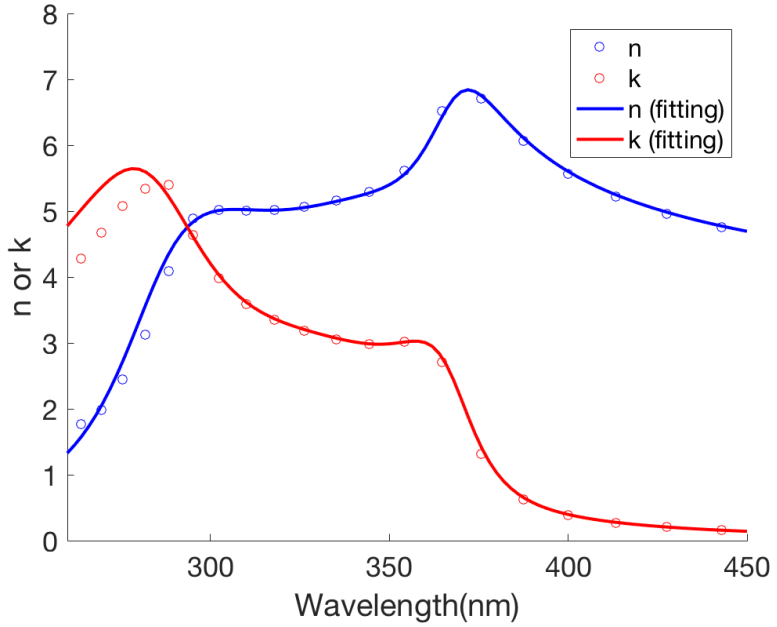

Figure 2. 2 Real (n) and imaginary (k) parts of refractive index spectrum of single crystal Si. The scatterers are measured data and the solid lines are fitted from the three-pole model.

2.2 Optical bowtie antenna with artificial lossy materials

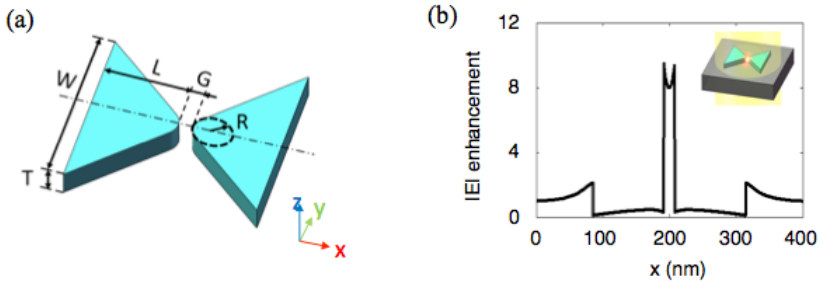

Figure 2. 3 Simulation of bowtie nanoantennas. (a) Geometry of the bowtie structure with the symmetry axis (represented as a dash-dot line) as the x-axis of right-hand coordinate system. (b) Line scan of the E-field amplitude enhancement along the bowtie symmetry axis at half thickness at the working frequency of 840 THz. Inset: schematic of the simulated physical scenario.

In both metallic and dielectric systems for photonic applications, research efforts so far have been focused on minimizing the material loss, in another word, avoiding the absorption peaks in the permittivity spectrum [57]. Here, we show that, counter-intuitively, large ε_i in dielectric nanostructures may contribute to field enhancement and confinement effectively, and the small light enhancement factor (EF) in existing dielectric systems[10, 16], can be greatly improved with the introduction of large ε_i. We first analyze this phenomenon using widely investigated optical nanoantennas [8, 67, 68] as examples, which can bridge light fields at mismatched scales and realize electromagnetic (EM) confinement and enhancement in a deep subwavelength "hotspot".

A typical bowtie optical antenna used in our simulations (COMSOL Multiphysics™ [69]) is depicted in Figure 2.3(a), consisting of two tip-to-tip triangles separated by a small gap of 9 nm (G) [8] . The width (W), length (L) and thickness (T) of the bowtie are 115 nm, 53 nm and 20 nm, respectively, and round tips with 11 nm radius (R) are used to imitate real fabrication. The bowtie is placed on a substrate (refractive index n = 1.5) in air (n = 1) and excited by an *x*-polarized EM wave along +*z* direction. The material permittivity is first set artificially to demonstrate the effect of material permittivity (the real and imaginary parts of permittivity do not follow the Drude-Lorentz model discussed in the previous sections). In the simulation results shown in Figure 2.3(b), the permittivity is 10 + *i*30.

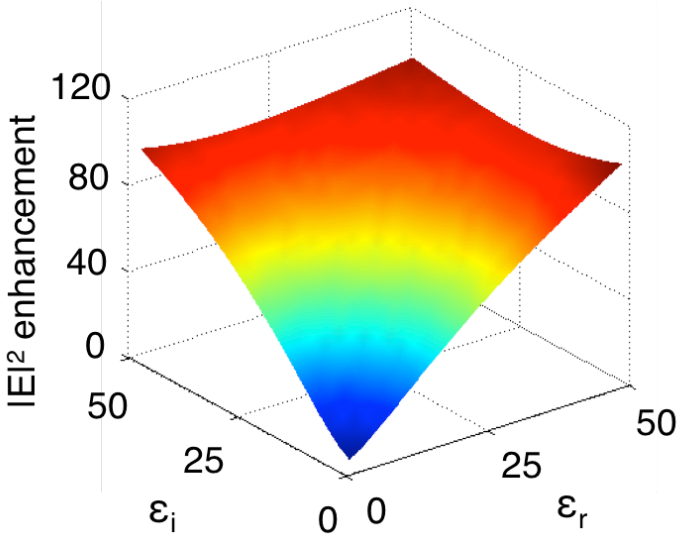

Figure 2. 4 $|E|^2$ enhancement factor inside the bowtie gap plotted as a function of real and imaginary parts of permittivity.

As shown in Figure 2.4, the intensity EF is plotted as a function of real and imaginary parts of permittivity. Here, the amplitude/intensity EF is defined as the ratio of the local E-field amplitude/intensity, to the E-field amplitude/intensity at the same geometrical point without bowtie in the simulation. The larger real and imaginary parts of permittivity bring out stronger field enhancement inside the bowtie gap. Figure 2.5 shows the cross-sectional field distribution for a same bowtie structure with different permittivities. It can be explained by the displacement continuity conditions. According to Maxwell equations, the current displacement is continuous across the

boundary ($\varepsilon_1 E_1 = \varepsilon_2 E_2$) for the polarization normal to the interface. If the permittivity of one medium increases, the field at the interface inside the other medium goes up to match the continuity equation. The cross-sections of electric field distribution for different permittivities are shown in Figure 2.5.

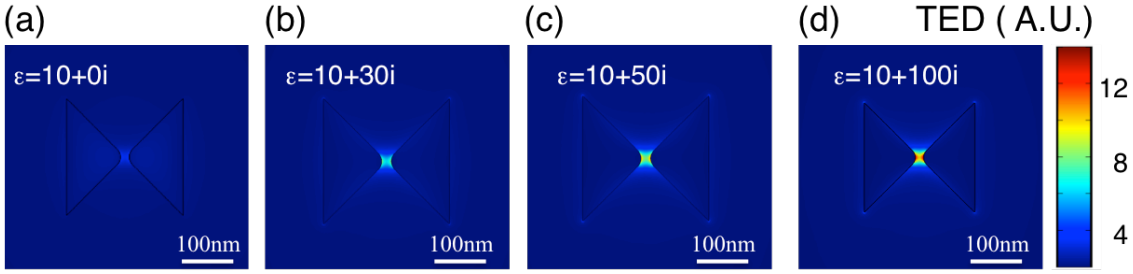

Figure 2. 5 Cross-sectional field distribution for a same bowtie structure with different permittivities. (a) ε = 10 + 0i (b) ε = 10 + 30i (c) ε = 10 + 50i (d) ε = 10 + 100i.

Previous application of large permittivity materials for subwavelength confinement faced great challenges to solely obtain a large ε_r, while in real materials a large ε_r is always associated to a large loss. Our justification of the role of a large ε_i in nanoantennas solved the problem, allowing a new paradigm of material selection in subwavelength light confinement and enhancement applications. Since a large ε_i is much easier to experimentally achieve than a large ε_r, the contribution of ε_i is even more effective in practice. Note that the saturation effect in Figure 2.4 where |ε| is very large owes to the compression of almost all the EM energy to the gap or the edge by impedance mismatch, and greater mismatch makes no substantial difference.

2.3 Performance evaluation of bowtie nanoantennas with real materials

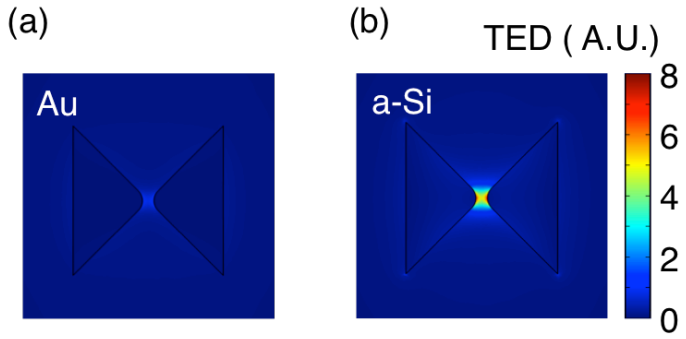

Figure 2. 6 Cross-sectional time-average EM energy density (TED) distribution of Au and a-Si bowties at 840 THz (3.5 eV), where a-Si bowtie has a better performance for light confinement.

Since the real material permittivity follows the KKR, real material systems are discussed in this section. Si is selected as our example because of its wide applications and large dissipative loss at UV (shown in Figure 2.2) due to the inter-band transitions [70]. Specifically, amorphous Si (a-Si) [71] is utilized for easier potential experimental realization and being readily modeled with one oscillator pole. It's illuminating to

compare a-Si, Au, Al [72] (noble metals), and HfO_2 [73] (lossless dielectrics), and artificial dispersive dielectrics following similar but weaker Lorentz oscillation shown in Equation (2.3). To make such artificial materials, ε_∞, ω_t, and Γ_0 are fixed to be 1.1, 890 THz and 440 THz, respectively, while ε_s is a tunable number as 2, 6, or 10. Thus, their frequency-dependent permittivities are similar to that of a-Si, as shown in Figure 2.7(a), which also depicts the plasmonic inactivity of Au in UV regime. Note that when a-Si permittivity is fitted by Equation (2.3), the corresponding ε_s equals to 19.5. Figure 2.6 shows the field distribution for a same bowtie made of Au and a-Si respectively, indicating the better performance of a-Si in field confinement over Au.

Figure 2.7(b) quantitatively shows the intensity EFs (calculated at the bowtie geometric center) as functions of the incident photon energy, demonstrating the lossy a-Si bowtie with a large ε_i achieves higher intensity EFs than bowties made of Au and artificial materials, and shows comparable performance with the Al bowtie at higher frequencies (the Al bowtie has a resonance around 4.5 eV). Ag is outperformed by Al in UV range and is thus not discussed here for clarity [74]. All lossy dielectric bowties show similar enhancement behavior in all frequencies studied here and the EF increases by 10-20 folds over a broad range with larger ε_i. Most importantly, such large enhancement is achieved in UV range, which is a long-term research aim in fields such as bioimaging and biosensing [75], due to plasmonic inactivity of noble metals in this region [74, 76, 77]. Even though Al has been considered as one solution [75], it possesses similar limits in deep UV and other problems of cytotoxicity [78], severe oxidation [79, 80], and device fabrication challenges when scaled down for short wavelength applications [54]. Therefore, our proposed lossy dielectrics overwhelm conventional materials (Au, Ag, Al, etc.) in those aspects [81] and can be easily achieved in UV or deep UV [70] .

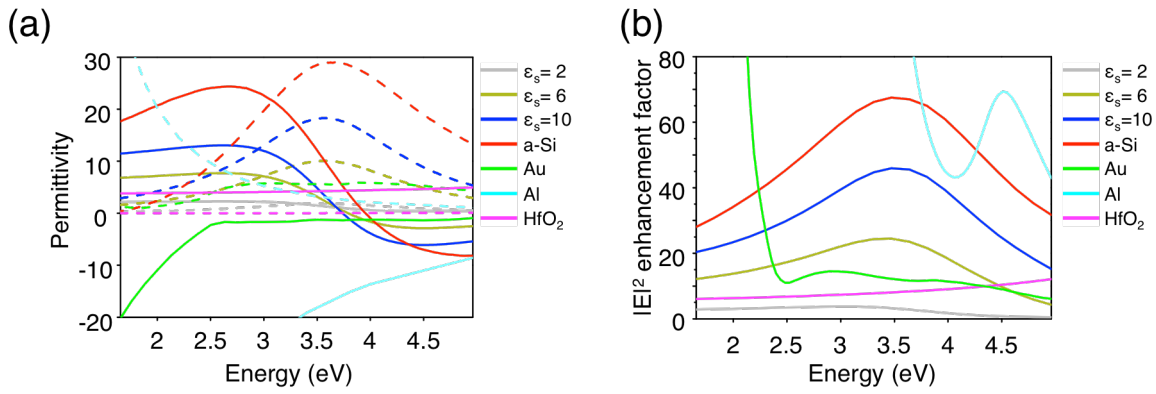

Figure 2. 7 Performance of lossy bowtie nanoantennas. (a) The permittivity of materials involved in the numerical calculation. The solid and dashed lines indicate ε_r and ε_i, respectively. (b) Intensity EF vs. incident light energy for bowties made of the materials in (a).

To characterize the field confinement ability of an optical antenna (with resonances), three most important parameters are studied here, quality factor (Q) [82], effective mode volume (V_{eff}) [82] and Purcell factor (F_p) [82, 83]. Q and V_{eff} describe the decay rate and peak electric field strength within the Bowtie antenna resonator, respectively.

F_p is of great importance for measuring the capability of the antenna to enhance the spontaneous emission rate and is defined as the magnitude of enhancement of spontaneous emission rate of the atom incorporated inside the antenna [83]. Q is defined as $Q = \omega/\Delta\omega$, where ω and Δω are the angular frequency of light and spectral width of the antenna respectively. It is straightforward to derive the value of ω and Δω from the spectrum of field enhancement and then calculate Q. Effective mode volume is given in the following,

$$V_{eff} = \frac{\int_V \varepsilon(r)\left|E(r)\right|^2 d^3r}{\max[\varepsilon(r)\left|E(r)\right|^2]} \tag{2.5}$$

where ε(r) is the dielectric constant, |E(r)| is the electric field strength, and V is a quantization volume encompassing the antenna and with a boundary in the radiation space of the antenna mode. In Equation (2.5), on the right-hand side, the nominator is the integration of energy density over the effect volume and the denominator is the maximum energy density. These two values can be directly extracted from the COMSOL simulation results. Once Q and V_{eff} are calculated, it is straightforward to obtain F_p using the formula as follows,

$$F_p = \frac{3Q\lambda^3}{4\pi^2 V_{eff}} \tag{2.6}$$

V_{eff} and F_p are also computed in Figure 2.8(a). Two orders of magnitude decrease in V_{eff} is achieved in lossy dielectric antennas with a larger ε_i, surpassing the widely accepted $V_{\text{eff}} \sim (\lambda/2)^3$ limit for dielectric resonators (λ is the EM field wavelength) [7]. A growing Purcell factor with an increasing ε_i verifies that better light confinement and funneling of energy from the propagating light to the hotspot are achieved in lossy dielectric nanoantennas. The Purcell factor of the a-Si bowtie antenna is comparable to those of some metallic nanoantennas working in the visible range or even longer wavelengths [84, 85].

Besides light confinement and enhancement, device level absorption loss has to be evaluated as compared to ε_i. Here we introduce an "enhancement-loss Figure of merit (FOM)" to evaluate those lossy dielectric bowties in Figure 2.8(b), which is defined as the ratio between the intensity EF and the total energy absorbed by an optical antenna. It is evident that, a larger ε_i leads to a larger FOM, meaning light confinement with unit material absorption loss is boosted, and the FOM of the a-Si bowtie is 5 times that of the Au bowtie. The increase of FOM by lossy dielectrics owes to the better enhancement as well as the limited total absorption loss. To clarify that, we plot the total absorption loss of a dielectric bowtie with a fixed real part of permittivity (ε_r) as a function of εi in the left inset of Figure 2.8(b), showing that the total loss will first reach a maximum and then decrease with larger ε_i, which can be explained by the competition between material absorption loss and impedance mismatch. The total absorption loss first increases with larger ε_i. However, as ε_i keeps rising, more EM energy is "compressed" into the gap and less EM energy is coupled into the bowtie (right inset of Figure 2.8(b)) because of the huge impedance mismatch between the lossy bowtie and its surroundings. Consequently, an ultra-lossy dielectric bowtie only generates limited

heat (material absorption loss is assumed to be the only heat source in optical antennas [16]), which, along with other advantages including thermal stability and chemical resistivity [86], promises the practical application of robust lossy dielectric nanoantennas.

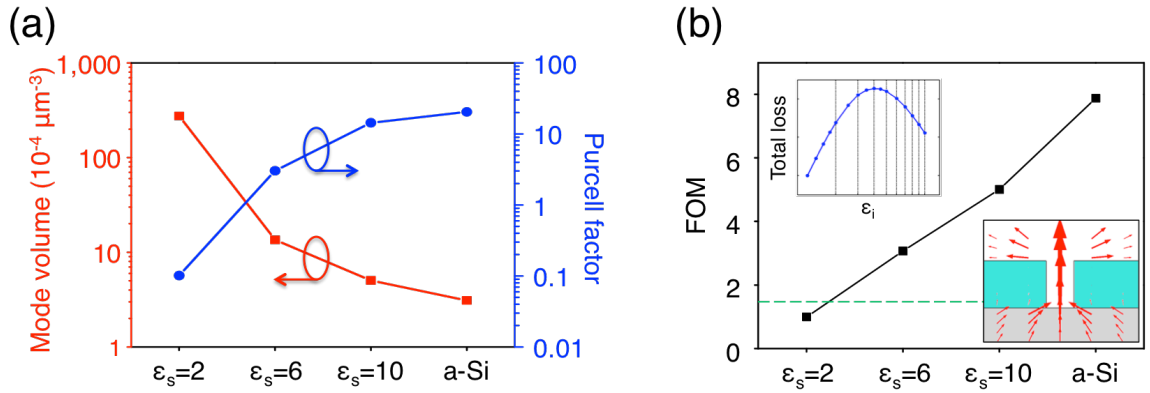

Figure 2. 8 Extracted mode volumes, Purcell factors and FOM. (a) Intensity EF vs. incident light energy for bowties made of the materials in Figure2.7. (b) FOM at 840 THz with the dashed line indicating the value of Au bowtie. Note that the values are normalized to the smallest one. Inset in (c): total loss vs. ε_i (left), and schematic of local power flow around the gap of a highly lossy dielectric bowtie (right).

2.4 Florescence enhancement demonstration with lossy dielectric antennas

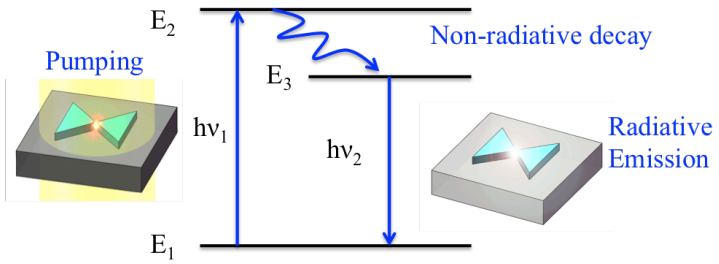

Figure 2. 9 Illustration of fluorescence enhancement involcing two processes: pumping and emission.

One of the most important applications of optical antennas is biomolecule fluorescence enhancement [8] and lossy dielectric antennas show such great potential as other plasmonic and lossless dielectric ones. The fluorescence enhancement involves two processes: pump excitation (already discussed above) and fluorescence emission, shown in Figure 2.9 [8]. Since pump and emission wavelengths are normally close to each other, they are both set to be 840 THz in the following analysis. To simulate fluorescence emission, a dipole source is placed at the bowtie center and the far-field radiated power in absence and presence of the bowtie are examined [8]. The radiated and non-radiated power EFs (normalized to the far-field radiated power in absence of bowtie antennas by definition) are calculated to obtain the quantum efficiency EF with the assumption that the intrinsic quantum efficiency (η_0) of the sample is 2.5% [8]. The quantum efficiency (QE) is calculated using the equation as follows [8] ,

$$QE = \frac{f_r}{f_r + f_{nr}} \tag{2.7}$$

where f_r and f_{nr} are radiative and non-radiative factors, normalized to the radiative power in absence of antenna. The *QE* enhancement factor is written in the following,

$$f_\eta = \frac{f_r}{\left(1-\eta_0\right)+\eta_0\left(f_r + f_{nr}\right)} \tag{2.8}$$

Therefore the total fluorescence enhancement ratio is as below,

$$f = f_\eta \times f_E \tag{2.9}$$

The total fluorescence EF is evaluated by multiplying the EF of pump excitation intensity (f_E) with the quantum efficiency EF (f_η), as shown in Figure 2.10. The large ε_i of a-Si leads to improvement in both radiative and non-radiative EFs, resulting in a total fluorescence EF of 636, much larger than those of the Au antenna (8) and the HfO_2 antenna (75), indicating its great potential in UV applications such as fluorescence detection from Tryptophan in proteins, which has been troubling a lot due to plasmonic inactivity in UV or oxidation of metals [87] .

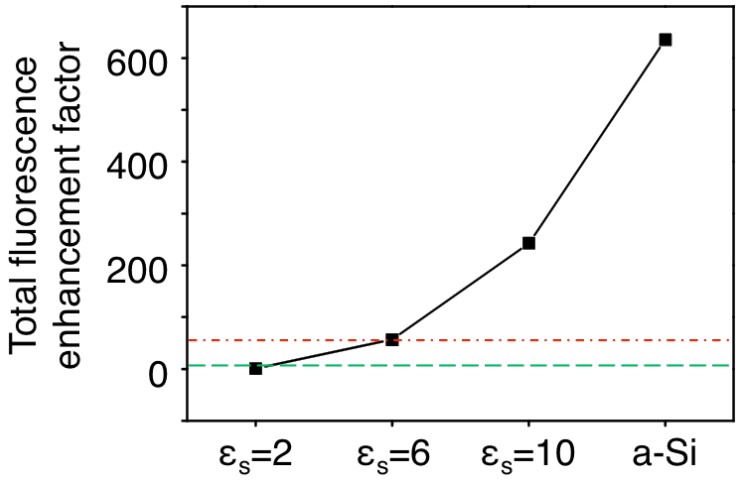

Figure 2. 10 Calculated fluorescence EFs with the green dashed and red dash-dot lines indicating the values of Au and HfO_2 bowties, respectively.

2.5 Conclusions

In this chapter, we show that, compared with Au (noble metal), HfO_2 (lossless, high refractive index dielectric) and artificial lossy dielectrics with weaker Lorentz oscillation strength, the a-Si nanoantenna has a much stronger ability to confine and enhance UV light with a better Purcell factor and larger fluorescence enhancement. As an example, a lossy dielectric nanoantenna made of a-Si displays remarkable light-matter interaction performance in UV range with a Purcell factor and fluorescence enhancement larger than those of Au and HfO_2 antennas. Such lossy dielectrics are easy to achieve using Lorentz oscillator model with large ε_r and ε_i almost simultaneously in multiple frequencies, providing a better option when other material systems fail to achieve enough performance. For example, in deep UV where Al is already inactive,

lossy dielectrics such as SiO_2 [88]and SiC [89] still work, with bio-compatibility [90, 91], CMOS compatibility and harsh environment endurance. Furthermore, based on the interband absorption induced large ε_i, engineering the band structure of the material will enable great tunability in the working frequency of those devices. This finding paves the way towards a completely new category of optical devices based on dissipative dielectrics, which will further enrich the ways nanophotonic research is done and enable future large-scale applications that do not exist today.

Chapter 3

Field confinement analysis of non-resonant dielectric nanogap structure

3.1 Dielectric nanogap structure (NGS)

The bowtie antenna structure studied in Chapter 2 utilized both of the material's large permittivity and geometric resonance even if it is weak due to the material loss (as shown in Figure 2.7(b), there is a spectrum peak). To provide insight into the sole contribution of loss to light confinement and enhancement in dielectric antennas, we analytically explore a simplified non-resonant structure, i.e., a dielectric nanogap structure (NGS), consisting of two identical single-mode optical slabs separated by a small gap and surrounded by a bulk material (Figure 3.1) [10]. The complex permittivity distribution is:

$$\varepsilon(x)=\begin{cases}\varepsilon_1, & |x|\le a\\ \varepsilon_{2r}+i\varepsilon_{2i}, & a<|x|\le b\\ \varepsilon_3, & b<|x|<\infty\end{cases} \tag{2.5}$$

where ε_1, ε_{2r} and ε_3 are real parts of permittivity, and ε_{2i} denotes the imaginary part of permittivity in the slabs (ε_2).

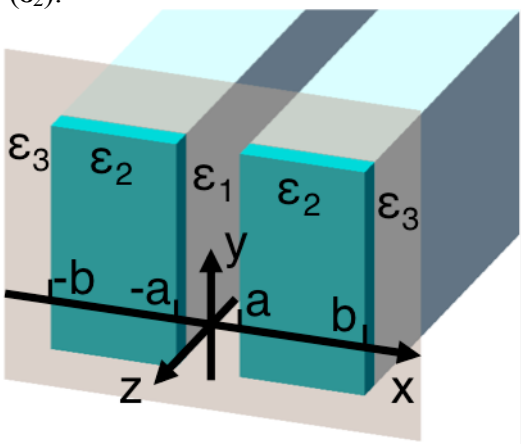

Figure 3. 1 Schematic of NGS infinitely long in the y direction. The shaded plane depicts a thin slice. The light propagates along the -z direction. The lossy slab width is (b-a).

For the NGS, the electric field is polarized across the gap, with a *y*-polarized magnetic field, and *x*-polarized and *z*-polarized electric field components (TM mode) [10]. Here, we obtain the field distribution with the existence of strong material loss by combining the boundary conditions with the wave equation and solving the characteristic dispersion relation [10]. With the Maxwell's equations and boundary conditions, we

can rigorously solve the field distributions at z = 0 mm analytically for the fundamental mode in such structure as follows,

$$E_{x0}(x)=A\begin{cases}\dfrac{1}{\varepsilon_1}\cosh(S_1x), & |x|\le a\\ \dfrac{1}{\varepsilon_2}\cosh(S_1a)\cos\left[S_2\left(|x|-a\right)\right]+\dfrac{S_1}{S_2}\dfrac{1}{\varepsilon_1}\sinh(S_1a)\sin\left[S_2\left(|x|-a\right)\right], & a<|x|\le b\\ \dfrac{1}{\varepsilon_3}\left\{\cosh(S_1a)\cos\left[S_2(b-a)\right]+\dfrac{S_1}{S_2}\dfrac{\varepsilon_2}{\varepsilon_1}\sinh(S_1a)\sin\left[S_2\left(|x|-a\right)\right]\right\}\exp\left[-S_3\left(|x|-b\right)\right], & |x|>b\end{cases} \tag{3.1}$$

where S_1 is the transverse wave number and S_2, S_3 are the field decay coefficient in the media with permittivity ε_2 and ε_3 respectively. The constant A is written as below,

$$A=A_0\frac{\sqrt{k_0^2\varepsilon_2-S_2}}{k_0} \tag{3.2}$$

where A_0 is an arbitrary constant and $k_0=2\pi/\lambda_0$ is the wave number in vacuum. S_i (i= 1,2,3) simultaneously follows the relations in the following,

$$k_0^2\varepsilon_1+S_1^2=k_0^2\varepsilon_2+S_2^2=k_0^2\varepsilon_3-S_3^2 \tag{3.3}$$

Another transcendental characteristic equation is used to calculate S_i,

$$\tan\left[S_2\left(b-a\right)-\arctan\left(\frac{S_3\varepsilon_2}{S_2\varepsilon_3}\right)\right]=\frac{S_1\varepsilon_2}{S_2\varepsilon_1}\tanh\left(S_1a\right) \tag{3.4}$$

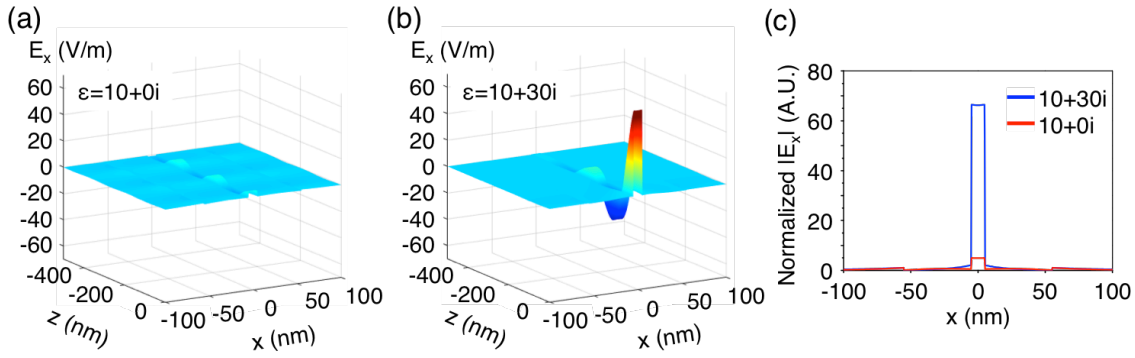

Figure 3. 2 E_x field distribution and performance of NGS. Analytically calculated 3D mapping of the field in NGS without loss (a) and with loss (b). (c), Line scan of the normalized E_x distribution in the plane of z = 0.

The ratio between the values of $|E_x|$ at the two sides of the interface equals to $[\varepsilon_{2r}^2+\varepsilon_{2i}^2]^{1/2}/\varepsilon_1$ across the interface. The permittivity contrast can be enlarged by introducing larger loss (ε_{2i}), which is experimentally more practical than simply looking for a large ε_r. An analytical three-dimensional (3D) spatial distribution of E_x for a symmetric fundamental mode (TM) at 840 THz is given in Figure 3.2 (b) and (c) in two different scenarios: without loss (ε_2 = 10 + 0i) and with loss (ε_2 = 10 + 30i). Here, we assume that ε_1 = ε_3 = 1, a = 5 nm, b = 55 nm. As depicted in Figure 3.2, the E_x inside

the gap at the NGS entrance is amplified with the introduction of loss. Although E_x decays in the propagation direction, very thin lossy slabs along z direction (the cross-sectional plane in Figure 3.1) can be utilized to compress and enhance the optical field in subwavelength scale volumes. It is geometrically similar to typical nanoantennas, without substantial influence from the propagation decay. In Figure 3.2(c), we depict the normalized E_x distribution in the plane of $z = 0$, which again shows the positive influence of loss. Note that the above values of calculated Ex are normalized to the ones at |x| = b (in the air).

3.2 Mode area and optical energy distribution investigation

We further calculate the effective refractive index (n_{eff}) for more details about the propagation and field distribution, and plot the results as functions of ε_{2i} in Figure 3(e). The imaginary part of n_{eff} first increases and then decreases when ε_{2i} goes up. This effect can also be explained by the competition between the field distribution and the increasing impedance mismatch by larger loss. In other words, the material loss not only enhances the field, but also eventually leads to less absorption loss and dissipation of energy.

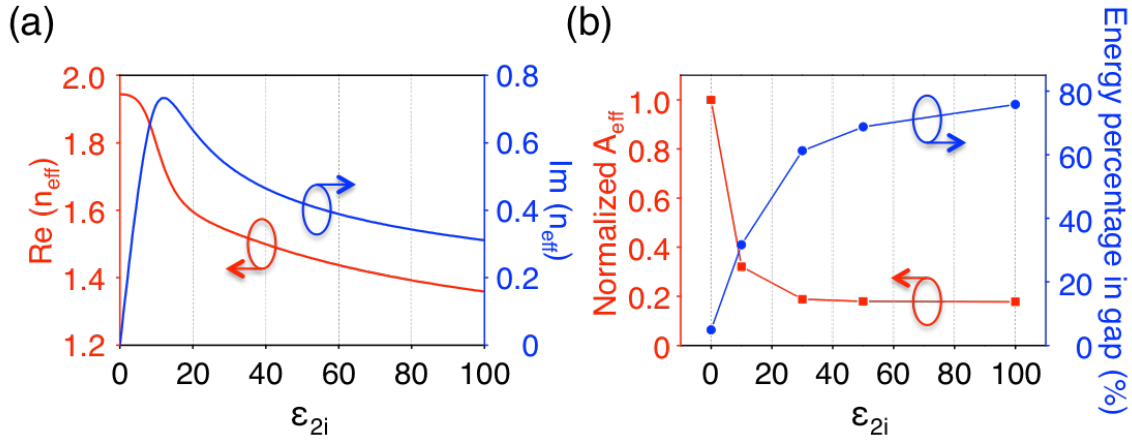

Figure 3. 3 (a) Real and imaginary parts of n_{eff} plotted as functions of ε_{2i}. (b) The effective mode area of NGSs and energy percentage in the gap plotted as functions of ε_{2i}. The effective mode areas and energy percentages are normalized to the lossless case.

To verify the subwavelength light confinement in NGSs, we calculate the cross-sectional mode area ($A_{eff} = \iint WdA/W_{max}$, W is energy density and W_{max} is the maximum energy density in the cross section of NGS). Figure 3(f) shows the simulated dependence of A_{eff} on the loss (ε_{2i}). With an increasing ε_{2i}, the energy of EM field is effectively compressed from the slabs into the gap, confirmed by the decreasing A_{eff} and increasing normalized power inside the gap, which goes up from ~5% to ~78% as ε_{2i} increases from 0 to 100, highlighting the great potential of the loss induced energy confinement. That light confinement is also attributed to the impedance mismatch and the field discontinuities across the interface between the lossy slabs and the gap. These two mechanisms provide a clear explanation of the physics behind.

3.3 Conclusions

In summary, we demonstrated and analyzed large subwavelength light confinement and enhancement inside dissipative dielectric nanostructures with the counter-intuitive contribution from ε_i, leading to a plethora of new materials suitable for nanophotonic applications. Corresponding lossy nanogap structure models are analytically studied, which demonstrates quantitatively that, the favorable light enhancement properties of the lossy dielectric antennas are due to larger dielectric discontinuities and impedance mismatch. In agreement with the analysis in Chapter 2, loss helps create large dielectric discontinuity and impedance mismatch at the material boundaries and, therefore, greatly boosts the EM field intensity in the nanostructure hotspots. Even if no resonance exists in the nanostructure, the material loss is still able to improve the field concentration in the hotspots, which evidences the positive of material loss solely.

Chapter 4

Circuit model for dispersive antennas

4.1 Circuit model for a single dielectric nanorod

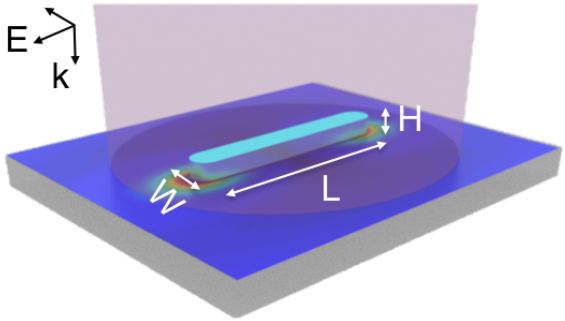

Figure 4. 1 Schematic configuration of a nanorod and its scattering field.

In chapter 2 and 3, the field localization enabled by material loss is investigated in detail. Meanwhile, the manipulation of the far field scattering may be readily tailored with the introduction of material loss as well. Here, we first investigate the far-field scattering efficiency of a nanorod consisting of a material with arbitrary permittivities, as depicted in Figure 4.1 (the ambient environment is air).

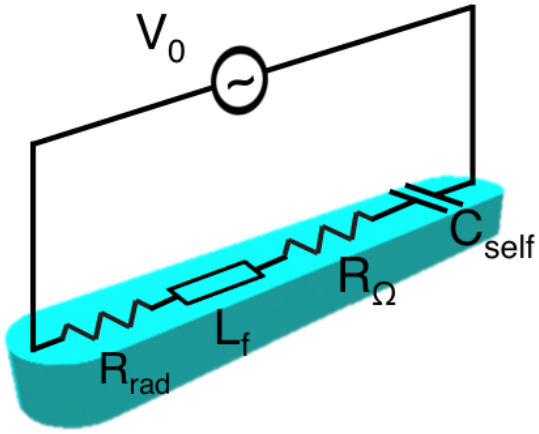

Figure 4. 2 Circuit model for a nanorod with length (*L*), width (*W*) and height (*H*).

A circuit model is built to calculate the scattering efficiency of a nanorod with certain length (L), width (W) and height (H), depicted in Figure 4.2 [92]. As shown in Figure 4.2, the circuit contains an alternating current (AC) voltage source, which models the incident plane wave, a parallel capacitor (C_{env}) in the environment and the impedances on the nanorod including radiation and material impedances. Radiation impedance consists of radiation resistance (R_{rad}) and self-inductance (L_f), both of which are independent of material property [93]. Only the radiation resistance contributes to the optical scattering field. The material impedance is composed of Ohmic resistance (R_ω) and reactance (X_{self}). The material reactance is capacitive (C_{self}) for dielectrics and inductive (L_{self}) for metals. Variation of the material permittivity changes the material impedance and thereby affects the scattering field.

Table 4.1 Notations and definitions for the circuit model.

Notation	Definition
C_{env}	Capacitance from the environment
R_{rad}	Radiation resistance
L_f	Self-inductance
R_Ω	Ohmic resistance
C_{self}	Capacitance inside the nanorod
Z_{rad}	Radiation impedance
Z_{mat}	Material impedance
Z_o	Vacuum impedance, 377 Ω
P_{rad}	Radiation (Scattering) power
L, W, H	Length, width and height of nanorod
a	Lattice constant in metasurface

The table 4.1 defines the parameters in the model. Radiation impedance is only determined by the geometry of nanorod [93]. Radiation resistance (R_{rad}) and self-inductance (L_f) are as follows [93],

$$R_{rad} = \frac{Z_m}{2\pi \sin^2\left(kL/2\right)}\left\{\gamma + \ln(kL) - \mathrm{Ci}(kL) + \frac{1}{2}\sin(kL)\left[\mathrm{Si}(2kL) - 2\mathrm{Si}(kL)\right] + \frac{1}{2}\cos(kL)\left[\mathrm{Ci}(2kL) - 2\mathrm{Ci}(kL) + \gamma + \ln(kL/2)\right]\right\} \tag{4.1}$$

$$L_f = \frac{Z_m}{2\pi\omega \sin^2\left(kL/2\right)}\left\{\mathrm{Si}(kL) + \frac{1}{2}\cos(kL)\left[2\mathrm{Si}(2kL) - \mathrm{Si}(2kL)\right] + \frac{1}{2}\sin(kL)\left[\mathrm{Ci}(2kL) - 2\mathrm{Ci}(kL) + \mathrm{Ci}(2kr_{eff}^2/L)\right]\right\} \tag{4.2}$$

where γ is the Euler constant; Si(x) and Ci(x) are sine and cosine integral functions. The effective radius r_{eff} is defined in the following,

$$r_{eff} = f\sqrt{WH/\pi} \tag{4.3}$$

where f is a geometry fitting parameter that converts "brick-like" nanorod to an effective cylinder. f is 1.45 for Si nanorod with the length of 145nm.

Therefore, we can define the radiation impedance as,

$$Z_{rad} = R_{rad} + j\omega L_f \tag{4.4}$$

The material impedance can be calculated from complex conductivity from Ampere's law:

$$\nabla \times H = j\omega\varepsilon_0\varepsilon E = \sigma E + j\omega\varepsilon_0 E \tag{4.5}$$

where ε is the complex permittivity of the material, σ is the complex conductivity. Therefore the material impedance is as follows,

$$Z_{mat} = \frac{1}{\sigma} \bullet \frac{L}{A} = \frac{1}{j\omega(\varepsilon - 1)} \bullet \frac{L}{W \bullet H} \tag{4.6}$$

where A, W, H are the cross-sectional area, width and length of the nanorod, respectively. Note that if the real part of permittivity is smaller than 1, then the material is inductive rather than capacitive (i.e. the reactance in Z_{mat} is positive), but it will not affect the scattering calculation. Assuming we have a circular polarized plane wave incident from the substrate (ε_{sub}), the decomposed linear polarization along the nanorod will be responsible for scattering (the response of nanorod to cross linear polarization is negligible). The amplitude of the circular polarized light is denoted as $\sqrt{2}E_0$, so that E_0 is the time-averaged electric field of that linear polarization component.

In this configuration, the power source can be modeled as an AC voltage source,

$$V_0 = L \bullet E_{eff} \tag{4.7}$$

where the E_{eff} is the effective electric field seen by the nanorod (fit from COMSOL simulation). The current (amplitude) is

$$I = \left| \frac{V_0}{Z_{rad} + Z_{mat}} \right| \tag{4.8}$$

The power scattered from the nanorod is equal to the power "dissipated" at R_{rad}, as follows,

$$P_{rad} = I^2 R_{rad} \tag{4.9}$$

In the real device, the substrate is silica with refractive index of 1.5. Hence, we define a the correction factor (g), which is the ratio of the forward scattering to the total scattering power and is obtained directly from COMSOL simulation (about 0.4 for forward scattering). Taking into account g yields the forward scattering power to the air,

$$P_{rad} = I^2 R_{rad} g \tag{4.10}$$

The real part of Z_{mat} is the Ohmic resistance that gives rise to dissipation loss:

$$P_{loss} = I^2 \,\mathrm{Re}\left(Z_{mat}\right) \tag{4.11}$$

The incident power on each unit can be calculated from time-averaged Poynting vector:

$$P_{in} = \frac{\sqrt{\varepsilon_{sub}}}{Z_0} E_{eff}^2 a^2 \tag{4.12}$$

Note that the incident power includes the cross-polarized light. Z_0 is free space impedance. Therefore, the total forward conversion efficiency can be calculated in the following:

$$\eta_{conversion} = \frac{P_{rad}^{forward}}{P_{in}} \tag{4.13}$$

The diffraction efficiency:

$$\eta_{diffraction} = \frac{P_{rad}^{forward}}{P_{in} - P_{rad} - P_{loss}} \tag{4.14}$$

The material property will strongly affect scattering efficiency.

4.2 Scattering efficiency calculation of a lossy dielectric nanorod with arbitrary permittivities

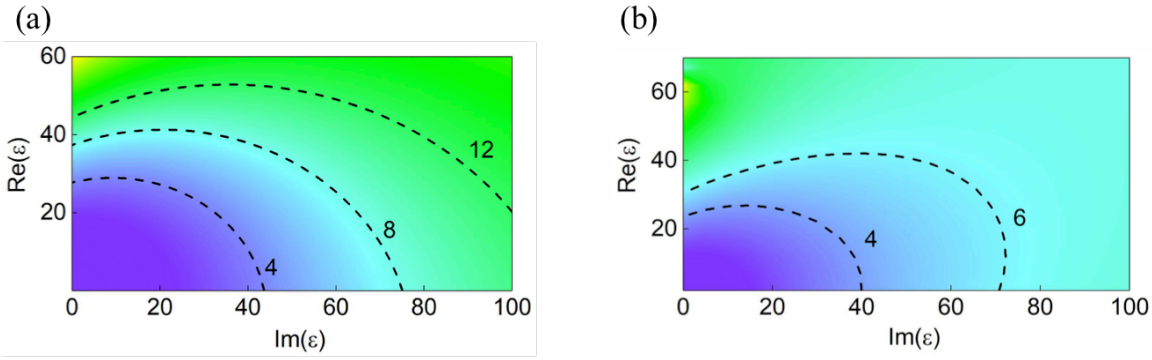

Figure 4. 3 Color mapping of scattering efficiency of a nanorod as a function of Re(ε) (ε_r) and Im(ε) (ε_i), with L = 130 nm, W = 30 nm and H = 30 nm at a wavelength of 380 nm. (a) Circuit model calculation result (b) COMSOL Simulation results.

Because Z_{mat} is a function of material permittivity, we can calculate the scattering efficiency of nanorod with different permittivities. The 2D mapping of scattering with complex permittivity is tenable, as shown in Figure 4.3. Figure 4.3 plots the color contour of the scattering efficiency of a rectangular nanorod as a function of the ε_r and ε_i at a wavelength (380 nm) close to the mercury *i*-line (this geometric size is close to the one for Si nanorod used in the metasurface design in Chapter 5). Here the scattering efficiency is defined as the ratio of the scattering cross section and the cross-sectional area of the scatterer [17]. As shown in Figure 4.3, not only ε_r but also ε_i contribute positively to the scattering efficiency in a dissipative system. Overall, the circuit result is in quite agreement with the one from COMSOL simulations. The discrepancy is due to the Mie resonances, which COMSOL is able to simulate but the circuit model is not.

We attribute this positive contribution of ε_i to the decreasing total impedance of the circuit ($|Z_{tot}|$) induced by the increasing ε_i, while the R_{rad}, which is independent of the material property, is constant (Figure 4.4). Therefore, scattered efficiency, which is proportional to the ratio of R_{rad} to Z_{tot} ($R_{rad}/|Z_{tot}|$), increases with the large ε_i, as illustrated in Figure 4.4. Similar behavior was theoretically discussed in reference [94]. This enables us to utilize common lossy dielectrics in the UV region to achieve high-efficiency metasurfaces, as discussed in Chapter 5.

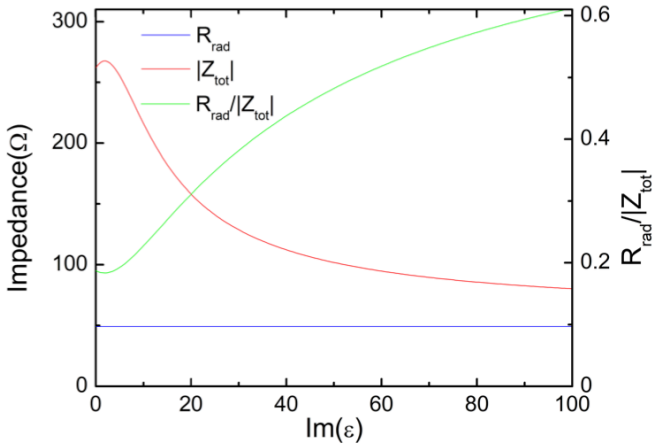

Figure 4. 4 R_{rad}, $|Z_{tot}|$ and $R_{rad}/|Z_{tot}|$ plotted as a function of ε_i when ε_r is fixed at 10.

4.3 Comparison of scattering efficiency calculation of a dielectric nanorod made of different materials

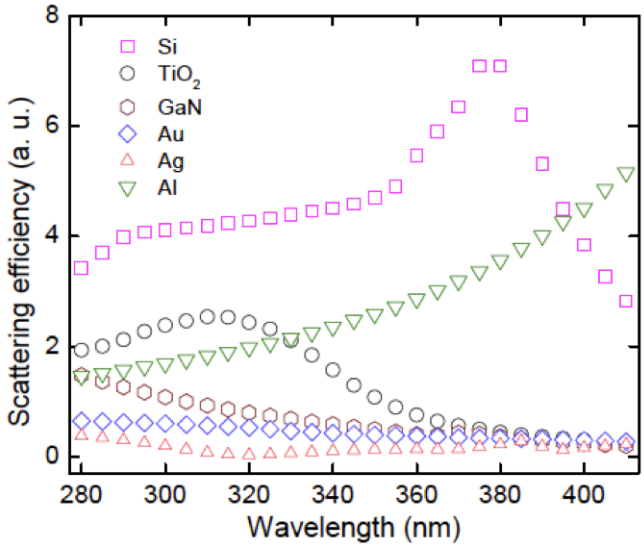

Figure 4. 5 Scattering efficiency of nanorods made of different materials, including Si, TiO_2, Au, Ag and Al with the same geometric parameters.

Due to its large permittivity at UV frequencies, CMOS compatibility and mature fabrication technologies, single crystal Si is chosen as the material platform studied here. To demonstrate the distinct property of Si at UV frequencies, we compare the single-nanorod scattering efficiencies of different widely used materials (Figure 4.5), including Si, TiO_2, Au, Ag, and Al, over a broad range of UV wavelengths from 280 nm to 410 nm. When the length is fixed at 130 nm, the Si nanorod outperforms all others, demonstrating the effectiveness of Si nanoantennas in the UV range and partially confirming the conclusion obtained from Figure 4.3 and Figure 4.4. *L*=130nm is chosen as the optimized length for the wavelength of 380 nm to maintain high efficiency over the broadband from 290 nm to 410 nm. A different length may be optimized for other wavelengths. The scattering efficiency spectra for different lengths are shown in Figure 4.6. When L = 100 nm, the Al nanorod has a resonance around 400 nm but it cannot be tuned to shorter wavelength (UV regime) because of the increasing absorption.

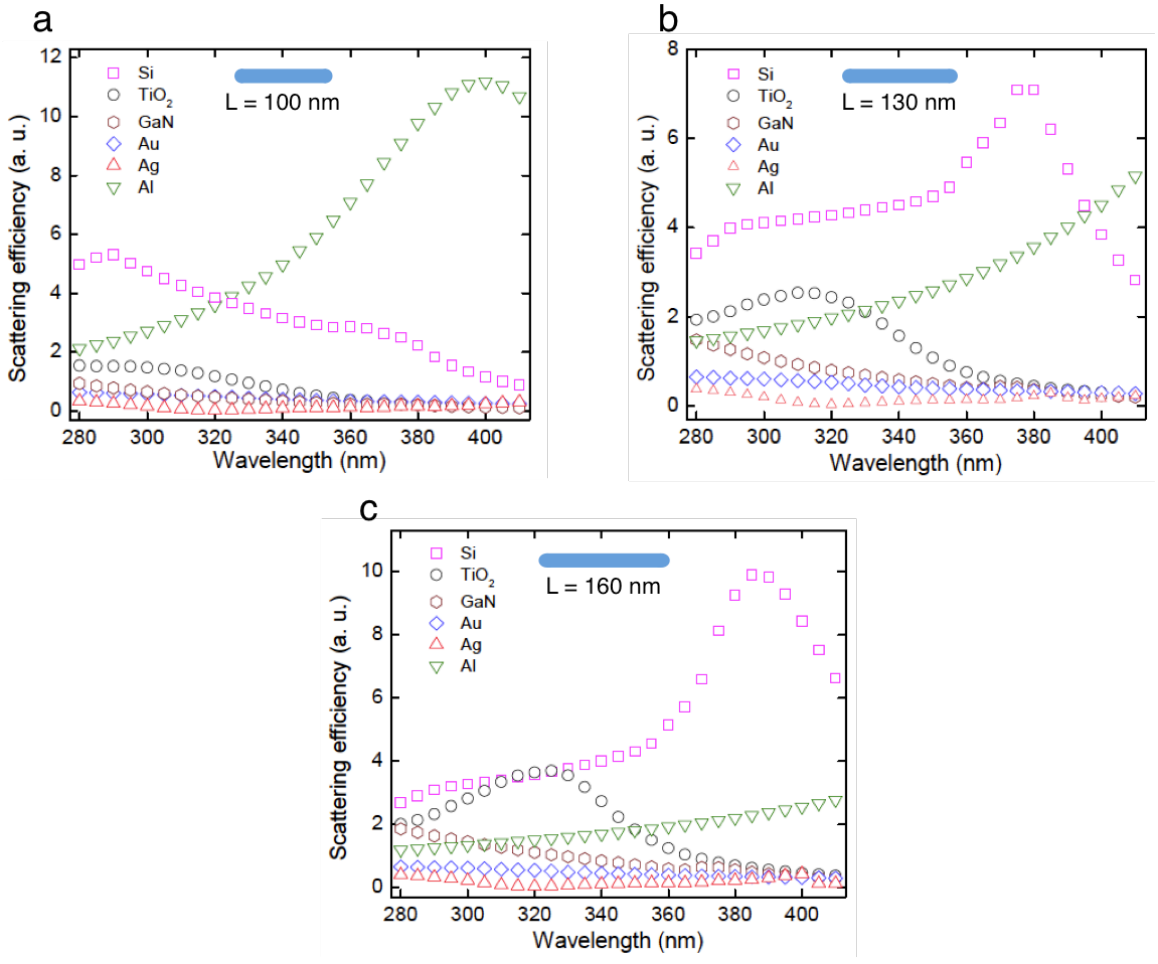

Figure 4. 6 Scattering efficiency spectra for a nanorod with different materials (L = 100nm (A), 130nm (B), 160nm (C)), including Si, TiO_2, Au, Ag and Al (FEM simulation results). It is in quite good agreement with the results in Figure 1D.

4.4 Conclusions

The scattering efficiency of a nanorod is investigated in this chapter. Both artificial and real materials are studied with circuit model and COMSOL software. A circuit model is built to confirm that the large permittivity is able to improve the far field scattering efficiency by decreasing the total impedance, which is in quite well agreement with the COMSOL simulations results. The analysis in this chapter lays the foundation for the design and understanding in improving the metasurface performance in Chapters 5 and 6.

Chapter 5

Design of all silicon ultraviolet metasurfaces

5.1 Light phase manipulation based on Pancharatnam-Berry phase

Among metasurface designs, the scatterer-orientation-controlled geometric phase (Pancharatnam-Berry phase) approach has been widely utilized to manipulate the phase of the scattered field for circularly polarized light [33, 36, 38-40]. A nanorod-shaped scatterer is able to control the phase of the scattered light with opposite helicity by only changing the orientation angle of the scatterer, and it is not subject to variations in size and material properties, upon which the scattering efficiency is dependent [33, 36, 37, 51]. This unique feature endows us with great freedom in optimizing the efficiency of the nanoantennas without sacrificing the phase control, as discussed in Chapter 4.

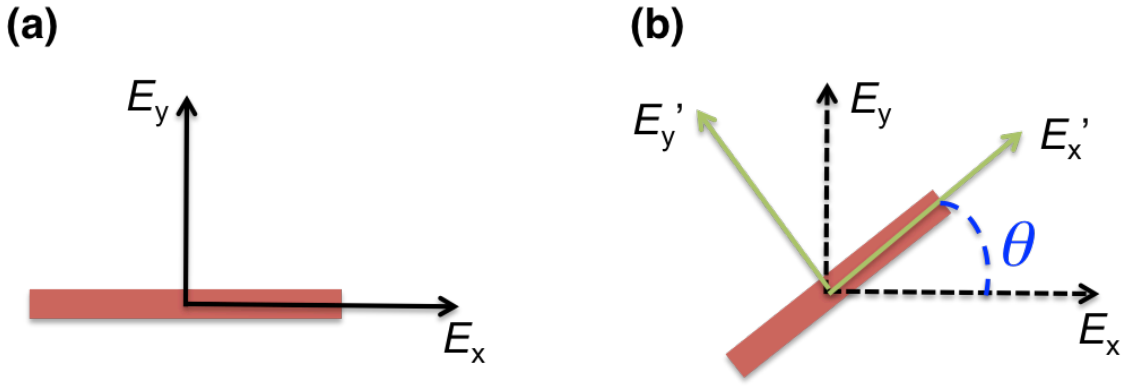

Figure 5. 1 Schematic of Nanorod (a) without rotation (b) with rotation angle θ. E_x and E_y denote the two polarized components of the incident electric field, which are along and perpendicular to the nanorod. E_x' and E_y' are the two components after rotation with an angle of θ.

The phase delay can be controlled with the rotation angle of the nanorod. Figure 5.1 depicts the impact of rotation angle on the phase delay using Jones matrix. We can start with the nanorod without rotation (Figure 5.1(a)) and its transmission matrix can be written as below,

$$J_0 = \begin{bmatrix} t_0 & 0 \\ 0 & t_e \end{bmatrix} \tag{5.1}$$

where t_o and t_e denote the transmission for two different polarizations respectively. Then when the nanorod is rotated by θ (Figure 5.1(b)), a new Jones matrix needs to be calculated. First of all, the two polarizations of the light are rotated to align with the local coordinate system of the nanorod (rotation of E_x - E_y to E_x' - E_y') and this operation is represented by a rotation matrix with rotation angle θ (the last term on the right hand side of Equation (5.2)). Then multiply it with the Jones matrix without rotation (J_0). Finally a clock-wise rotation matrix (with rotation angle of -θ) has to be multiplied to transform back to the original polarizations (rotation of E_x' - E_y' to E_x - E_y, described by the first term on the right hand side of Equation (5.2)). As such, the Jones matrix for a nanorod with rotation angle θ can be written as,

$$J = \begin{bmatrix} \cos\theta & -\sin\theta \\ \sin\theta & \cos\theta \end{bmatrix} J_o \begin{bmatrix} \cos\theta & \sin\theta \\ -\sin\theta & \cos\theta \end{bmatrix} \tag{5.2}$$

Then we can derive the electric field after the nanorod for the incidence with circular polarization in the following,

$$E_T^{R/L} = J \bullet E_I^{R/L} = \frac{t_o + t_e}{2} E_I^{R/L} + \frac{t_o - t_e}{2} e^{im2\theta} E_I^{L/R} \tag{5.3}$$

where $E^{L/R}$ represents left-hand and right-hand circularly polarized light, respectively ($E^L = 1/\sqrt{2}\begin{bmatrix}1 & -i\end{bmatrix}^T$ and $E^R = 1/\sqrt{2}\begin{bmatrix}1 & i\end{bmatrix}^T$). In Equation (5.3), the first term on the right hand side describes the transmission for the same polarization with incidence and while the second term indicates the transmission for the cross-polarized light which picks up an additional phase of 2θ. As such, the phase delay in each pixel can be manipulated and an array of nanorods is capable of shaping the beam precisely, leading to a series of applications, such as beam bending [36], metalens [37] and hologram [33]. Figure 5.2 shows an example of 2π phase delay coverage by 8 rotated antennas.

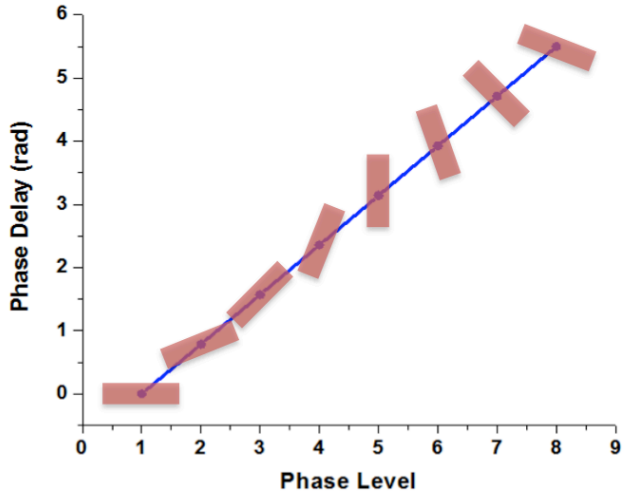

Figure 5. 2 Phase delay plotted a function of phase level (number of antennas, N, used to cover 2π phase delay). Here N = 8.

5.2 Design of metasurfaces for beam steering and metalens applications

Since each antenna with a rotation angle θ is able to impart a phase delay of 2θ, an aligned array of antennas with rotations angles covering π is able to bend the beam to certain direction with bent angle of α following the equation as below,

$$\alpha = a\sin\left(\frac{\lambda}{NP}\right) \tag{5.4}$$

where λ is the wavelength of the incident light, N is the number of antennas covering π rotation angle and P is the pitch size. Figure 5.3(a) shows the schematic configuration of an array for beam bending application. Here N constituent antennas are arranged together to tune the phase delay gradually from 0 to 2π (from left to right). Changing N and P allows for the tuning of bending angle. Equation (4) indicates that the bending angle is wavelength dependent as well. The rotation angle of the i-th antenna (i = 0, 1, 2 …N-1) is as follows,

$$\theta_i = \frac{i \bullet \pi}{N} \tag{5.5}$$

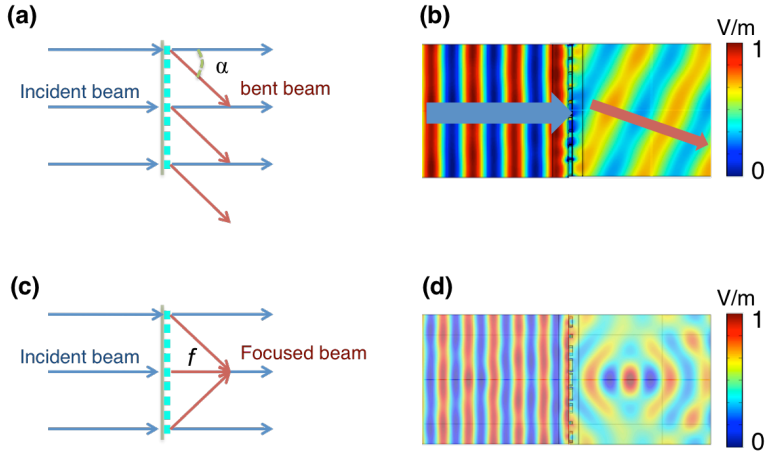

Figure 5. 3 Schematic illustration of (a) beam bending (c) Focusing with metasurfaces. Simulations of EM field for applications of (b) beam bending and (d) focusing. N = 8 antennas are used for beam bending and N = 9 for focusing. Wavelength is 380 nm and pitch size is 160 nm.

Once Figuring out the beam bending, it is straightforward to understand the antenna alignment of antennas for the focusing applications. Figure 5.3(c) and (d) depict the focused beam spot from the metasurface. A gradual phase delay from the antenna in the middle to the one on two sides can be engineered to make the metasurface act as a metalens, which is much thinner than the conventional lenses. The spatial phase profile can be written as,

$$\phi = -\frac{2\pi}{\lambda}\left(\sqrt{r^2 + f^2} - f\right) \tag{5.6}$$

where λ is the incident wavelength, r is the distance from the optical axis and f is the desired focal length.

In Figure 5(d), the designed focal length is 1 μm, which is predicted by the simulation very well. The beam waist is around 0.4 μm, which is close to the wavelength. Note that only an array of 9 antennas is considered in our simulation to show the focusing effect. If a two-dimensional array of antennas and more antennas are included in the metasurface, smaller beam waist and larger numerical aperture can be achieved.

5.3 Design of metasurfaces for hologram application

In addition to beam bending and focusing effects, another important functionality of metasurface is phase-only hologram generation without the need for a reference beam and an extra look-up table. The phase in each pixel can be manipulated individually, encoding the desired continuous local phase profile for circularly polarized illumination and thereby a phase mask can be designed to generate any desired pattern in the far field. It is similar to the computer-generated hologram with spatial light modulator. However, a subwavelength pitch size allows for only zero-order diffraction and wide field of view (FOV). Furthermore, the phase is independent of the dispersion, resulting in the potential applications for a broad-range of wavelengths [33].

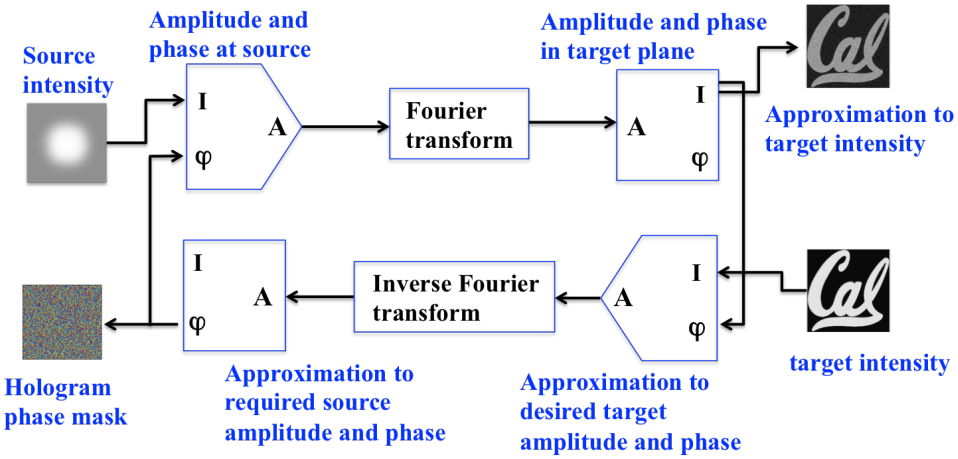

Figure 5. 4 Chart flow for conventional iterative Gerchberg-Saxton algorithm to retrieve the phase profile on metasurface based on the target image ("Cal" logo pattern).

There are several ways to retrieve the phase profile for the specific target image, among which Gerchberg-Saxton (GS) iterative algorithm is one of the most widely used one [95], as shown in Figure 5.4. It starts with Gaussian beam amplitude or plane wave with an arbitrary initial phase profile. Then it propagates to the far field with a Fourier transform. The amplitude of field in the far field is then replaced with the target image (here a "Cal" logo pattern is used) while the phase is kept. This complex field is then used to generate the incident wave after the phase mask plane via an inverse Fourier transform. On the phase mask plane, the calculated amplitude is then replaced with the incident beam one and propagates to the far field again. The process involving Fourier and inverse Fourier transforms with two amplitude constraints (incident beam amplitude and far field target amplitude) is repeated iteratively until a satisfied far field image is obtained. Figure 5.6 (a) and (b) shows the original image and the GS method generated far field target image, respectively. Here the original image size is 300 pixel

× 300 pixel, which leads to the same size for the hologram phase mask because of the discrete Fourier transform. The pixel size of the phase mask is optimized to bring out the maximum conversion efficiency, which is the same as beam bending and focusing effects. However, as shown in Figure 5.6(b), the GS method generated image shows some noises, which cannot be eliminated by implementing more iterations.

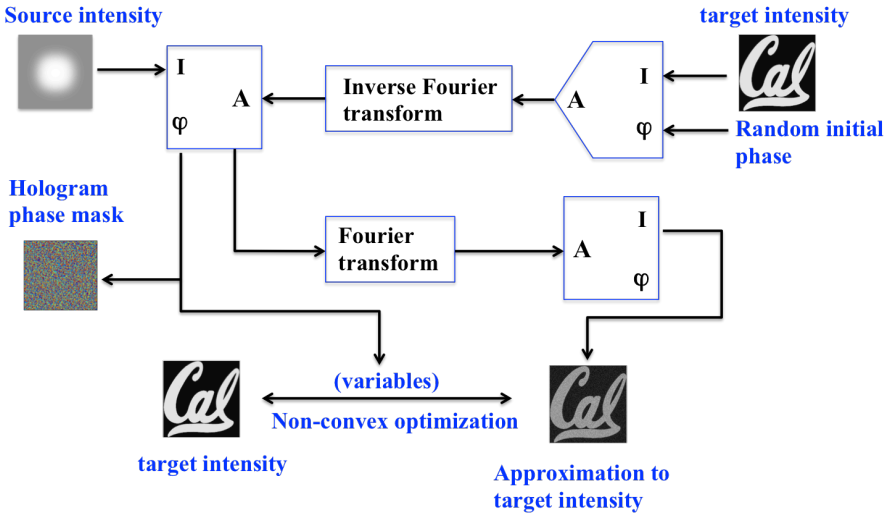

Figure 5. 5 Flow chart of the non-convex optimization algorithm to generate phase profile.

To obtain a far field target image with low noise level, a non-convex optimization algorithm is employed to generate the phase profile [96], shown in Figure 5.5. The initial phase profile is obtained with inverse Fourier transform and then Fourier transform allows for the far field pattern generated. The difference between the generated far field pattern and the ideal target image is the cost function, which is required to minimize with the phase profile variables. The generated image is shown in Figure 5.6(c), which provides improved quality over the traditional Gerchberg-Saxton method by exploiting the binary nature of the target pattern.

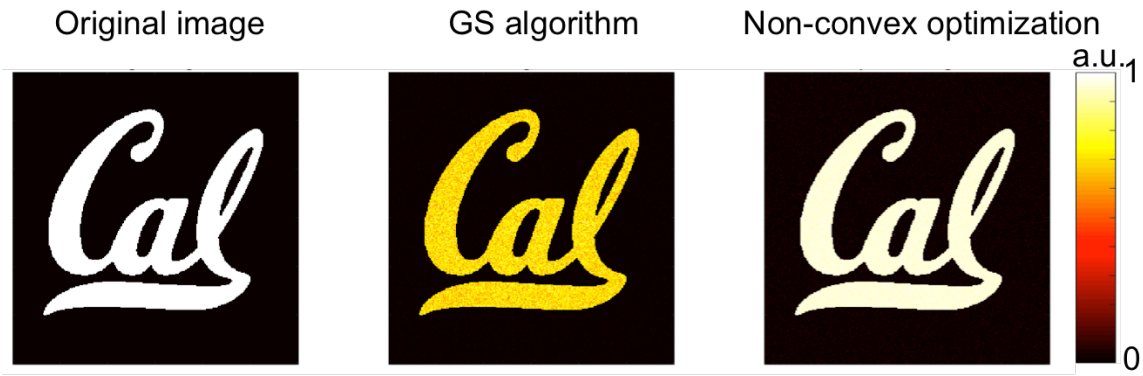

Figure 5. 6 (a) Original image (b) GS algorithm generated image with high noise level (c) Non-convex optimization algorithm generated image with low noise level.

5.3 Conclusions

In this Chapter, we demonstrate the designs of metasurfaces for versatile and unconventional optical functionalities. The phase delay imparted by the simple rotating

nanorod is discussed mathematically. Such complete phase control enables the applications of flexible beam steering, focusing and hologram generations. Two algorithms based on CGH to retrieve the phase profile are discussed and compared. The non-convex optimization, which is used in the metasurface designs (in Chapter 6), shows the ability to suppress the noise theoretically over the traditional GS method.

Chapter 6

Fabrication and characterization of all Si ultraviolet metasurfaces

6.1 Single crystal Si membrane transfer and confirmation of crystallinity

Following the design of Si UV metasurface are the fabrication and characterization. To experimentally demonstrate the effectiveness of the single-crystal Si platform in the UV range, we fabricate and characterize all-Si metasurfaces for two applications: UV beam steering and holographic lithography.

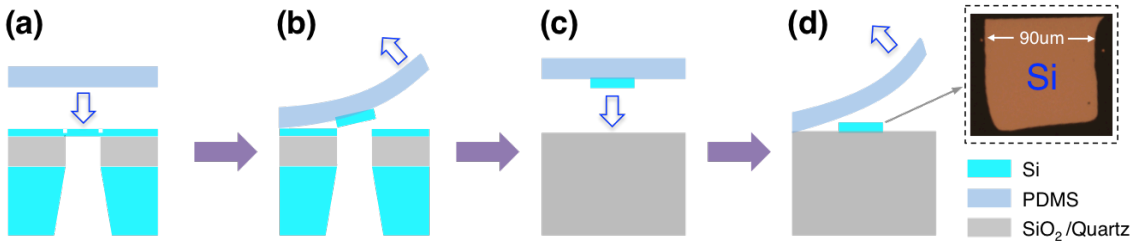

Figure 6. 1 Single-crystalline Si membranes transfer process. Inset of (d) optical image of a piece of transferred Si membrane on quartz substrate.

The fabrication process of all Si metasurfaces begins with the transfer of a single crystal Si membrane onto a quartz substrate using a PDMS stamp, as shown in Figure 6.1. This technique is inspired by the two dimensional materials transfer [97]. The Si membrane is obtained from a commercially available transmission electron microscopy (TEM) grid (SiMPore Inc, US100-C35Q33). First of all, a metallic probe is used to break the Si windows on TEM grid. A Polydimethylsiloxane (PDMS) (Sylgard 184 Silicone elastomer, Dow Corning) stamp, which is mounted on a micromanipulator, is attached to the heated TEM grid windows (suspended Si membrane) (~60 ^{o}C). As the PDMS is transparent, the Si membrane can be seen under the microscope. Once it cools down to the room temperature, the Si membrane with the PDMS is peeled off the TEM grid (Figure 6.1(a) and (b)). The Si membrane can be identified on the PDMS. Then a heated acceptor substrate (quartz) (~ 60^{o}C) is fixed on a XYZ stage. The PDMS stamp is then attached and pressed against the surface of the quartz substrate (Figure 6.1(d)). The substrate temperature is then increased to 90 ^{o}C to improve the adhesion of Si membrane to the quartz substrate. Finally it is peeled off very slowly at 90^{o}C, resulting in the Si membrane attaching well to the quartz substrate via Van de waals force

(Figure 6.1(d)). As the stamp is transparent, one can see the Si membrane through it and thereby it is possible to align the Si membrane to the desired location on both the PDMS and the acceptor substrate. The Si membrane thickness is around 40 nm. The electron diffraction pattern from the Si membrane is shown in Figure 6.2, confirming that it is indeed single crystal. Another proof of the crystalline Si is the measured refractive index spectra in the UV range, shown in Figure 6.3. As shown in Figure 6.3, ε_r goes up to ~45 around 380 nm and ε_i reaches ~42 around 300nm. The measured data (scatters) are in good agreement with the widely used ones (solid lines) [65], indicating Si membrane is single crystal.

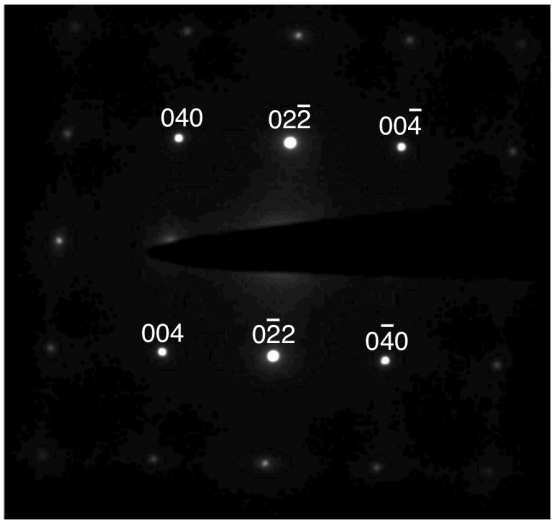

Figure 6. 2 Electron diffraction pattern of the single crystal Si membrane (zone axis [100]). Selected area diffraction pattern is taken along the Si [100] direction. Sharp diffraction spots after indexing indicate the perfect diamond cubic (dc) structure of high-quality single crystal Si.

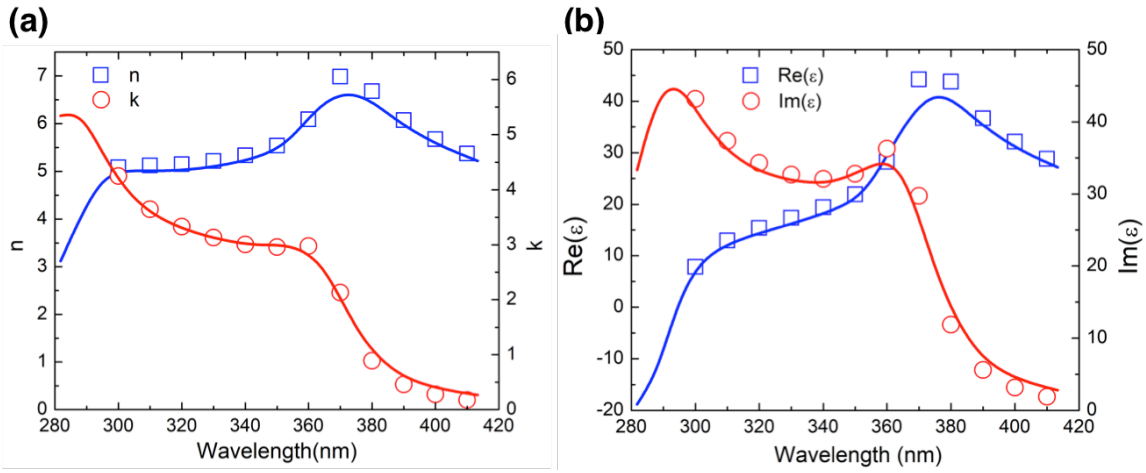

Figure 6. 3 (a) Refractive index and (b) permittivity spectra for Si in UV range. The dots are the measured date and the solid curve is reference [65].

6.2 Fabrication of metasurfaces

The phase profile for the specific target image is obtained with the non-convex optimization algorithm discussed in Chapter 5. The pitch size of 160nm, length of 145nm and width of 40nm are shown to bring out the maximum scattering efficiency, as discussed in Chapter 4. Then the mask layout based on the phase profile can be drawn and used to fabricate the Si UV metasurfaces.

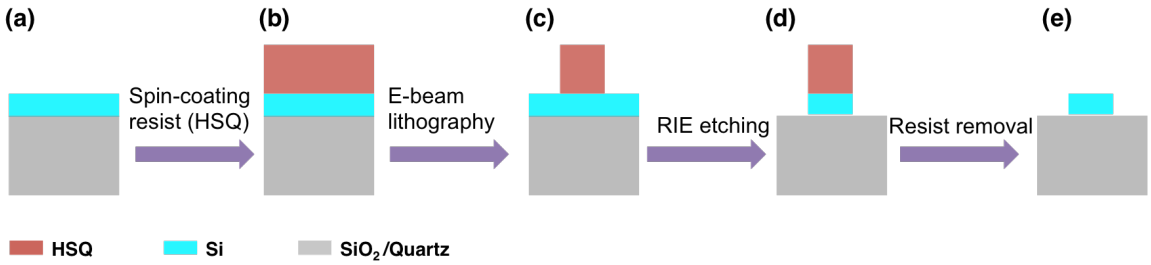

Figure 6. 4 Fabrication processes of Si metasurfaces with E-beam lithograph and RIE etching.

Electron beam (E-beam) lithography and standard reactive ion etching (HBr/Cl_2) techniques are utilized to fabricate the metasurface patterns on the Si film as shown in Figure 6.4. Electron beam resist, Hydrogen silsesquioxane (HSQ) is first spin-coated on Quartz substrate. Then electron beam is used to expose HSQ resist and a development with 25% Tetramethylammonium hydroxide (TMAH) for about a minute results in the pattern shown in Figure 6.4(c). Reactive ion etching (RIE) with HBr/Cl_2 technique is employed to etch Si membrane. Hydrogen Fluoride (HF) is used to remove the residue HSQ. In the experiment, it is not removed finally since it does not affect the performance of the metasurface. Figure 6.5 shows the scanning electron microscope (SEM) pictures of fabricated metasurfaces for beam steering (Figure 6.5(b)) and hologram applications (Figure 6.5(c)).

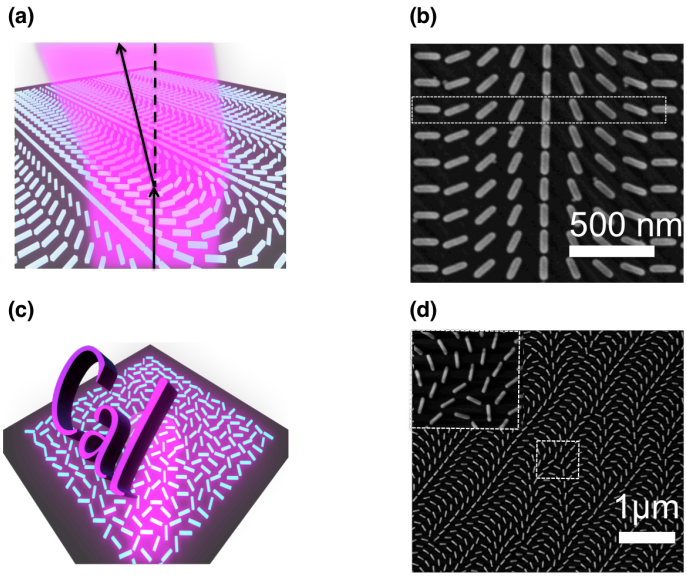

Figure 6. 5 Schematic illustrations of (a) beam steering and (c) hologram with Si metasurfaces. SEM pictures of metasurfaces for (b) beam steering and (d) hologram applications (the inset at the left upper corner is the enlarged view of the dotted box area).

6.3 Characterization of the metasurface for beam steering

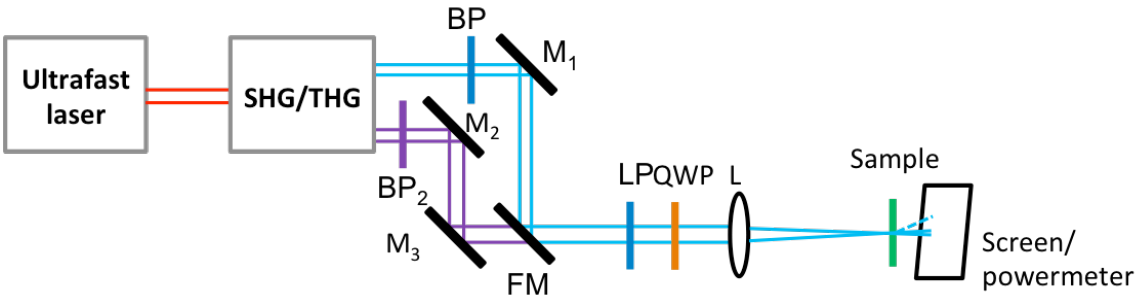

Figure 6

Figure 6. 6 Optical setup for measuring the conversion efficiency. Abbreviations used for the optical components are as follows. SHG: second harmonic generation; THG: third harmonic generation; BP_1 and BP_2: band pass filters; M_1 and M_2: mirrors; FM: flip mirror LP: linear polarizer; QWP: quarter wave plate; L: lenses. A flip is used to switch from THG to SHG wavelength range. THG: 340nm to 410nm; SHG: 290 nm to 340 nm.

In the demonstration of UV beam steering, each unit cell of the metasurface (labeled as a dashed box in inset of Figure 6.5(b)) is composed of eight optimized Si nanorods with different orientation angles lying on a quartz substrate (each nanorod is in a single unit). The optical setup for measuring the conversion efficiency spectra of the beam steering application is depicted in Figure 6.6. A femto-second laser (Coherent, Chameleon Ultra II) combined with a tripler (Coherent, Chameleon SHG/THG), which can generate coherent UV light source from 228 nm to 500nm, is used. In the measurement SHG covers the wavelength range from 340 nm to 410nm while THG provides 290 nm to 340 nm light. A polarizer (Thorlabs, GLB10) and a quarter-wave plate (Thorlabs, AQWP05M-340) are employed to generate the wavefront (circular polarization) required by the metasurface. The optical powers of the bent beam and the incident beam are captured by a powermeter (Conherent, Controller: FieldMaxII-TO Laser Power Meter; head: OP-2UV).

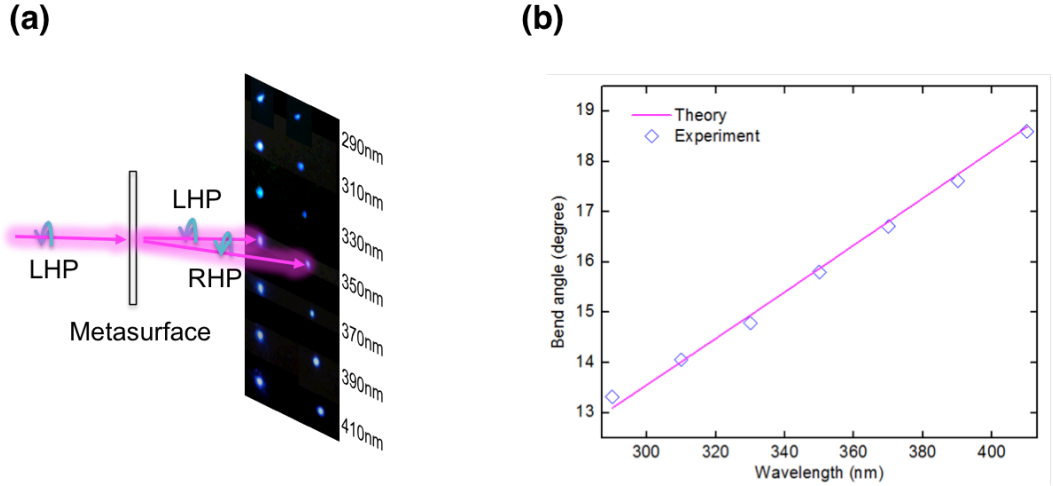

Figure 6. 7 (a) Optical image of the unconverted and bent beams on a luminescent screen for wavelengths from 290 nm to 410 nm. (b) Theoretically and experimentally obtained bending angle for different wavelengths in transmission mode.

A luminescent screen after the metasurface captures the beam spots (unconverted and converted beams), as shown in Figure 6.7(a). The distance between those two beam spots and the one between the luminescent screen and the metasurface are measured to calculate the bending angle. The unit cell covers 2π phase shift, leading to a bending angle of approximately 13.1 degrees at 290nm wavelength and 17.3 degrees at 380 nm, as shown in Figure 6.7. The measured bending angles for different wavelengths are in good agreement with the theoretical predictions with Equation 5.4.

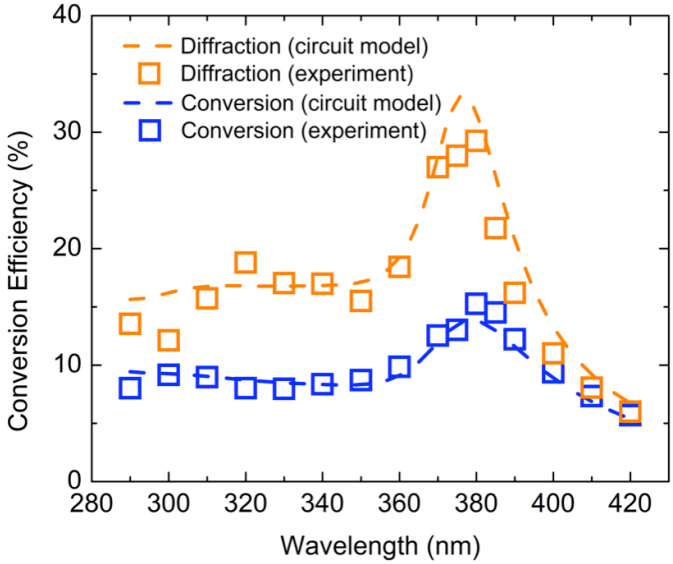

Figure 6. 8 Theoretically calculated (with circuit model) (dash line), FEM simulated (solid line) and experimentally measured (diamond scatterers) conversion efficiency of the metasurface. Fabricated nanorod dimensions: L =142 nm, W =32 nm, and H = 35 nm.

The conversion efficiency (the ratio of the power of the bent beam to the total incident power) and diffraction efficiency (the ratio of the power of the bent beam to the direct transmitted power) are measured using the experimental setup shown in Figure 6.6. As shown in Figure 6.8, over a broadband range from 290 nm to 410 nm, the conversion efficiency reaches as high as 15% at 380 nm and remains at the level of 10% even at the short wavelength of 290nm. Meanwhile, the diffraction efficiency achieves 30% around 380nm and maintains over 15% at shorter wavelengths. The experimental results plotted in Figure 6.8 are in good agreement with circuit model calculations (discussed in Chapter 4), which are plotted as dashed curves in the same Figure

Figure 6.8 shows two local maxima around 300nm and 380nm in conversion efficiency spectrum, corresponding to two dipole resonances. This can be explained by the circuit model discussed in Chapter 4. From the classical antenna theory, antenna resonance is defined as when the impedance of antenna becomes a real number. In other words, the total reactance (imaginary part of impedance) is zero. Following the circuit model we show in Figure 4.2 and the geometry of antenna therein, the total reactance in our system consists of two parts: $j\omega L_f$ and $1/j\omega C_{self}$, respectively, where j is the imaginary unit and ω is frequency. We plot $j\omega L_f$ and $-1/j\omega C_{self}$, as a function of wavelength, as shown in Figure 6.9. Near 380 nm, those two curves intersect, indicating that antenna is on resonance. It is the origin of the local peak in conversion efficiency.

Note that there is also a small bump of conversion efficiency near 300 nm (Figure 6.8). The reason is that Si has a very small real permittivity ($\varepsilon_r \sim 0$) and very large imaginary permittivity ($\varepsilon_i \sim 37$) at that wavelength range, which results in a small impedance:

$$Z_{\max} \propto \frac{1}{j\omega\varepsilon_0\left(\varepsilon_r - 1 - j\varepsilon_i\right)} \tag{6.1}$$

The total impedance of the circuit drops significantly and the scattering increases.

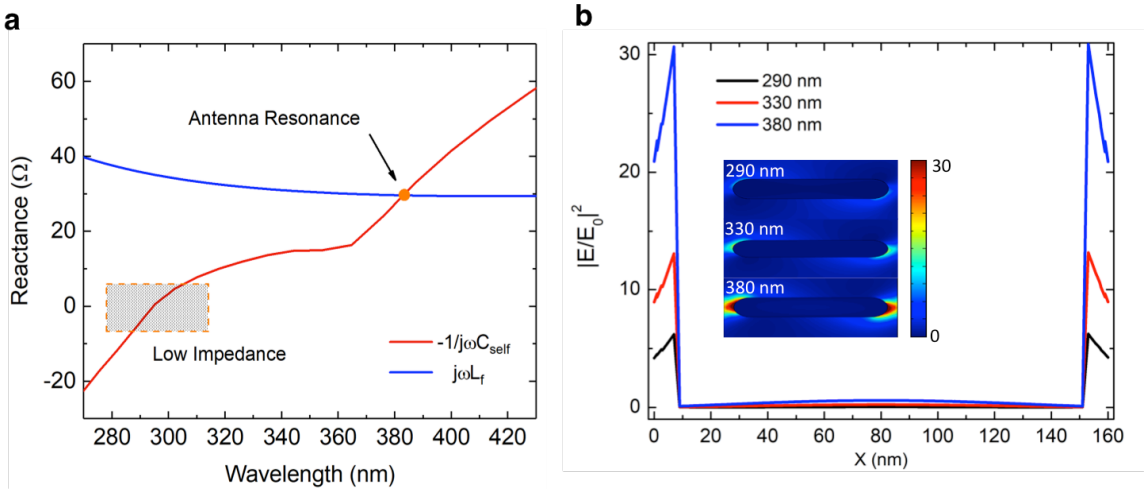

Figure 6. 9 (a) Reactance (including capacitance and inductance) spectrum for Si antenna. (b) Near field distribution of Si antenna at different wavelengths (normalized to the incident field) plotted along the long axis of the antenna. The inset shows the two-dimensional intensity distribution. The asymmetry field distribution is due to the circularly polarized incidence.

In addition to understanding the local maxima in scattering spectrum, the overall high efficiency can be explained with circuit model and the analysis of field distribution. We first look back at the field distribution, which is shown in Figure 6.9(b). It is very clear that the majority of field is repelled outside the antenna body. With very little penetration of field into the lossy dielectric, the dielectric loss is limited. This phenomenon results from the fact that large permittivity strongly enhances scattering. The permittivity of Si at 380 nm is 40 + *i*7, so that the dielectric loss is small enough to support a relative sharp peak.

We shall also obtain quantitative results using circuit model. The dielectric loss corresponds to the R_Ω in the circuit (Figure 4.2), which is also the real part of Z_{mat} (Equation 6.1),

$$R_\Omega = \mathrm{Re}\left[Z_{\max}\right] \propto \frac{\varepsilon_i}{\omega\left[\left(1-\varepsilon_r\right)^2 + \varepsilon_i^2\right]} \tag{6.2}$$

From Equation 6.2, a large ε_r will limit the dielectric loss. The resistance of the Si nanorod we investigate here is about 8 Ω at 380 nm wavelength, while an Al nanorod has resistance of 11 Ω with the same geometry. Consequently, the resonance peak we observed in the conversion efficiency is not very broadened.

6.4 UV hologram enabled high-resolution lithography

A unique advantage of UV light is that its high photon energies and short wavelengths are highly desired for photolithography applications. Even three-dimensional (3D) lithography of periodic structures has been achieved with UV illumination [98]. Here, for the first time to the best of our knowledge, we demonstrate metasurface-based holographic lithography of arbitrary patterns. The manipulation of phase for each individual antenna of a metasurface allows the implementation of computer-generated holography (CGH). Our setup is demonstrated at 380 nm, close to the widely used mercury *i*-line, allowing utilization of various widely used photoresists (e.g. S1800 series, SPR220 series, and AZ 7800 series). The first hologram we create is a "Cal" pattern. The discrete phase distribution (32 phase levels covering 2π) is generated by an iterative nonlinear optimization algorithm, as discussed in Chapter 5.

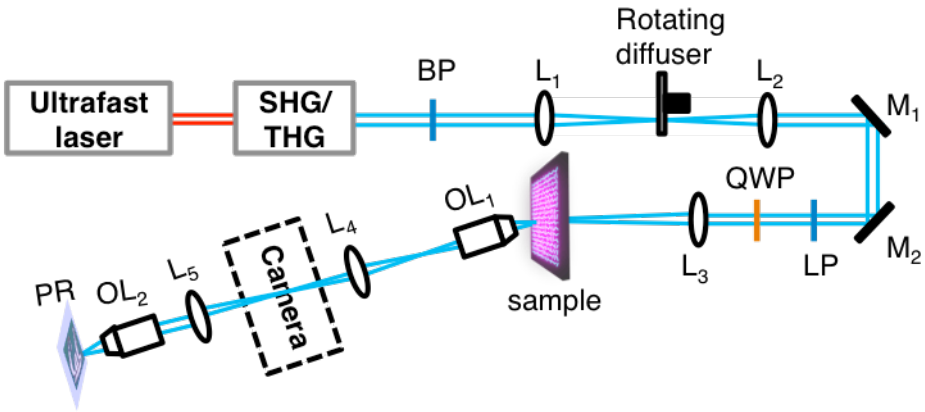

Figure 6. 10 Experimental setup for photolithography enabled by generated hologram. Abbreviations used for the optical components are as follows. BP: band pass filter; L_1, L_2, L_3, L_4, L_5: lenses; M_1, M_2: mirrors; LP: linear polarizer; QWP: quarter wave plate; OL_1, OL_2: objective lenses; PR: photoresist (S1805). The camera is removed during the exposure.

The experimental setup is depicted in Figure 6.10 to characterize the holographic lithography. An off-axis design is applied such that the image propagates in the similar way as the bent beam (Figure 6.11b shows a low resolution image compared to Figure 5.6(c) because only part of the image is used for the off-axis image), as shown in Figure 6.10. A 4f system is inserted in the illumination path and a rotating diffuser (Edmund, # 47989) in the focused beam plane to reduce the laser speckle noise (shown in Figure 6.10) by diminishing the temporal coherence and maintaining the spatial coherence. After the metasurface, a Mitutoyo long-working-distance objective lens (M Plan Apo SL100×, NA = 0.55; working distance = 13 mm; effective focal length is 2 mm) and a fused silica lens (focal length is 38 mm) are used to form an image of holographic "CAL" pattern on a CMOS camera (Thorlabs, DCC1645C). Another two-lens system consisting of a fused silica lens (focal length is 300 mm) and a Mitutoyo objective lens (M Plan Apo NIR20×, NA = 0.40; working distance = 20.0mm; effective focal length is 10 mm), is employed to shrink the size of the image by 30 times and the image is then recorded by the photoresist (S1805). Photoresist S1805 is spin-coated with a speed of 5000 rpm, forming a thickness of around 400nm and it is developed with MF-319 developer (MicroChem).

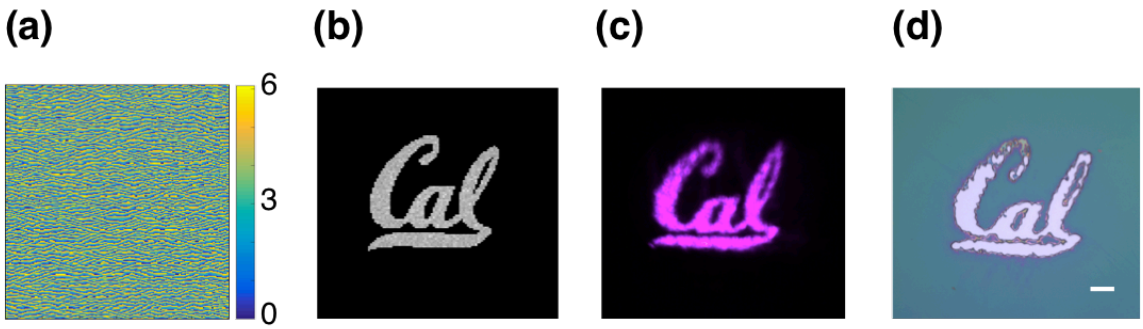

Figure 6. 11 (a) Phase distribution of target image ("Cal" logo) obtained with the non-convex optimization algorithm and (b) Theoretically calculated holographic "Cal" pattern based on the phase distribution in (a). (c) Camera captured holographic "Cal" pattern. The operating wavelength is 380 nm. (d) "Cal" pattern exposed on photoresist. Scale bar: 10 μm.

The camera captured image of "CAL" pattern is shown in Figure 6.14(c)), and then the exposed photoresist by a de-magnified pattern is shown in Figure 6.14(d). All features shown in Figure 6.14(c), including the uneven boundaries, are transferred to the resist, confirming the fidelity of the lithography process.

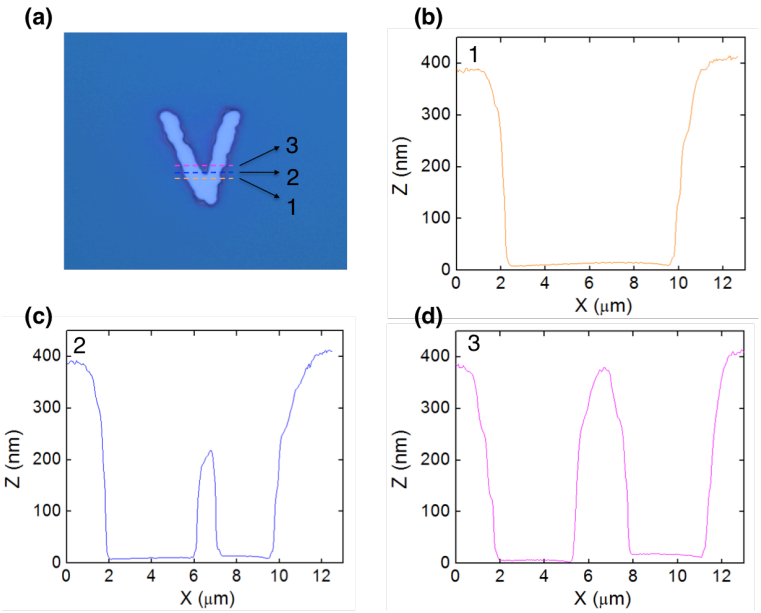

Figure 6. 12 AFM measurement for the height of the photoresist. (A) Optical image of the "V" pattern and the three lines chosen for AFM measurement for the resolution. Height information along the lines (drawn in (a)), (b) line 1, (c) line 2, (d) line 3.

To demonstrate the resolution of this holographic lithography, a "V" shape pattern with a smaller size is recorded on the resist as well, shown in Figure 6.12 (the camera captured "V" pattern is shown in the inset). Figure 6.12(b)-(d) show the Atomic Force Microscope (AFM) images of the exposed photoresist along the dashed line drawn in Figure 6.12(a), demonstrating a half-patch resolution of approximately 2 μm (similar definition of resolution in [22]). In principle, the resolution of this design is only restricted by the diffraction limit, which can be achieved by further optimizing the fabrication process and the imaging system. This metasurface-based lithography can be

potentially extended to 3D with 3D holography, a step forward from existing lithography technologies [98].

6.5 Alternative designs to improve the conversion efficiency of metasurfaces

To further boost the efficiency of UV metasurfaces, here we propose two different ways: one is to work in the reflection mode (Figure 6.13) and the other is to utilize the double-bar structures (Figure 6.14).

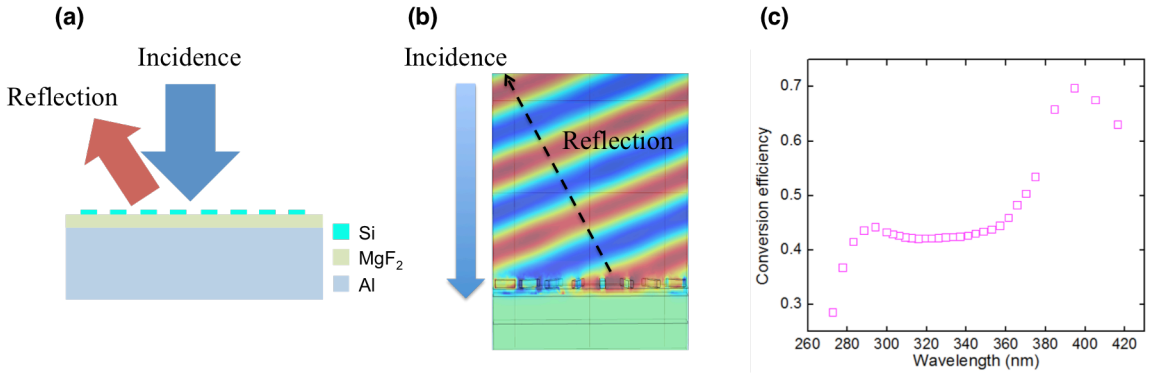

Figure 6. 13 (a) Schematic illustration of reflective metasurfaces with MgF_2 spacer layer and Al mirror. (b) FEM Simulation of the reflected field with a reflective metasurface. The antenna size is the same with the transmissive ones as discussed above. The thickness of the MgF_2 is 30nm. (c) Conversion efficiency spectrum of a reflective metasurface.

Figure 13(a) shows schematic illustration of a reflective metasurface. The same Si metasurface is designed with the previous transmissive metasurface and a Magnesium fluoride (MgF_2) spacer layer and Al mirror are employed here. The spacer layer is 30 nm thick, which is optimized for the overall range of 290nm to 420 nm. Figure 6.13(b) shows the simulated beam steering of the reflected circularly polarized field with opposite helicity achieved with 8 nanorods at 380 nm. COMSOL simulation shows that the maximum efficiency in the UV ranges increases to 70% in the reflection mode (Figure 6.13(c)) and the overall efficiency is around 45%.

With optimization of the antenna design, even higher efficiencies for both transmission and reflection modes can be achieved. For example, by introducing a double bar design (Figure 6.14(a)), the efficiency of the all-Si metasurface can be increased to the level of 200% (diffraction efficiency) and 37% (conversion efficiency) in the transmission mode (Figure 6.14(b)). This high diffraction efficiency will be essential to improve the signal-to-noise ratio in the far field transmission. The demonstration of effective UV beam steering successfully confirms the proposed mechanisms that the scattering efficiency of nano-optic antennas benefits substantially from the strong interaction between Si and UV light. With spacer later and reflective mirror, or sandwiched double bar configurations, this interaction can further be boosted and thereby improving the conversion efficiency.

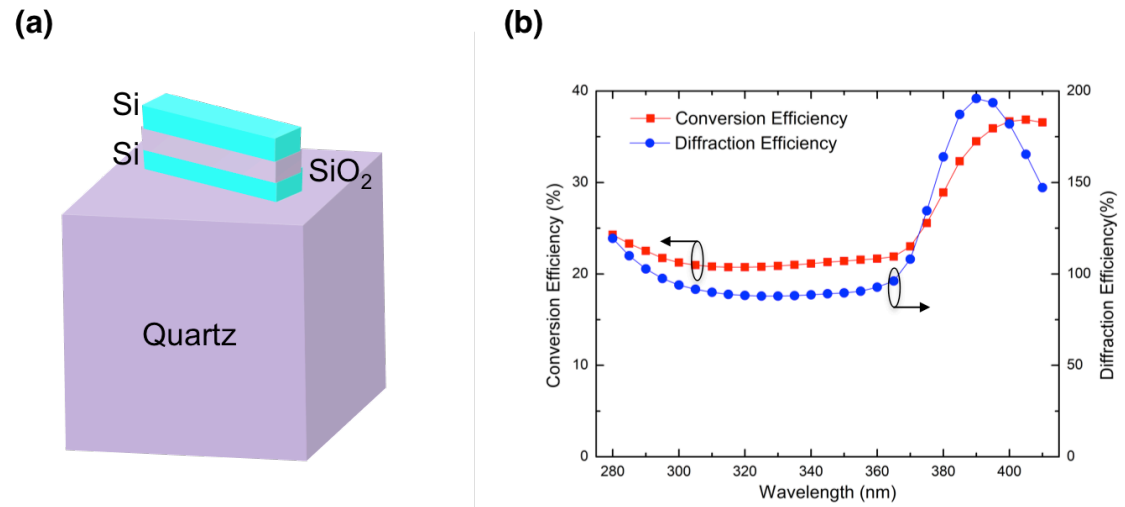

Figure 6. 14 Double-bar design and simulated conversion efficiency and diffraction efficiency spectra. a) Schematic of a unit cell of the double bar metasurface design. The period of a unit cell and the Si antenna size are the same with the single bar design. The sandwitched SiO_2 has the same length and width with Si. Its thickness is 30nm. b) Simulated conversion and diffraction efficiency spectra in the UV range. The overall conversion efficiency is increased to be higher than 20% and maximum is even higher than 35%. The diffraction efficiency is around 100% for the whole UV range and the maximum is up to 200%.

6.6 Conclusions

Utilizing the all-single crystal Si platform, we have experimentally demonstrated broadband UV metasurfaces with efficiencies as high as 15% in transmission mode for beam steering applications. The COMSOL simulations predict 70% efficiency in the reflection mode and a double bar design is able to boost the transmissive diffraction efficiency to 200% theoretically. A circuit model is built and accurately describes the total impedance modulation by the material permittivity. Enabled by the new capability in manipulating UV light, we have achieved micron-resolution holographic lithography. Our results pave the way to better understand and effectively utilize material loss instead of avoiding it. By employing other larger bandgap materials, the working spectrum range can be broadened to even far UV frequencies. Moreover, a single 2D mask can generate multiple holographic patterns at the same time, each at a different image plane, enabling cost-effective fabrication and the potential for 3D lithography, providing new opportunities for future nano-manufacturing.

Chapter 7

A lithography free and field-programmable photonic metacanvas

7.1 Introduction

Mathematical operators are generally used in wave optics to quantify the light manipulation of photonic devices, and different photonic devices correspond to specifically fixed mathematical operators [99], which indeed leads to principal and experimental limitations. On the one hand, in situ modification of the corresponding mathematical operators is necessary to fulfill the functionality of an optical reconfigurable system; on the other hand, probing into the time-resolved observation of photonic phenomena requires real-time evolution of those mathematical operators. As such, rewritability, with successful examples in other fields like field-programmable gate arrays (FPGA) [100], would create new optical functionalities via (re) compilation of photonic operators [101], and thus inevitably attracts vast attention in the field of photonics. Previous attempts realizing the reconfigurability used micro/nanomechanical metamaterials [102-104], liquid crystals [105] or amorphous-crystalline phase-transition materials [106], are limited in terms of functionality, pixel density, efficiency, fabrication/reconfiguration cost or high working temperature (>623 °C) [107]. It is much desired to utilize phase-transition materials to reconfigure photonic elements in a fast, scalable, cost-effective, and lithography-free way at or near room temperature.

In this Chapter, we present an all-solid, rewritable metacanvas for photonic applications, on which arbitrary photonic devices can be rapidly and repeatedly written and erased for real-time manipulation of light waves. Different patterns can be written and erased on the same metacanvas successively. The writing is performed with a low-power laser and the entire process stays below 90 °C. Dynamic manipulation of optical waves is demonstrated with the metacanvas, specifically light propagation, polarization, and reconstruction. The metacanvas supports physical (re)compilation of photonic operators akin to that of FPGA, thus realizing the in situ modification of the corresponding mathematical operators of the metacanvas. This dynamic optical system without moving parts opens possibilities where photonic elements can be field programmed to deliver complex, system-level functionalities.

7.2 Phase transition signature of VO_2 and deposition of polycrystalline VO_2 film

The meta-canvas is realized using the hysteresis of the metal-insulator phase transition (MIT) of polycrystalline vanadium dioxide (VO_2) films. It is of important to review the phase transition signature of VO_2 first. VO_2 undergoes a temperature-driven, reversible transition from the insulating (I) to metallic (M) phase when heated above its transition temperature (T_c ~ 68°C) [108]. The metal-to-insulator (MIT) transition behavior is accompanied by a significant change in mechanical, electrical and optical properties. Although this phase transition mechanism is till controversial, a representative understanding is discussed here.

As shown in Figure 7.1, when temperature is beyond the T_c (~68°C), VO_2 is in the rutile metallic phase; the vanadium ions occupy the body center and vertex of the tetragonal structure (Figure 7.1(b)) and each vanadium ion and six surrounding oxygen ions constituting an octahedral unit. The electrons are free to move, exhibiting high conductivity. When the phase transition happens, the crystal parameters change and the vanadium atoms deviate from the vertex angle, leading to the transition from highly symmetrical quadrilateral structure to monoclinic one with low symmetry and two varying vanadium-vanadium bonds (Figure 7.1(a)). The previous free-moving electrons of each vanadium atom turn to be bound to these vanadium-vanadium bonds, resulting in the insulator property. There are some reported explanations for such phase transition, such as the lattice distortion and electron correlations [109-111].

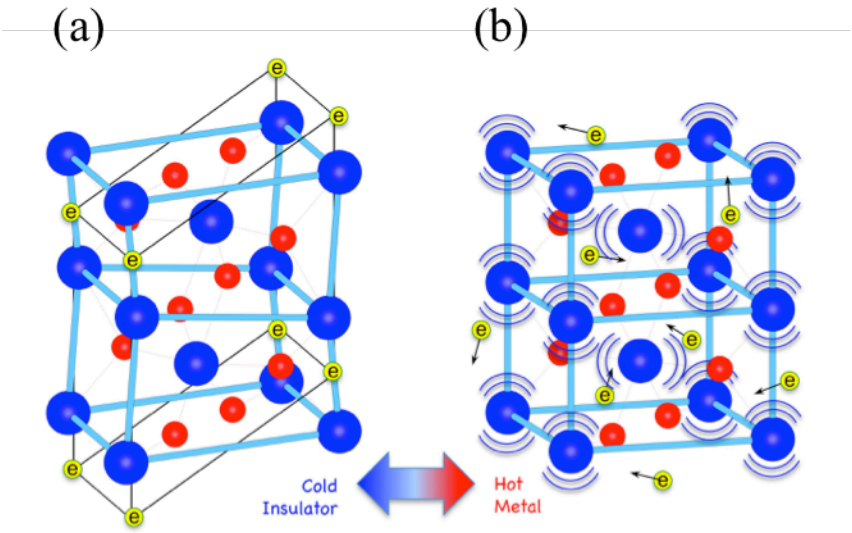

Figure 7. 1 Schematic illustration of the change of VO_2 crystal structure. (a) Monoclinic insulator (b) Tetragonal metal [108].

Such phase transition signature of VO_2 may allow for the switching between two different states. First of all we deposit and characterize VO_2 films. VO_2 films are deposited onto double-side polished, undoped Si substrates in a DC magnetron sputtering system using high-purity vanadium metal target. The sputtering was carried

out with a flowing gas mixture (49.7 sccm Ar and 0.3 sccm O_2 under 0.55 Pa for 30 min, DC power of 60 W) at room temperature. After the VO_2 deposition, it was annealed in low-pressure O_2 atmosphere (3×10^{-2} mbar) at 450 ^oC for 10 min to facilitate the crystallization. The grain size of the VO_2 thin film is roughly 50-200 nm, as shown in Figure 7.2(a). Raman spectrum of the VO_2 thin film verifies its good quality, shown in Figure 7.2(b).

The quality of VO_2 plays a pivotal role in VO_2 hysteresis (discussed later) as well as practical applications [112]. The characterization results in Figure 7.2, together with the temperature-dependent resistance curve in Figure 7.3(b), indicate the high ON/OFF ratio, steep metal-insulator transition, strong Raman signals, and correct phase transition temperature of the VO_2 films used in the experiments (more details shown in Figure 7.3). Hence, the good quality of the VO_2 films, from a practical point of view, used as the metacanvas has been verified. Also, the quality of such VO_2 films was demonstrated elsewhere [113].

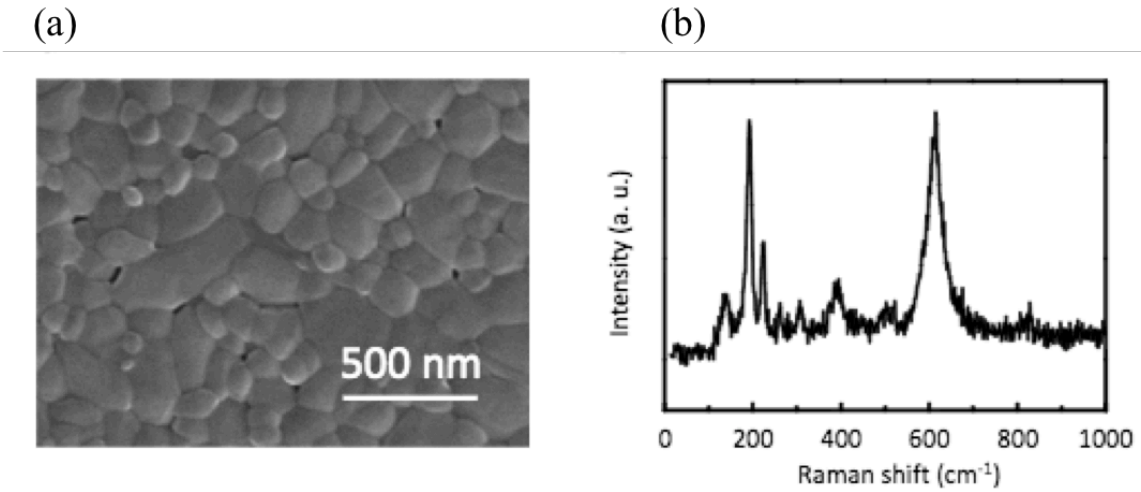

Figure 7. 2 (a) SEM image and (b) Raman spectrum of the VO_2 film.

7.3 A rewritable VO_2 meta-canvas based on hysteresis

VO_2 undergoes a temperature-driven, reversible transition from the insulating (I) to metallic (M) phase when heated above its transition temperature ($T_c \sim 68^oC$) [114]. The VO_2 film, meta-canvas, can be micro-patterned with a laser beam based on the thermal heating effect (a schematic configuration is shown in Figure 7.3(a)). These two phases differ drastically in their physical properties: the electron density (1.9×10^{23} for the M-phase Vs. 1.9×10^{19} cm^{-3} for the I-phase), color (dark green Vs. bright yellow under white light illumination, shown in Figure 7.3(b) insets), and relative dielectric constant (-35+119i Vs. 4.9 near the operation wavelength of 10.6μm in this work) are all distinct [108, 114], thus attracting much attention in various fields [115-117]. This contrast, together with the wide MIT hysteresis of poly-crystalline VO_2 films lay the material foundation that enables the meta-canvas for non-volatile pattern writing and erasing.

As illustrated in Figure 7.3(b), we first globally heat the VO_2 film from room temperature (Point A) to T_c (Point B), and the entire film is still in the I-phase. Subsequently, a laser is focused onto the film to locally heat the VO_2 to the M-phase (Point C). When the laser is turned off or moves to other regions, the laser-heated region will still stay in the M phase (Point D) owing to the hysteresis [118]. Hence a non-volatile M-phase pattern is written with the laser onto the I-phase film. The pattern can be easily erased by reducing the temperature of the entire film beyond the hysteresis (e.g., to Point A). Upon re-heating to Point B, the film is reset for re-writing the next pattern in the same region. As such, nearly arbitrary patterns of the M phase can be written, erased, and rewritten on the same area, hence providing a canvas to "field-program" various metaphotonic elements.

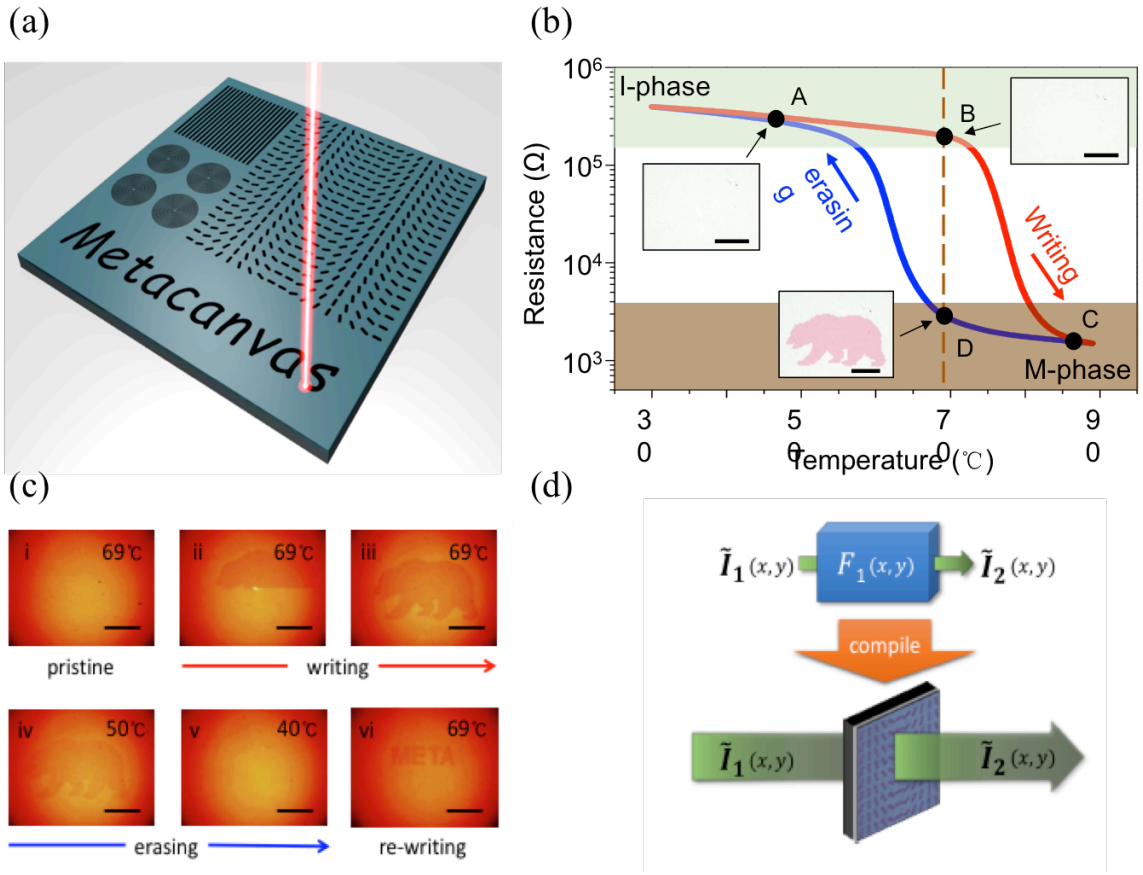

Figure 7. 3 A rewritable meta-canvas. (a) Schematic of laser writing different photonic operator patterns on a meta-canvas. (b) Temperature-dependent resistance of a VO_2 film, where the transition temperature (T_c) is denoted by a vertical dashed line. Inset A and B: un-patterned VO_2 film as a meta-canvas (all in I-phase). Inset D: the VO_2 film (global temperature kept at T_c) is laser-written with a pattern of a bear in M-phase. (c) Optical images of writing and erasing on the meta-canvas: a pattern of a bear (M-phase) is written onto an I-phase VO_2 film (i - iii), then erased by decreasing the global temperature (iv, v), and another pattern of "META" is written in the same area (vi). (d) Diagram showing the mathematic matrix ($\boldsymbol{F}$) for light waveform ($\tilde{\boldsymbol{I}}$) is compiled into a meta-canvas in the form of a photonic operator for real light manipulation. Scale bar is 100μm in b and c.

Since the meta-canvas writing is only a heating process, there is no special requirement on the writing laser. We experimentally achieved pattern writing on the meta-canvas

with various lasers, such as a 488nm continuous wave (CW) laser in a micro-photoluminescence/Raman system (Renishaw), a 400nm femtosecond laser from a Chameleon laser source (Coherent), and a 10.6μm CO_2 laser (Coherent). The temperature control (heating and cooling) was achieved using Lakeshore 325 (and/or 321) temperature controller(s) and home-made heating stages which consisted of Pt temperature sensors and Kapton® insulated flexible heaters. A LRS-0532 diode pumped solid state laser (Laserglow Technologies) was used for the laser writing, which operates in the continuous wave (CW) mode at 532 nm wavelength. Besides the laser, other key components in the direct laser writing system included an Olympus 100× lens (NA=0.95, infinity corrected), a nano-positioning stage (Aerotech, ANT130-XY series), and a mechanical shutter (Thorlabs). The movement of the nano-positioning stage and the ON/OFF of the mechanical shutter were computer-programmed and automatically controlled, where a CCD was also used for *in-situ* observation and recording. The laser power received at the VO_2 film was 1.14~1.25mW, with a diameter of less than 1 um. The resistance hysteresis curve of the VO_2 shown in Figure 7.3(b) was measured using a probe station and a home-built heating stage with a Lakeshore 325 temperature controller.

It is well worth noting that, the laser power density has to be optimized to have the best writing performance, which also depends on the thermal conductivity of the substrate, the absorption coefficient of VO_2 at the laser wavelength, and the intensity distribution of laser. Too low power results in a blur and vague pattern, while too much power causes irreversible damage to the meta-canvas. It is also applicable when the meta-canvas is used in an optical application, because if the probe laser is too powerful, it will heat the meta-canvas up and remove all patterns on it. Even though there is an upper limit for the input power, that value is really large for many applications. In our test, 10.6 μW wavelength, ~800 μm diameter CO_2 laser (which was used in the characterization) can only induce the phase transition of VO_2 in the meta-canvas at a power of ~200mW. With lower power density, it will be rather safe to conduct experiments.

Such a rewritable meta-canvas is ideal to implement compilation of photonic operators for manipulation of light. This process is similar to the concept of compilation in electrical engineering: to realize the desired logic in the form of a software program, it is compiled into FPGA using an assembly language. In such a process, the speed and programmability of the compilation are critically important. In analogy, to realize the desired photonic operator to manipulate light, it is rapidly [119] compiled onto the meta-canvas using the "assembly languages" (Figure 7.3(d)., which can be optical gratings [7, 120], metasurface [31, 106], holography [33, 121], metatronics [122], *etc.* Such rapid, cost-effective, and reversible compilation of photonic operators on the rewritable meta-canvas enables a rich collection of photonics research and applications. Here we start by dynamically compiling a phase array, based on which we develop the concept of and demonstrate a physical simulator; finally we show a more general prototype for a rewritable photonic system. The thickness of the VO_2 film is only 200 nm and the probe beam wavelength is 10.6 μm, forming a wavelength-thickness-ratio as high as 53 for all the photonic operators compiled. The writing laser used in

demonstration is a 532nm continuous laser with power around 1mW and diameter < 1μm, and a feature size of 1 μm could be achieved.

7.4 A beam-steering operator compiled on the meta-canvas

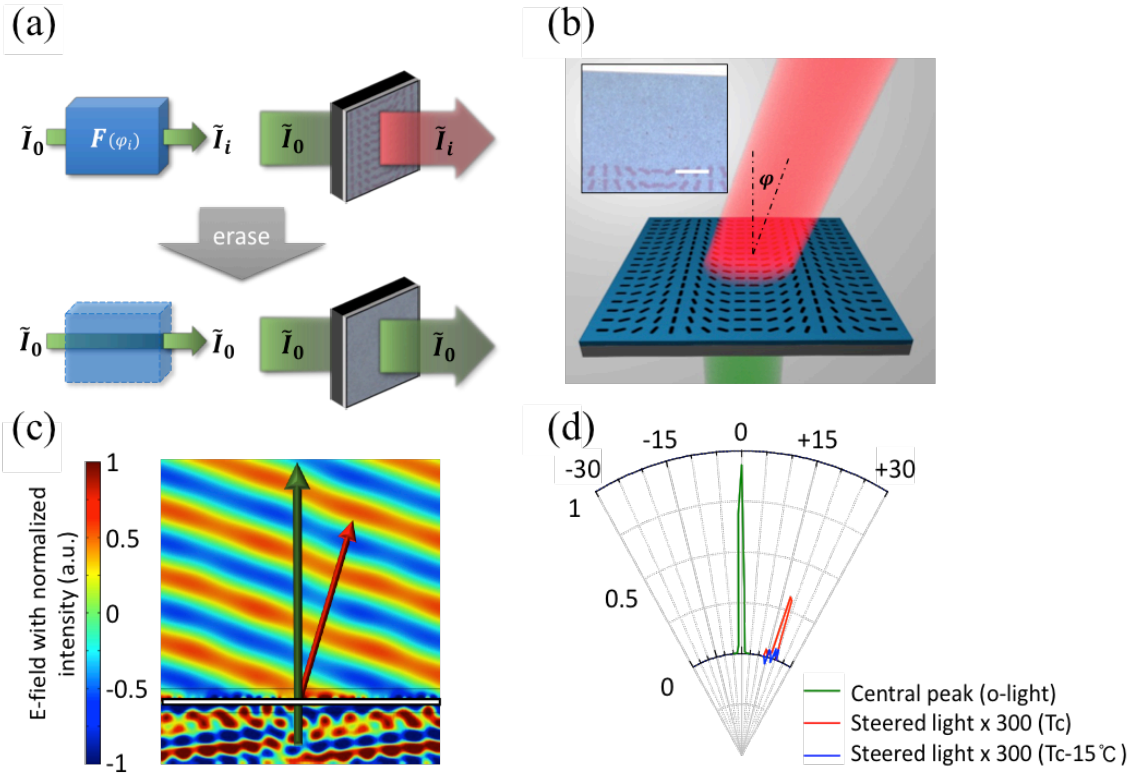

Figure 7. 4 A beam-steering operator compiled on the meta-canvas. (a) Diagram of the dynamic light beam steering process. (b) Schematic of the beam steerer with steering angle φ. Inset: optical image of a phase array compiled on the meta-canvas. Scale bar: 10μm. (c) COMSOL simulation of light steering with the phase array. The green and red arrows represent the input and the steered light propagation direction, respectively, while the white horizontal line shows the plane of the VO_2 meta-canvas. (d) Normalized measured light intensity as a function of the propagation direction angle φ.

Electromagnetic phase arrays have found various applications ranging from radar, communication [123], biomedical sciences [124], holography [33], to optical tweezers [125]. Currently, large-scale integrated phase array has been reported, but a cost-effective way to implement large-scale, lithography-free, and rapidly reconfigurable phase arrays is much desired to boost these applications. Here, we first test a basic function of the phase array, beam steering. Figures 7.3(d) show the diagrams of the beam steering process with the metacanvas. The designed phase array is compiled onto the metacanvas, which steers the input light beam to an angle of φ_i as well as changes the handedness of the steered beam, which is similar as the Si UV metasurfaces discussed in Chapters 5 and 6. In the experiment, a steered beam was indeed observed along the designed direction (Figure 7.4(d)). As we erased the phase array on the meta-canvas by decreasing the global temperature (Figure 7.4(a)), the steered beam vanished, so a new photonic operator can be compiled afterward onto the same metacanvas for

beam steering in different directions, thus verifying the (re)compilation of operators on the metacanvas.

Figure 7.4(a) shows the working sequence of the dynamic phase array. The designed phase array is compiled onto the meta-canvas to form a photonic operator $\mathbf{F}(\varphi_i)$, which steers the input light beam $\tilde{\mathbf{I}}_0$ with an angle of $\boldsymbol{\varphi}_i$ and changes the handedness of the steered beam. The definition of the operator $\mathbf{F}$, light waveform $\tilde{\mathbf{I}}$ and the detailed formulas are summarized in the Appendix. Then the operator is erased to eliminate the steering effect. The COMSOL simulation result is shown in Figure 7.4(c), which well matches the design and the experiment. In the experiment, a steered beam was observed along the designed direction (Figure 7.4(d)). As we erased the phase array on the meta-canvas by decreasing temperature, the steered beam disappeared. After that, the meta-canvas can be compiled as a new photonic operator $\mathbf{F}(\varphi_{i+1})$ for beam steering in different directions.

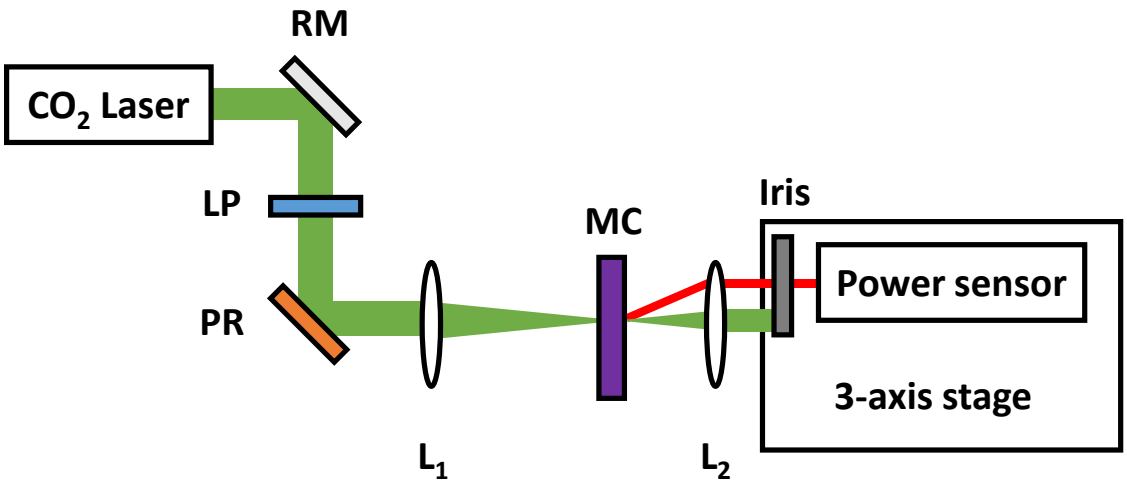

Figure 7. 5 Detailed diagram of the setup used in the beam steering and holographic physical simulator experiments. RM, reflective mirror; LP, commercial linear polarizer; PR: 90° phase retarder; L, focusing lens; MC, meta-canvas.

The experiment setup used for the beam steering is illustrated in Figure 7.5. Note that some reflective mirrors are omitted for clarity of the diagram, and the distance between optical components is not shown to the scale. A CO_2 laser (DIAMOND^{TM} C-20), with a waveform generator (33600A series, Keysight Technologies Inc.), was used for generating the desired 10.6 μm laser radiation in all the characterization experiments. A commercial wire grid linear polarizer (WP25M-IRC, Thorlabs) and a 90°phase retarder (Ophir) were used for creation of the circular polarized light. The subsequent integrated power measurement was measured using a high-sensitivity thermal power sensor (S401C, Thorlabs), where each data point is the average of 20 measurements continuously recorded at 10Hz. The mapping of intensity distribution was achieved with pixel-by-pixel scanning: one iris and the power sensor (S401C) were integrated onto a 3-axis nanomax stage (Thorlabs) controlled by a three-channel APT™ benchtop stepper motor controller (BSC203, Thorlabs). Similarly, each data point in the mapping is averaged from 10 consecutively measured values. B-spline interpolation was applied to all the mapping data.

In the beam steering experiment, the circular polarized light transmitted through the meta-canvas compiled with the phase array. A focusing lens is positioned behind the meta-canvas. Since the distance between the meta-canvas and the lens is equal to its focal length, the steered light is focused at the focal plane at the other side, where a 2D mapping was conducted. After converting the position information at the mapping plane into the steered angle, we obtained data to plot Figure 7.4(d).

7.5 Dynamic compilation of operators on the metacanvas

As a versatile platform capable of "free-style" (re)compilation of operators, the metacanvas can go beyond device level applications such as the beam steerer and enable construction of a comprehensively reconfigurable photonic system. Here, we demonstrate a prototype of such reconfigurable system using two metacanvases for time-resolved observation of dynamic transitions. Transitions between physical phenomena have been heavily investigated in attempt to reveal the otherwise hidden dynamics in various contexts, such as quantum systems [126] and topological phase transition [127]. However, in photonic systems, it is rather difficult or even impossible to experimentally achieve smooth transitions without interrupting the optics. Aided with in situ programming capabilities, a metacanvas-based system enables real-time reconfiguration of photonic operators to manipulate light, thus opening up new opportunities for resolving and probing dynamic transitions. Again as a proof of concept, we use manipulation of structured light with structured devices [128] as an example. Concentric-ring gratings have been studied intensively for exploration of cylindrical vector and orbital angular momentum with possible applications such as tight focusing and structuring of light [128]. A circularly polarized beam transmitting through the grating generates a doughnut-shaped light field with a dark center due to high transmittance of the radial component of the light beam, while a linearly polarized incident beam results in a two-lobe-shaped light field [128].

The diagram of achieving such transition is shown schematically in Figure 7.6(a). Sequentially erasing operators $\boldsymbol{F_1}$ and $\boldsymbol{F_2}$ would enable the transition from $\tilde{\boldsymbol{I}}_{\boldsymbol{3}}$ to $\tilde{\boldsymbol{I}}'_{\boldsymbol{3}}$, and finally $\tilde{\boldsymbol{I}}_{\boldsymbol{1}}$. The experimental setup is shown in Figure 4b, where two meta-canvases are used. The first meta-canvas compiled as a linear polarizer $\boldsymbol{F_1}$ transforms the circular polarized light $\tilde{\boldsymbol{I}}_{\boldsymbol{1}}$ into linear polarized light $\tilde{\boldsymbol{I}}_{\boldsymbol{2}}$, which is further transformed into a two-lobe pattern $\tilde{\boldsymbol{I}}_{\boldsymbol{3}}$ by a concentric-ring grating $\boldsymbol{F_2}$ on the second meta-canvas. Prior to the transition experiment, we characterized the performance of the linear polarizer at various temperatures, which proved that $\boldsymbol{F_1}$ was correctly compiled and erasable (Figure 7.6(c)). The polarization ratio of this linear polarizer is maximized and equal to 4.5 at T_c and gradually decreases to about 1 at T_c− 15 °C when the pattern is nearly completely erased.

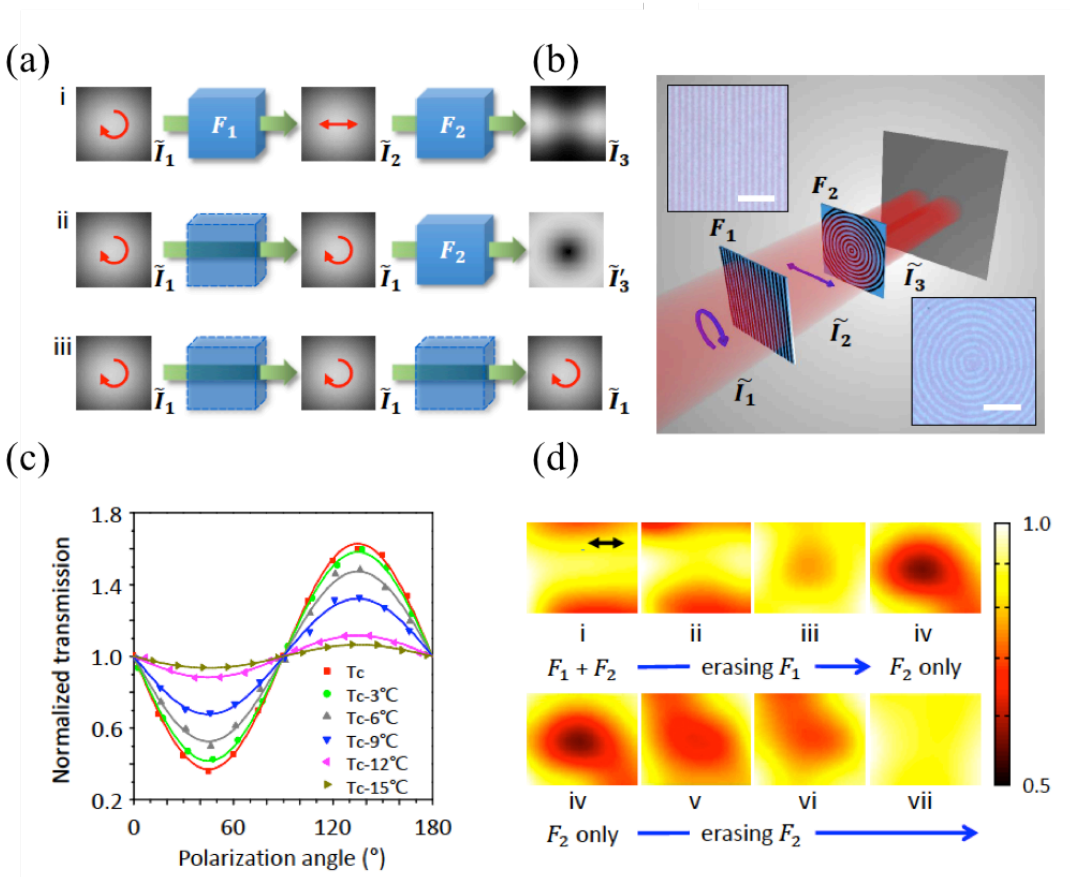

Figure 7. 6 Dynamic control of polarizers as photonic operators on the meta-canvas. a, Diagram of light manipulation with the dynamical control of the operators. b, Schematic of the experimental setup. Inset: optical images of the meta-canvas compiled as a linear polarizer $\boldsymbol{F_1}$ (top left) or a concentric-ring grating $\boldsymbol{F_2}$ (bottom right). Scale bar: 10μm. c, Evolution of the normalized polarization-dependent light transmission from the linear polarizer as temperature is decreased from T_c to T_c-15°C. d, Transmitted light intensity normalized by profile of the incident light intensity. (i) Two-lobe pattern where the arrow shows the polarization direction. (i-iv) Transition from the two-lobe-pattern ($\boldsymbol{F_1}$+$\boldsymbol{F_2}$) to a doughnut pattern (F_2 only) when the linear polarizer ($\boldsymbol{F_1}$) is erased. (iv-vii) Fading of the doughnut pattern when the concentric-ring grating (F_2) is also erased.

Note that Figure 7.6(c) in clearly shows a temperature-dependent polarization ratio of the meta-canvas compiled as a linear polarizer. This is because, when the global temperature of the meta-canvas was decreased, the written M-phase patterns on it went through a metal-insulator phase transition (MIT) and gradually faded away. After that the meta-canvas finally became a homogenous I-phase VO_2 film. Since the performance of both metallic wire grid linear polarizer and conductance is directly related to the carrier movement, we derived the polarization ratio as a function of the temperature difference from T_c, and plotted it in Figure 7.7, together with the measured hysteresis curve in Figure 7.3(b). It is clearly shown that, those data sets match each other very well, proving that the degradation of linear polarizer performance originated from the MIT of the written pattern [129].

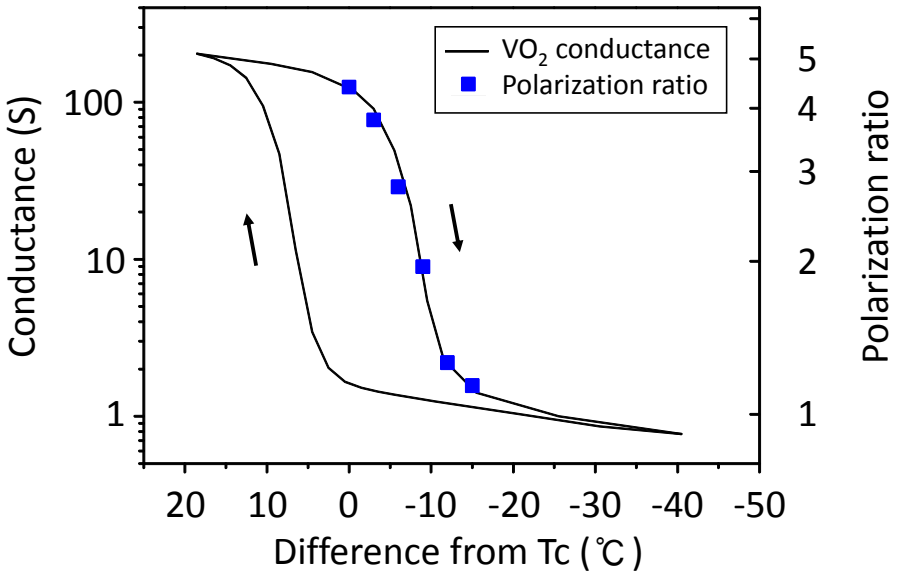

Figure 7. 7 Temperature dependent polarization ratio of the meta-operator compiled as a linear polarizer.

The concentric-ring grating was also similarly characterized and its performance was confirmed. As we assembled them as an optical system in Figure 7.6(b), a two-lobe pattern ($\tilde{\boldsymbol{I}}_{\boldsymbol{3}}$) was detected, as shown in Figure 7.6(d)-i. When $\boldsymbol{F}_1$ was being erased, we observed a smooth transition from the two-lobe pattern $\tilde{\boldsymbol{I}}_{\boldsymbol{3}}$ to a doughnut pattern $\tilde{\boldsymbol{I}}'_{\boldsymbol{3}}$ thanks to the smooth transition of the light before $\boldsymbol{F}_2$ from linear polarization to circular polarization. The reduced optical contrast of the patterns, which are practically new operators, carries the information of intermediate states. Finally, when $\boldsymbol{F}_2$ was also completely erased, the doughnut pattern vanished and the output returned the light field of $\tilde{\boldsymbol{I}}_{\boldsymbol{1}}$ since there is no operator acting on it (Figure 7.6(d)-vii). We note that what is plotted in Figure 7.6(d) is the transmission ratio in order to explicitly show the pattern. Thus, the metacanvas based optics could enable dynamical transition in optics without physically replacing the optical components. New photonic operators can be subsequently complied onto these metacanvases, hence realizing system-level reconfiguration, potentially a valuable merit for applications such as optical computing.

The experiment setup used for the separate characterization of meta-canvases compiled as a linear polarizer and a concentric-ring grating and the transition observation are illustrated in Figure 7.8. Note that some reflective mirrors are omitted for clarity, and the distance between optical components is not drawn to the scale. The light right after the phase retarder is circular polarized light.

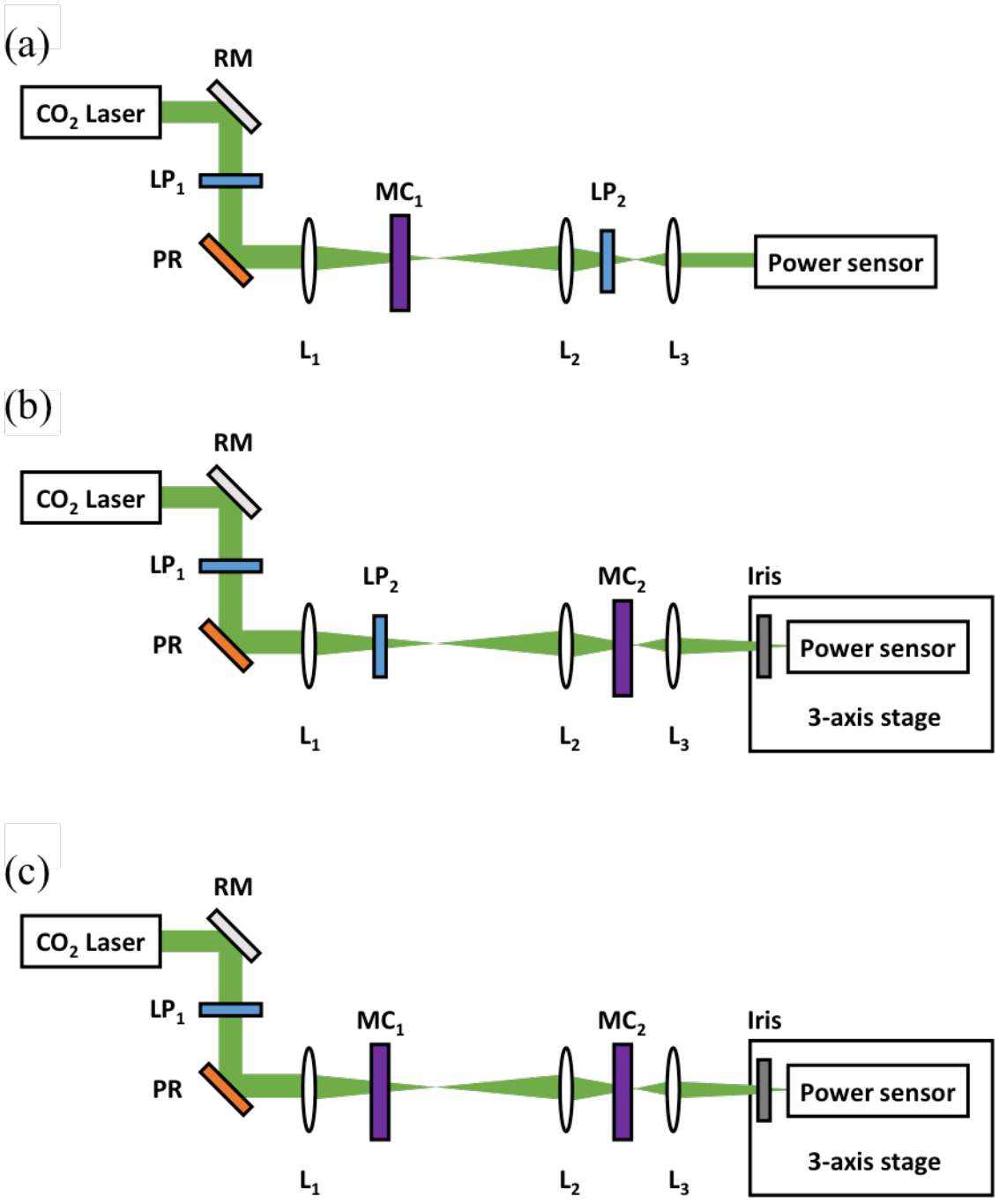

Figure 7. 8 Detailed diagram of the (a) meta-canvas as a linear polarizer, (b) meta-canvas as a concentric-ring grating, (c) transition observation setups. RM, reflective mirror; LP, commercial linear polarizer; PR, 90° phase retarder; L, focusing lens; MC, meta-canvas.

To prove the functionality of the metacanvas compiled as a concentric-ring grating. We separately characterized that with the setup shown in Figure 7.8(b). First measurement was taken using linear polarized light provided by a commercial linear polarizer (LP_2), as is in shown in Figure 7.9(a). Then we rotated LP_2 by 90°, and got the Figure 7.9(b). Those two-lobe patterns match the results in previous works [130]. Finally, we

removed the LP_2 to let circular polarized light transmit through the meta-canvas, leading to the result in Figure 7.9(c), where a doughnut shape with a dark center is shown.

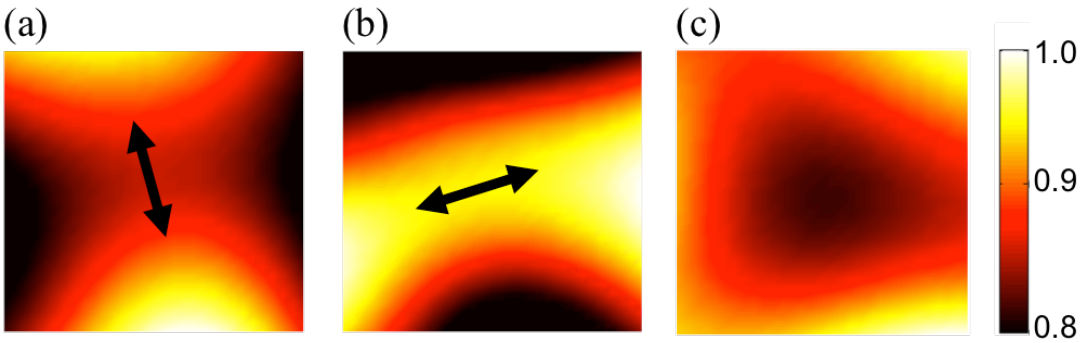

Figure 7. 9 Experimental characterization of a meta-operator compiled as a concentric-ring grating. (a) and (b)Two-lobe pattern created by making linear polarized light pass through the concentric-ring grating. Arrows show the corresponding polarization directions. (c) A doughnut pattern created by making circular polarized light pass through the concentric-ring grating.

7.6 A holographic physical simulator compiled on the meta-canvas

To further employ such photonic operator recompilation as demonstrated by the reconfigurable photonic system, we use the metacanvas to experimentally simulate the design of optical elements, thereafter termed as a physical simulator. Physical simulation is generally used in engineering projects to evaluate and compensate random errors arising from real-world applications that cannot be pre-captured by theoretical calculation or computer simulation [131] but are critical in fields such as holography. One deep-rooted problem in holography is the mismatch between the designed and experimental results caused by ubiquitous experimental errors, such as fabrication error, detector resolution, laser noise, and diffraction distortion [132]. Although numerical full-wave simulation is able to partially solve these problems, the solution is severely limited by the memory size and computation power of the simulating computer. As a result, it has not been possible to simulate large-scale holograms with billions of meshes, let alone the random influence of optical setups involved [133]. The metacanvas, with the advantages of lithography free, economical, and rapid recompilation, presents an approach to simulate the hologram with a physically real system, i.e., a physical simulator.

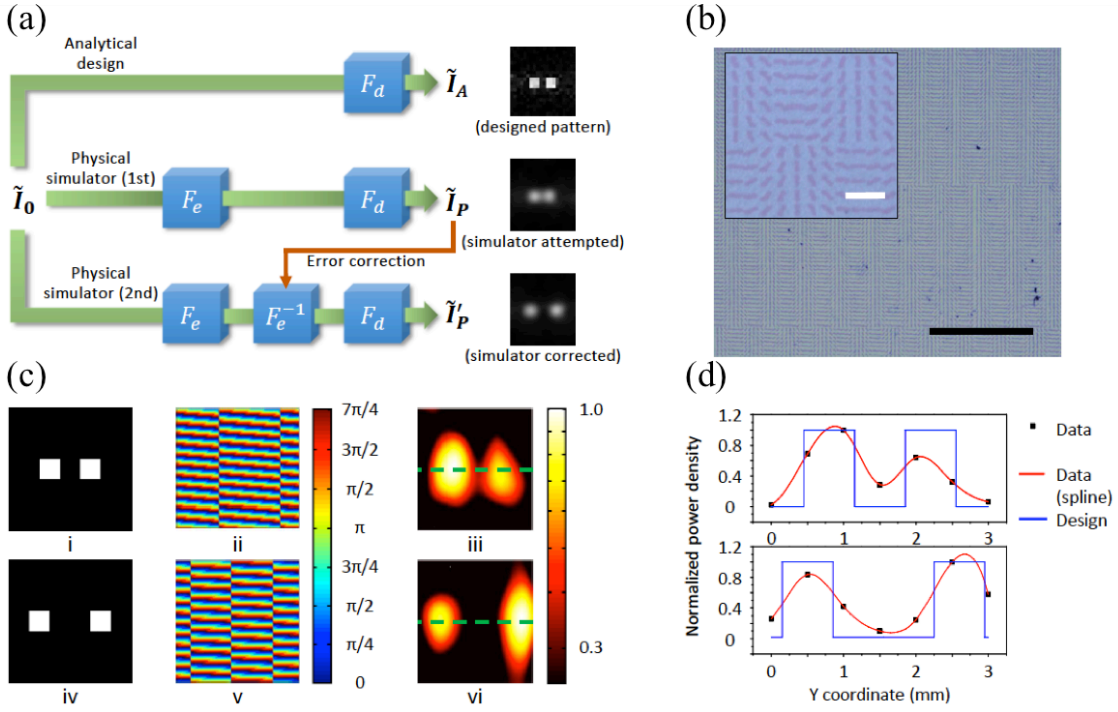

Figure 7. 10 A holographic physical simulator is compiled on the meta-canvas. (a) Diagram showing the imaging correction process using the physical simulator with schematic images. The first attempt in the physical simulator output ($\tilde{\boldsymbol{I}}_{\boldsymbol{p}}$) includes the lumped experimental error ($\boldsymbol{F_e}$) with the designed phase distribution ($\boldsymbol{F_d}$). This error information can then be identified and then input as a feedback to the second round design ($\boldsymbol{F_e^{-1}}$) in the physical simulation to eliminate the influence of error. The modified phase array ($\boldsymbol{F'_d = F_e^{-1}F_d}$) can be used in real implementation with well expected ideal image. (b) Optical images of a hologram complied on the meta-canvas with different magnifications. Scale bar: 100μm (main) and 10μm (Inset). (c) Two target two-spot images, the corresponding calculated phase distribution, and the experimental holographic images with one-pixel (i-iii) and two-pixel (iv-vi) separation. Note that (i) and (iv) only show the middle parts of the full images, and (ii) and (v) have taken into consideration the beam steering phase. (d) Comparison between the analytical design and the physical simulator output along the horizontal dashed lines in the holographic images in c(iii,vi).

The workflow of physical simulation is depicted in Figure 7.10(a), where the analytically designed hologram $\boldsymbol{F_d}$ is compiled onto a meta-canvas to output an experimental holographic image using the real setup. The difference between the designed ($\tilde{\boldsymbol{I}}_{\boldsymbol{A}}$) and the physically simulated ($\tilde{\boldsymbol{I}}_{\boldsymbol{P}}$) images is analyzed to find the lumped experimental error ($\boldsymbol{F_e}$). In the next step, a revision ($\boldsymbol{F_e^{-1}}$) is added to the design to compensate $\boldsymbol{F_e}$ for the error correction, hence achieving the error-corrected output ($\tilde{\boldsymbol{I}}'_p$). Such corrected design ($\boldsymbol{F'_d}$) can then be applied to real fabrication of holograms. To demonstrate this process, we compiled a computer generated hologram (CGH) design (discussed in Chapter 5) of a two-spot image on the meta-canvas (Figure 7.10(b)). The design of (i-ii) and the experimental observation (iii) are shown in Figure 7.10(c). The experimental result (iii) in Figure 7.10(c) shows that the two spots are separated insufficiently apart from each other, resulting in an overlap between the two spots. We then fixed the error by adding one more pixel between the spots (iv-v), which led to completely separated two spots (vi). The comparison between the design and the experimental data clearly shows the limitation of the analytical work (Figure 7.5(d)).

Therefore, using feedback between analytical design and experimental implementation, the meta-canvas based physical simulator effectively processed a real full-wave simulation breaking the computational limitation, providing a fast, cost-effective approach to correct the hologram before real-world fabrication.

7.7 Conclusions

In conclusion, we have exploited the VO_2 phase transition to attain real-time re-configurability and field programmability of photonic devices, and achieved rapid (re)compilation of various photonic operators on the metacanvas for full light manipulation in both space and time dimensions. From the high-speed, large-scale, "free-style" writing and erasing, the dynamic compilation of photonic operators has the potential to enable unprecedented applications (e.g., real-time analysis and control of photonic devices) as well as basic research (e.g., probing into time-dependent optical processes). We note that all the experiments we show in this work were completed with only three VO_2 films, which have undergone several tens of damage-free writing–erasing processes under ambient condition, exhibiting great versatility and stability. Different patterns have been repetitively written and erased on the same film, thus proving the context of rewritability.

The performance of the photonic operators compiled on the metacanvas can be further improved by optimizing the feature size and shape, the film thickness, and the material quality. Current limitations for unleashing the full potential of the metacanvas are related to our facilities rather than the metacanvas itself. Further improvements in the metacanvas can be made at least in two aspects: first, switching the laser writing to electrical control of metacanvas will potentially yield a friendlier device footprint for some integrated electronic systems; second, the technology of metacanvas can be applied to other materials with first-order phase transition and a hysteresis akin to that of VO_2 films [134], potentially expanding the spectral range and working condition. In all, aided with more advanced facilities, one can envision to further apply the metacanvas technology for more advanced applications, such as optical computing [135] or fully reconfigurable photonic circuitry [136]. It is also possible to build dynamic optical systems without moving parts, where a wide range of functionalities can be customized in situ by repeatedly programming and coding the metacanvases.

Chapter 8

Summary and outlook

In this dissertation, we explored the opportunities using dissipative dielectric meta-structures and their potential advantages over the conventionally existing optical and photonic components. In Chapter 1, we reviewed the nanophotonics field enabled by the nano-particle scattering, particularly in the form of plasmonic metals and lossless dielectric ones with high refractive index. Different mechanisms based on resonances and non-resonances are revisited, both of which show the ability to confine the field to nanoscale and manipulate the far field flexibly and hence achieving unique optical response. Some limitations with plasmonic and lossless dielectrics for specific applications, such as thermal stability, UV inactivity and low index nature were discussed. The motivation to employ dissipative dielectrics was proposed. In Chapters 2 and 3, we theoretically investigated the dissipative dielectrics in the applications for confinement and enhancement of optical field to nanoscale. Both resonant and non-resonant structures with dissipative dielectrics show the potential better performance over the lossless dielectrics. The total fluorescence enhancement over 600 can be achieved with a-Si theoretically. In Chapter 4, a circuit model was built to explain the large scattering efficiency of a dissipative antenna, providing insight into the physics behind. In Chapter 5, geometric phased enabled metasurface design was introduced. A simple rotating nanorod is able to impart different phase delay for the incident light. The beam steering, focusing and phase-only hologram applications based on the metasurfaces were discussed well. In Chapter 6, we experimentally demonstrated the beam steering and holographic lithography with the all Si metasurfaces in the UV range for the first time, to our best knowledge. Micro-resolution in lithography was achieved. Two alternative ways to further improve the efficiency were proposed as well. In Chapter 7, we demonstrated rapid compilation of photonic operators onto a rewritable meta-canvas for light manipulation. Dynamical control of optical waves for light propagation, reconstruction and polarization with VO_2 films at neat room temperature were achieved.

Looking forward, the works presented in this dissertation only represents a small portion of the potential applications of dissipative dielectrics and rewritable VO_2 can demonstrate. As we see in Chapters 2 and 3, the dissipative dielectrics may have an opportunity for enhanced Raman spectroscopy for some unique wavelengths which conventional metals and lossless dielectrics cannot reach. The two alternative ways of improving efficiency for metasurfaces are also worth to be explored experimentally and 3D lithography enabled by such high efficiency UV metasurfaces have a great potential for the replacement of projection lenses in steppers. As we discussed in Chapter 7, with the improved resolution of writing laser, a pure VO_2 metasurfaces with smaller features can be achieved and may allow for the applications in the visible wavelengths, opening up more opportunities in imaging, display and holograms. Si Metasurfaces are very promising in that they have shown the ability to allow for arbitrary manipulation for

amplitude, phase and polarization of the light with high efficiency, but their functionalities are usually fixed at the moment of fabrication. A potential hybrid system combining Si metasurfaces and VO_2 may enable potential tunability in the UV regime. Furthermore, as mentioned in Chapter 8, faster methods to induce the phase transition, for example, electrical modulation are worthy to be explored as well.

Appendix

Equivalent mathematic formulas for experiments

In the main text, mathematic operators are compiled onto meta-canvases while mathematic diagrams are used to guide the experiments. Here, the mathematic operators and diagrams are analysed in detail to give a complete explanation of the experiments in the main text.

A.1 Basic definition

Without loss of generality, the light is represented as a two dimensional (2D) complex vector $\tilde{\boldsymbol{I}}(x, y)$

$$\tilde{\boldsymbol{I}}(x,y) = \begin{pmatrix} a_x\, e^{j\theta_x} \\ \\ a_y\, e^{j\theta_y} \end{pmatrix} \tag{A1}$$

Where a_x and a_y denote the amplitudes of light in the x and y direction, while θ_x and θ_y represent the corresponding phases.

A.2 Beam steering

A nanorod optical antenna with a rotation angle of ϑ, yields a phase shift of $\psi = 2\vartheta$. It is assumed that the light is rotated along the y axis, then the phase shift should follow (A2)

$$\psi(x,y) = \frac{2\pi \sin\varphi}{\lambda} x \tag{A2}$$

Thus, ϑ of each nanorod is as follows,

$$\vartheta(x,y) = \psi(x,y)/2 = \frac{\pi \sin\varphi}{\lambda} x \tag{A3}$$

So rotation around the y axis by φ can be denoted as

$$\mathbf{F}(x,y) = r_1\, Exp\left(j\, \frac{\pi \sin\varphi}{\lambda} x\right) + r_2 \tag{A4}$$

which illustrates the way in which $\boldsymbol{F}(\varphi_i)$ in Fig. 2a is calculated.

Since the incident light is partially preserved after the meta-canvas, here we use two coefficients r_1 and r_2. r_1 denotes the amplitude of the phase-controlled light, and r_2 corresponds to the transmitted incident light, both of which are determined by the meta-canvas.

A.3 Hologram

A hologram achieves image reconstruction by designing the phase retardation at every point. We can get a 2D phase distribution $\vartheta_h(x, y)$ with computer-generated hologram design, whose effect on the probe light is expressed as

$$\mathbf{F_d}(x,y) = Exp[j\,\vartheta_h(x,y)] \tag{A5}$$

We can reconstruct the far-field holographic image by performing Fourier transform **W** with a focusing lens

$$\tilde{\mathbf{I}}_{\mathrm{A}}(x,y) = \mathbf{W}\mathbf{F}_{\mathrm{d}}(x,y)\tilde{\mathbf{I}}_0(x,y) \tag{A6}$$

A.4 Linear polarizer

A left-hand or right-hand circular polarized light (LHC or RHC) can be expressed as

$$\tilde{\boldsymbol{I}}_{LHC}(x,y) = a(x,y)e^{j\theta}(\hat{\boldsymbol{e}}_{\boldsymbol{x}} + j\hat{\boldsymbol{e}}_{\boldsymbol{y}}) = a(x,y)e^{j\theta}\begin{pmatrix}1\\ j\end{pmatrix} \tag{A7}$$

$$\tilde{\boldsymbol{I}}_{RHC}(x,y) = a(x,y)e^{j\theta}(\hat{\boldsymbol{e}}_{\boldsymbol{x}} - j\hat{\boldsymbol{e}}_{\boldsymbol{y}}) = a(x,y)e^{j\theta}\begin{pmatrix}1\\ -j\end{pmatrix} \tag{A8}$$

For a linear polarizer, the transmission coefficient of $\hat{\boldsymbol{e}}_{\boldsymbol{x}}$ and $\hat{\boldsymbol{e}}_{\boldsymbol{y}}$ polarization have different values. And a linear polarizer has the following expression of matrix

$$\boldsymbol{F}_1 = \begin{pmatrix}t_x & 0\\ 0 & t_y\end{pmatrix} \tag{A9}$$

For example, a perfect polarizer letting X-polarized light transmitted satisfies the following relationship

$$t_x = 1, \text{ and } t_y = 0 \tag{A10}$$

Bibliography

[1] B. Lee, I.-M. Lee, S. Kim, D.-H. Oh, L. Hesselink, Review on subwavelength confinement of light with plasmonics, Journal of Modern Optics, 57 (2010) 1479-1497.

[2] L. Novotny, B. Hecht, Principles of nano-optics, Cambridge university press, 2012.

[3] P. Zijlstra, J.W. Chon, M. Gu, Five-dimensional optical recording mediated by surface plasmons in gold nanorods, Nature, 459 (2009) 410-413.

[4] J.N. Anker, W.P. Hall, O. Lyandres, N.C. Shah, J. Zhao, R.P. Van Duyne, Biosensing with plasmonic nanosensors, in: Nanoscience and Technology: A Collection of Reviews from Nature Journals, World Scientific, 2010, pp. 308-319.

[5] L. Pan, Y. Park, Y. Xiong, E. Ulin-Avila, Y. Wang, L. Zeng, S. Xiong, J. Rho, C. Sun, D.B. Bogy, Maskless plasmonic lithography at 22 nm resolution, Scientific reports, 1 (2011) 175.

[6] T. Xu, Y.-K. Wu, X. Luo, L.J. Guo, Plasmonic nanoresonators for high-resolution colour filtering and spectral imaging, Nature communications, 1 (2010) 59.

[7] J.A. Schuller, E.S. Barnard, W. Cai, Y.C. Jun, J.S. White, M.L. Brongersma, Plasmonics for extreme light concentration and manipulation, Nature materials, 9 (2010) 193.

[8] A. Kinkhabwala, Z. Yu, S. Fan, Y. Avlasevich, K. Müllen, W. Moerner, Large single-molecule fluorescence enhancements produced by a bowtie nanoantenna, Nature Photonics, 3 (2009) 654.

[9] H. Guo, T.P. Meyrath, T. Zentgraf, N. Liu, L. Fu, H. Schweizer, H. Giessen, Optical resonances of bowtie slot antennas and their geometry and material dependence, Optics express, 16 (2008) 7756-7766.

[10] V.R. Almeida, Q. Xu, C.A. Barrios, M. Lipson, Guiding and confining light in void nanostructure, Optics letters, 29 (2004) 1209-1211.

[11] A.I. Kuznetsov, A.E. Miroshnichenko, M.L. Brongersma, Y.S. Kivshar, B. Luk'yanchuk, Optically resonant dielectric nanostructures, Science, 354 (2016) aag2472.

[12] K. Yu, A. Lakhani, M.C. Wu, Subwavelength metal-optic semiconductor nanopatch lasers, Optics express, 18 (2010) 8790-8799.

[13] A. Degiron, H. Lezec, N. Yamamoto, T. Ebbesen, Optical transmission properties of a single subwavelength aperture in a real metal, Optics Communications, 239 (2004) 61-66.

[14] Q.-H. Park, Optical antennas and plasmonics, Contemporary physics, 50 (2009) 407-423.

[15] M. Pelton, J. Aizpurua, G. Bryant, Metal‐nanoparticle plasmonics, Laser & Photonics Reviews, 2 (2008) 136-159.

[16] M. Caldarola, P. Albella, E. Cortés, M. Rahmani, T. Roschuk, G. Grinblat, R.F. Oulton, A.V. Bragas, S.A. Maier, Non-plasmonic nanoantennas for surface enhanced spectroscopies with ultra-low heat conversion, Nature Communications, 6 (2015) 7915.

[17] C.F. Bohren, D.R. Huffman, Absorption and scattering of light by small particles, John Wiley & Sons, 2008.

[18] J.B. Pendry, A.J. Holden, D.J. Robbins, W. Stewart, Magnetism from conductors and enhanced nonlinear phenomena, IEEE transactions on microwave theory and techniques, 47 (1999) 2075-2084.

[19] Y. Yan, G. Xie, M.P. Lavery, H. Huang, N. Ahmed, C. Bao, Y. Ren, Y. Cao, L. Li, Z. Zhao, High-capacity millimetre-wave communications with orbital angular momentum multiplexing, Nature communications, 5 (2014) 4876.

[20] K.V. Sreekanth, Y. Alapan, M. ElKabbash, E. Ilker, M. Hinczewski, U.A. Gurkan, A. De Luca, G. Strangi, Extreme sensitivity biosensing platform based on hyperbolic metamaterials, Nature materials, 15 (2016) 621.

[21] N. Fang, H. Lee, C. Sun, X. Zhang, Sub–diffraction-limited optical imaging with a silver superlens, Science, 308 (2005) 534-537.

[22] G. Lifante, Integrated photonics: fundamentals, Wiley Online Library, 2003.

[23] N. Yu, F. Capasso, Flat optics with designer metasurfaces, Nature materials, 13 (2014) 139.

[24] A.V. Kildishev, A. Boltasseva, V.M. Shalaev, Planar photonics with metasurfaces, Science, 339 (2013) 1232009.

[25] N.M. Estakhri, A. Alù, Recent progress in gradient metasurfaces, JOSA B, 33 (2016) A21-A30.

[26] S. Jahani, Z. Jacob, All-dielectric metamaterials, Nature nanotechnology, 11 (2016) 23.

[27] P. Lalanne, P. Chavel, Metalenses at visible wavelengths: past, present, perspectives, Laser & Photonics Reviews, 11 (2017) 1600295.

[28] P. Genevet, F. Capasso, F. Aieta, M. Khorasaninejad, R. Devlin, Recent advances in planar optics: from plasmonic to dielectric metasurfaces, Optica, 4 (2017) 139-152.

[29] H.H. Hsiao, C.H. Chu, D.P. Tsai, Fundamentals and applications of metasurfaces, Small Methods, 1 (2017) 1600064.

[30] P. Qiao, W. Yang, C.J. Chang-Hasnain, Recent advances in high-contrast metastructures, metasurfaces, and photonic crystals, Advances in Optics and Photonics, 10 (2018) 180-245.

[31] N. Yu, P. Genevet, M.A. Kats, F. Aieta, J.-P. Tetienne, F. Capasso, Z. Gaburro, Light propagation with phase discontinuities: generalized laws of reflection and refraction, science, 334 (2011) 333-337.

[32] X. Ni, N.K. Emani, A.V. Kildishev, A. Boltasseva, V.M. Shalaev, Broadband light bending with plasmonic nanoantennas, Science, 335 (2012) 427-427.

[33] G. Zheng, H. Mühlenbernd, M. Kenney, G. Li, T. Zentgraf, S. Zhang, Metasurface holograms reaching 80% efficiency, Nature nanotechnology, 10 (2015) 308.

[34] C. Pfeiffer, N.K. Emani, A.M. Shaltout, A. Boltasseva, V.M. Shalaev, A. Grbic, Efficient light bending with isotropic metamaterial Huygens' surfaces, Nano letters, 14 (2014) 2491-2497.

[35] A. Arbabi, Y. Horie, M. Bagheri, A. Faraon, Dielectric metasurfaces for complete control of phase and polarization with subwavelength spatial resolution and high transmission, Nat Nanotechnol, 10 (2015) 937-943.

[36] D. Lin, P. Fan, E. Hasman, M.L. Brongersma, Dielectric gradient metasurface optical elements, Science, 345 (2014) 298-302.

[37] M. Khorasaninejad, W.T. Chen, R.C. Devlin, J. Oh, A.Y. Zhu, F. Capasso, Metalenses at visible wavelengths: Diffraction-limited focusing and subwavelength resolution imaging, Science, 352 (2016) 1190-1194.

[38] S. Pancharatnam, Generalized theory of interference and its applications, in: Proceedings of the Indian Academy of Sciences-Section A, Springer, 1956, pp. 398-417.

[39] M.V. Berry, The adiabatic phase and Pancharatnam's phase for polarized light, Journal of Modern Optics, 34 (1987) 1401-1407.

[40] E. Hasman, V. Kleiner, G. Biener, A. Niv, Polarization dependent focusing lens by use of quantized Pancharatnam–Berry phase diffractive optics, Applied physics letters, 82 (2003) 328-330.

[41] Z. Bomzon, G. Biener, V. Kleiner, E. Hasman, Space-variant Pancharatnam-Berry phase optical elements with computer-generated subwavelength gratings, Opt Lett, 27 (2002) 1141-1143.

[42] Y.F. Yu, A.Y. Zhu, R. Paniagua‐Domínguez, Y.H. Fu, B. Luk'yanchuk, A.I. Kuznetsov, High‐transmission dielectric metasurface with 2π phase control at visible wavelengths, Laser & Photonics Reviews, 9 (2015) 412-418.

[43] I. Staude, A.E. Miroshnichenko, M. Decker, N.T. Fofang, S. Liu, E. Gonzales, J. Dominguez, T.S. Luk, D.N. Neshev, I. Brener, Tailoring directional scattering through magnetic and electric resonances in subwavelength silicon nanodisks, ACS nano, 7 (2013) 7824-7832.

[44] M. Decker, I. Staude, M. Falkner, J. Dominguez, D.N. Neshev, I. Brener, T. Pertsch, Y.S. Kivshar, High‐efficiency dielectric Huygens' surfaces, Advanced Optical Materials, 3 (2015) 813-820.

[45] Y. Yang, W. Wang, P. Moitra, I.I. Kravchenko, D.P. Briggs, J. Valentine, Dielectric meta-reflectarray for broadband linear polarization conversion and optical vortex generation, Nano letters, 14 (2014) 1394-1399.

[46] K.E. Chong, I. Staude, A. James, J. Dominguez, S. Liu, S. Campione, G.S. Subramania, T.S. Luk, M. Decker, D.N. Neshev, Polarization-independent silicon metadevices for efficient optical wavefront control, Nano letters, 15 (2015) 5369-5374.

[47] M.I. Shalaev, J. Sun, A. Tsukernik, A. Pandey, K. Nikolskiy, N.M. Litchinitser, High-efficiency all-dielectric metasurfaces for ultracompact beam manipulation in transmission mode, Nano letters, 15 (2015) 6261-6266.

[48] C. Pfeiffer, A. Grbic, Metamaterial Huygens' surfaces: tailoring wave fronts with reflectionless sheets, Physical review letters, 110 (2013) 197401.

[49] M.F. Limonov, M.V. Rybin, A.N. Poddubny, Y.S. Kivshar, Fano resonances in photonics, Nature Photonics, 11 (2017) 543.

[50] X. Wang, D. Wilson, R. Muller, P. Maker, D. Psaltis, Liquid-crystal blazed-grating beam deflector, Appl Opt, 39 (2000) 6545-6555.

[51] S. Wang, P.C. Wu, V.-C. Su, Y.-C. Lai, M.-K. Chen, H.Y. Kuo, B.H. Chen, Y.H. Chen, T.-T. Huang, J.-H. Wang, R.-M. Lin, C.-H. Kuan, T. Li, Z. Wang, S. Zhu, D.P. Tsai, A broadband achromatic metalens in the visible, Nature Nanotechnology, 13 (2018) 227-232.

[52] A. Zhan, S. Colburn, R. Trivedi, T.K. Fryett, C.M. Dodson, A. Majumdar, Low-Contrast Dielectric Metasurface Optics, ACS Photonics, 3 (2016) 209-214.

[53] M.W. Knight, N.S. King, L. Liu, H.O. Everitt, P. Nordlander, N.J. Halas, Aluminum for plasmonics, ACS Nano, 8 (2014) 834-840.

[54] J. Martin, J. Plain, Fabrication of aluminium nanostructures for plasmonics, Journal of Physics D: Applied Physics, 48 (2014) 184002.

[55] A. Boltasseva, H.A. Atwater, Materials science. Low-loss plasmonic metamaterials, Science, 331 (2011) 290-291.

[56] J.R. Bolton, Ultraviolet applications handbook, Ayr, Ont.: Bolton Photosciences Incorporated, 2001.

[57] P.R. West, S. Ishii, G.V. Naik, N.K. Emani, V.M. Shalaev, A. Boltasseva, Searching for better plasmonic materials, Laser & Photonics Reviews, 4 (2010) 795-808.

[58] A.D. Rakić, A.B. Djurišić, J.M. Elazar, M.L. Majewski, Optical properties of metallic films for vertical-cavity optoelectronic devices, Appl. Opt., 37 (1998) 5271-5283.

[59] P. Drude, Zur Elektronentheorie der Metalle, Annalen der Physik, 306 (1900) 566-613.

[60] P. Drude, Zur Elektronentheorie der Metalle; II. Teil. Galvanomagnetische und thermomagnetische Effecte, Annalen der Physik, 308 (1900) 369-402.

[61] E.B. Wilson, Review: H. A. Lorentz, The Theory of Electrons and its Applications to the Phenomena of Light and Radiant Heat, Bull. Amer. Math. Soc., 24 (1917) 100-101.

[62] R. de L. Kronig, On the Theory of Dispersion of X-Rays, J. Opt. Soc. Am., 12 (1926) 547-557.

[63] H.A. Kramers, La diffusion de la lumiere par les atomes, Atti Cong. Intern. Fisica (Transactions of Volta Centenary Congress) Como, 2 (1927) 545-557.

[64] J.S. Toll, Causality and the Dispersion Relation: Logical Foundations, Physical Review, 104 (1956) 1760-1770.

[65] D.E. Aspnes, A.A. Studna, Dielectric functions and optical parameters of Si, Ge, GaP, GaAs, GaSb, InP, InAs, and InSb from 1.5 to 6.0 eV, Physical Review B, 27 (1983) 985-1009.

[66] E.D. Palik, Handbook of optical constants of solids, Academic press, 1998.

[67] N. Yu, E. Cubukcu, L. Diehl, D. Bour, S. Corzine, J. Zhu, G. Höfler, K.B. Crozier, F. Capasso, Bowtie plasmonic quantum cascade laser antenna, Optics Express, 15 (2007) 13272-13281.

[68] A. Alu, N. Engheta, Input impedance, nanocircuit loading, and radiation tuning of optical nanoantennas, Physical review letters, 101 (2008) 043901.

[69] C. Multiphysics, Introduction to COMSOL Multiphysics®, COMSOL Multiphysics, Burlington, MA, accessed Feb, 9 (1998) 2018.

[70] G. Jellison Jr, Optical functions of silicon determined by two-channel polarization modulation ellipsometry, Optical Materials, 1 (1992) 41-47.

[71] D. Pierce, W.E. Spicer, Electronic structure of amorphous Si from photoemission and optical studies, Physical Review B, 5 (1972) 3017.

[72] A.D. Rakić, Algorithm for the determination of intrinsic optical constants of metal films: application to aluminum, Appl. Opt., 34 (1995) 4755-4767.

[73] D. Franta, I. Ohlídal, D. Nečas, F. Vižd'a, O. Caha, M. Hasoň, P. Pokorný, Optical characterization of HfO2 thin films, Thin Solid Films, 519 (2011) 6085-6091.

[74] G.H. Chan, J. Zhao, G.C. Schatz, R.P. Van Duyne, Localized surface plasmon resonance spectroscopy of triangular aluminum nanoparticles, The Journal of Physical Chemistry C, 112 (2008) 13958-13963.

[75] M. Kikawada, A. Ono, W. Inami, Y. Kawata, Enhanced multicolor fluorescence in bioimaging using deep-ultraviolet surface plasmon resonance, Applied Physics Letters, 104 (2014) 223703.

[76] P.B. Johnson, R.-W. Christy, Optical constants of the noble metals, Physical review B, 6 (1972) 4370.

[77] S. Kawata, Y. Inouye, P. Verma, Plasmonics for near-field nano-imaging and superlensing, Nature photonics, 3 (2009) 388.

[78] D.L. Jones, L.V. Kochian, Aluminum interaction with plasma membrane lipids and enzyme metal binding sites and its potential role in Al cytotoxicity, FEBS letters, 400 (1997) 51-57.

[79] L. Li, S. Fang Lim, A.A. Puretzky, R. Riehn, H. Hallen, Near-field enhanced ultraviolet resonance Raman spectroscopy using aluminum bow-tie nano-antenna, Applied physics letters, 101 (2012) 113116.

[80] M.W. Knight, N.S. King, L. Liu, H.O. Everitt, P. Nordlander, N.J. Halas, Aluminum for plasmonics, ACS nano, 8 (2013) 834-840.

[81] F. Erogbogbo, K.-T. Yong, I. Roy, R. Hu, W.-C. Law, W. Zhao, H. Ding, F. Wu, R. Kumar, M.T. Swihart, In vivo targeted cancer imaging, sentinel lymph node mapping and multi-channel imaging with biocompatible silicon nanocrystals, ACS nano, 5 (2010) 413-423.

[82] S. Zhang, Y.-S. Park, Y. Liu, T. Zentgraf, X. Zhang, Far-field measurement of ultra-small plasmonic mode volume, Optics express, 18 (2010) 6048-6055.

[83] E.M. Purcell, Spontaneous emission probabilities at radio frequencies, in: Confined electrons and photons, Springer, 1995, pp. 839-839.

[84] D. Arbel, N. Berkovitch, A. Nevet, A. Peer, S. Cohen, D. Ritter, M. Orenstein, Light emission rate enhancement from InP MQW by plasmon nano-antenna arrays, Optics Express, 19 (2011) 9807-9813.

[85] C. Belacel, B. Habert, F. Bigourdan, F. Marquier, J.-P. Hugonin, S. Michaelis de Vasconcellos, X. Lafosse, L. Coolen, C. Schwob, C. Javaux, Controlling

spontaneous emission with plasmonic optical patch antennas, Nano letters, 13 (2013) 1516-1521.

[86] Y. Yang, K. Ekinci, X. Huang, L. Schiavone, M. Roukes, C. Zorman, M. Mehregany, Monocrystalline silicon carbide nanoelectromechanical systems, Applied Physics Letters, 78 (2001) 162-164.

[87] I.-T. Chen, P.-H. Chang, Y.-C. Chang, T.-F. Guo, Lighting up ultraviolet fluorescence from chicken albumen through plasmon resonance energy transfer of gold nanoparticles, Scientific reports, 3 (2013) 1505.

[88] R. Kitamura, L. Pilon, M. Jonasz, Optical constants of silica glass from extreme ultraviolet to far infrared at near room temperature, Appl. Opt., 46 (2007) 8118-8133.

[89] S. Zollner, J. Chen, E. Duda, T. Wetteroth, S. Wilson, J.N. Hilfiker, Dielectric functions of bulk 4H and 6H SiC and spectroscopic ellipsometry studies of thin SiC films on Si, Journal of applied physics, 85 (1999) 8353-8361.

[90] D. Tarn, C.E. Ashley, M. Xue, E.C. Carnes, J.I. Zink, C.J. Brinker, Mesoporous silica nanoparticle nanocarriers: biofunctionality and biocompatibility, Accounts of chemical research, 46 (2013) 792-801.

[91] J. Botsoa, V. Lysenko, A. Geloen, O. Marty, J. Bluet, G. Guillot, Application of 3 C-Si C quantum dots for living cell imaging, Applied Physics Letters, 92 (2008) 173902.

[92] M.S. Eggleston, K. Messer, L. Zhang, E. Yablonovitch, M.C. Wu, Optical antenna enhanced spontaneous emission, Proceedings of the National Academy of Sciences, 112 (2015) 1704-1709.

[93] C.A. Balanis, Antenna theory: analysis and design, John wiley & sons, 2016.

[94] R. Fleury, J. Soric, A. Alù, Physical bounds on absorption and scattering for cloaked sensors, Physical Review B, 89 (2014) 045122.

[95] R.W. Gerchberg, A practical algorithm for the determination of phase from image and diffraction plane pictures, Optik, 35 (1972) 237-246.

[96] J. Zhang, N. Pégard, J. Zhong, H. Adesnik, L. Waller, 3D computer-generated holography by non-convex optimization, Optica, 4 (2017) 1306-1313.

[97] K.S. Kim, Y. Zhao, H. Jang, S.Y. Lee, J.M. Kim, K.S. Kim, J.-H. Ahn, P. Kim, J.-Y. Choi, B.H. Hong, Large-scale pattern growth of graphene films for stretchable transparent electrodes, nature, 457 (2009) 706.

[98] M. Campbell, D. Sharp, M. Harrison, R. Denning, A. Turberfield, Fabrication of photonic crystals for the visible spectrum by holographic lithography, Nature, 404 (2000) 53.

[99] A. Gerrard, J.M. Burch, Introduction to matrix methods in optics, Courier Corporation, 1994.

[100] S. Brown, J. Rose, Architecture of FPGAs and CPLDs: A tutorial, IEEE Design and Test of Computers, 13 (1996) 42-57.

[101] A. Silva, F. Monticone, G. Castaldi, V. Galdi, A. Alù, N. Engheta, Performing mathematical operations with metamaterials, Science, 343 (2014) 160-163.

[102] N.I. Zheludev, E. Plum, Reconfigurable nanomechanical photonic metamaterials, Nature nanotechnology, 11 (2016) 16.

[103] J.Y. Ou, E. Plum, J. Zhang, N.I. Zheludev, Giant nonlinearity of an optically reconfigurable plasmonic metamaterial, Advanced Materials, 28 (2016) 729-733.

[104] L. Cong, P. Pitchappa, C. Lee, R. Singh, Active phase transition via loss engineering in a terahertz MEMS metamaterial, Advanced Materials, 29 (2017) 1700733.

[105] N.I. Zheludev, Obtaining optical properties on demand, Science, 348 (2015) 973-974.

[106] Q. Wang, E.T. Rogers, B. Gholipour, C.-M. Wang, G. Yuan, J. Teng, N.I. Zheludev, Optically reconfigurable metasurfaces and photonic devices based on phase change materials, Nature Photonics, 10 (2016) 60.

[107] Z. Sun, J. Zhou, R. Ahuja, Unique melting behavior in phase-change materials for rewritable data storage, Physical review letters, 98 (2007) 055505.

[108] D. Fu, K. Liu, T. Tao, K. Lo, C. Cheng, B. Liu, R. Zhang, H.A. Bechtel, J. Wu, Comprehensive study of the metal-insulator transition in pulsed laser deposited epitaxial VO2 thin films, Journal of Applied Physics, 113 (2013) 043707.

[109] A. Cavalleri, T. Dekorsy, H.H. Chong, J.-C. Kieffer, R.W. Schoenlein, Evidence for a structurally-driven insulator-to-metal transition in VO 2: A view from the ultrafast timescale, Physical Review B, 70 (2004) 161102.

[110] M. Haverkort, Z. Hu, A. Tanaka, W. Reichelt, S. Streltsov, M. Korotin, V. Anisimov, H. Hsieh, H.-J. Lin, C. Chen, Orbital-assisted metal-insulator transition in VO 2, Physical Review Letters, 95 (2005) 196404.

[111] M.M. Qazilbash, M. Brehm, B.-G. Chae, P.-C. Ho, G.O. Andreev, B.-J. Kim, S.J. Yun, A. Balatsky, M. Maple, F. Keilmann, Mott transition in VO2 revealed by infrared spectroscopy and nano-imaging, Science, 318 (2007) 1750-1753.

[112] K. Appavoo, D.Y. Lei, Y. Sonnefraud, B. Wang, S.T. Pantelides, S.A. Maier, R.F. Haglund Jr, Role of defects in the phase transition of VO2 nanoparticles probed by plasmon resonance spectroscopy, Nano letters, 12 (2012) 780-786.

[113] H. Ma, J. Hou, X. Wang, J. Zhang, Z. Yuan, L. Xiao, Y. Wei, S. Fan, K. Jiang, K. Liu, Flexible, all-inorganic actuators based on vanadium dioxide and carbon nanotube bimorphs, Nano letters, 17 (2016) 421-428.

[114] M. Qazilbash, M. Brehm, G. Andreev, A. Frenzel, P.-C. Ho, B.-G. Chae, B.-J. Kim, S.J. Yun, H.-T. Kim, A. Balatsky, Infrared spectroscopy and nano-imaging of the insulator-to-metal transition in vanadium dioxide, Physical Review B, 79 (2009) 075107.

[115] S. Kumar, M.D. Pickett, J.P. Strachan, G. Gibson, Y. Nishi, R.S. Williams, Local Temperature Redistribution and Structural Transition During Joule‐Heating‐Driven Conductance Switching in VO2, Advanced Materials, 25 (2013) 6128-6132.

[116] B. Hu, Y. Ding, W. Chen, D. Kulkarni, Y. Shen, V.V. Tsukruk, Z.L. Wang, External‐strain induced insulating phase transition in VO2 nanobeam and its application as flexible strain sensor, Advanced Materials, 22 (2010) 5134-5139.

[117] L. Pellegrino, N. Manca, T. Kanki, H. Tanaka, M. Biasotti, E. Bellingeri, A.S. Siri, D. Marré, Multistate Memory Devices Based on Free‐standing VO2/TiO2 Microstructures Driven by Joule Self‐Heating, Advanced Materials, 24 (2012) 2929-2934.

[118] J. Hou, X. Wang, D. Fu, C. Ko, Y. Chen, Y. Sun, S. Lee, K.X. Wang, K. Dong, Y. Sun, Modulating photoluminescence of monolayer molybdenum disulfide by metal–insulator phase transition in active substrates, small, 12 (2016) 3976-3984.

[119] A. Cavalleri, C. Tóth, C.W. Siders, J. Squier, F. Ráksi, P. Forget, J. Kieffer, Femtosecond structural dynamics in VO 2 during an ultrafast solid-solid phase transition, Physical review letters, 87 (2001) 237401.

[120] K. Aydin, V.E. Ferry, R.M. Briggs, H.A. Atwater, Broadband polarization-independent resonant light absorption using ultrathin plasmonic super absorbers, Nature communications, 2 (2011) 517.

[121] X. Ni, A.V. Kildishev, V.M. Shalaev, Metasurface holograms for visible light, Nature communications, 4 (2013) 2807.

[122] Y. Sun, B. Edwards, A. Alù, N. Engheta, Experimental realization of optical lumped nanocircuits at infrared wavelengths, Nature materials, 11 (2012) 208.

[123] R.C. Hansen, Phased array antennas, John Wiley & Sons, 2009.

[124] Z. Yaqoob, D. Psaltis, M.S. Feld, C. Yang, Optical phase conjugation for turbidity suppression in biological samples, Nature photonics, 2 (2008) 110.

[125] D.G. Grier, A revolution in optical manipulation, nature, 424 (2003) 810.

[126] Y. Zhang, T.-R. Chang, B. Zhou, Y.-T. Cui, H. Yan, Z. Liu, F. Schmitt, J. Lee, R. Moore, Y. Chen, Direct observation of the transition from indirect to direct bandgap in atomically thin epitaxial MoSe 2, Nature nanotechnology, 9 (2014) 111.

[127] C. Yan, J. Liu, Y. Zang, J. Wang, Z. Wang, P. Wang, Z.-D. Zhang, L. Wang, X. Ma, S. Ji, Experimental observation of Dirac-like surface states and topological phase transition in Pb 1− x Sn x Te (111) films, Physical review letters, 112 (2014) 186801.

[128] J. Zeng, X. Wang, J. Sun, A. Pandey, A.N. Cartwright, N.M. Litchinitser, Manipulating complex light with metamaterials, Scientific reports, 3 (2013) 2826.

[129] J. Rensberg, S. Zhang, Y. Zhou, A.S. McLeod, C. Schwarz, M. Goldflam, M. Liu, J. Kerbusch, R. Nawrodt, S. Ramanathan, Active optical metasurfaces based on defect-engineered phase-transition materials, Nano letters, 16 (2016) 1050-1055.

[130] L. Zhang, S. Mei, K. Huang, C.W. Qiu, Advances in full control of electromagnetic waves with metasurfaces, Advanced Optical Materials, 4 (2016) 818-833.

[131] J.L. Schwartz, M.A. Peck, C.D. Hall, Historical review of air-bearing spacecraft simulators, Journal of Guidance, Control, and Dynamics, 26 (2003) 513-522.

[132] P. Zhou, J.H. Burge, Fabrication error analysis and experimental demonstration for computer-generated holograms, Appl. Opt., 46 (2007) 657-663.

[133] H.F. Ma, T.J. Cui, Three-dimensional broadband ground-plane cloak made of metamaterials, Nature communications, 1 (2010) 21.

[134] Z. Yang, C. Ko, S. Ramanathan, Oxide electronics utilizing ultrafast metal-insulator transitions, Annual Review of Materials Research, 41 (2011) 337-367.

[135] H.J. Caulfield, S. Dolev, Why future supercomputing requires optics, Nature Photonics, 4 (2010) 261.

[136] R. Kirchain, L. Kimerling, A roadmap for nanophotonics, Nature Photonics, 1 (2007) 303.